3D-STIFFNESS MICROENVIRONMENT LEADS TO NUCLEAR ENVELOPE RUPTURE, DNA DAMAGE, AND GENOME VARIATION

Kuangzheng Zhu

A DISSERTATION

in

Chemical and Biomolecular Engineering

Presented to the Faculties of the University of Pennsylvania

in

Partial Fulfillment of the Requirements for the

Degree of Doctor of Philosophy 2021

Supervisor of Dissertation

Dennis E. Discher, Robert D. Bent Professor of Bioengineering, Chemical and Biomolecular Engineering, Mechanical Engineering, and Applied Mechanics

Graduate Group Chairperson

John C. Crocker, Professor of Chemical and Biomolecular Engineering

Dissertation Committee

John C. Crocker, Professor of Chemical and Biomolecular Engineering; Ravi Radhakrishnan, Professor of Bioengineering, Chemical and Biomolecular Engineering; Paul Janmey, Professor of Physiology, Physics and Astronomy

Acknowledgements

Thank you to Professor Dennis E. Discher, you are the most enthusiastic scholar I have met and fulfilled all my imaginations of a scientist and engineer whose stereotypes can only be judged from biographies. Your devotion in research and ardency in new discoveries have not only revealed your peerless ingenuity, but also provided us with motivation, inspiration, and even pleasure in exploring in the interdisciplinary field of mechano-molecular biology and pursuing the pure, clear truth behind convoluted, opaque procedures. We have learned not only solid knowledge, experimental skills, and analytical methods, but also, more importantly, ability to think critically and defensively, which constitutes the greatest legacy I obtained from you as my teacher. Sangkyun introduced me to your research group when I first visited the campus of UPenn, and I first met you in a happy hour and talked to you about cancer cells with Manasvita. You also had me work

as a teaching assistant for you in CBE 555 and 557, giving me more chances for Thanks also for inviting us for dinners in all conferences before Covid, and thanks to always caring about our health status after the Great Pandemic started.

Thank you to Professor John C. Crocker, our graduate group chair, my teacher in Transport II, also my committee member, as well as the guide in introducing us to the big family of the CBE department. I still remember you gave us new students lectures in the CBE office about the deadlines of proposal and defense. Time has elapsed so fast that I am going to defend. I really enjoy the materials I learned from the course you taught, which provides me with extraordinary knowledge in optics, useful for imaging analysis that has been frequently involved in my research experience. Also, hope you are not offended by me sending you some of my friends with administrative issues that need your mediation, as you always want to help students resolve their problems.

Thank you to my mentors who have graduated but given me guidance not only as little teachers but also elder brothers and sisters. Yuntao Xia has taught me the most laboratory and analytical skills in my first two years of research experience, and has provided me with advice in future careers and

people skills. You also began the project of Chr-loss reporter and made the initial important step as a pioneer. Congratulations again on your new-born cute baby! Charlotte has shadowed me on confocal microscopy, EdU staining, and SNPa sequencing algorithm. You like to listen to me bragging about linguistics and some ancient stories. You have advised me a lot in paper organization and future occupational planning. Sangkyun, you are the first person in the Discher lab I met, even before I formally went to UPenn, and gave me strong insights that made me finally your academic brother in this group. Thank you for trusting me in conducting the last experiment after you left. Similar to Charlotte, you like to listen to me storytelling about ancient Chinese and Korean history, wars and peace, fight and negotiation. Jerome, thank you for teaching me the logistics of SNPa and initially taught me how to use the SNPa sequencing algorithm with Matlab. Thank you for arranging all the singing and bowling game events for us during weekends. Too bad we never had those again after Covid.

Thank you to my current colleagues. Brandon Hayes, I would like to give you a strong hug, for your effort in the big project of Chr-loss reporter as a co first author. You have done a fantastic and productive job in cell culturing, flow cytometry, gene editing, etc. You helped me execute many

experiments during the first phase after opening in the shift that I couldn't attend. You like Japanese food and I do too, but too bad we didn't get together because of the Covid. Thank you to Jason Andrechak and Larry Dooling, for injecting cells to mice to form xenografts. Thank you to Mai Wang for your excellent computational skills in single cell sequencing capability. Thank you to Michael Tobin for finishing up the phenotype of cells with genomic variation. Thank you to Alisya Anlas for conducting confocal images on proving existence of reporter-neg cells in spheroids.

Thank you to our dear lab manager Manu Tewari. You have organized great PSOC talks and provided us with delicious food, including pizza, sushi, and sandwiches. You have also helped me with iPS culture strategies, as well as generated progeria cells for one of my early projects. Most people have entered and left the Discher group within a couple years except for you, who have eyewitnessed the history and changes of the lab.

Thank you to the master's students Dazhen Liu and Junhong Du for helping me out with cell culture and experiments in the project of nuclear envelope rupture and Chr-loss reporter, respectively. Hope you learned enough in this lab with Yuntao, me, and Brandon, and are happy where you are now as Ph.D. candidates. Moreover, the company from you guys allowed

me to talk to someone when nobody else was in the lab late at night, so that I would feel less lonely and stressed out. Sometimes you guys accompanied me for a walk along the Schuylkill River to Philadelphia Museum of Art and listen to me giving lectures on Western and Eastern histories.

Thank you to my other committee members professor Ravi Radhakrishnan and professor Paul Janmey. As PSOC members, you have attended PSOC talks frequently and have provided many suggestions to the works carried out by me and many of our colleagues. Your opinions, as are coming from a professional knowledge base, are important to consider for improving the research.

Thank you to our collaborators on the project professor Roger Greenberg and Professor Michael Lampson. Thanks to Roger for letting me use your 96-well mini flow cytometry to perform my testing of the dose-effect of reversine on cells. Thanks to Michael for suggestions in the field of spindle assembly checkpoint, and thanks also to Scott Chen for the antibodies provided to me.

Thank you to my roommate who is also my classmate in CBE department, Renjing Huang. We learned from each other in our first year to conquer complicated CBE core courses, especially kinetics and transport I

and II, but you ended up working in the field of catalysis, closer to what the information presented in the core courses. However, despite the indirect relationship, what I learned from course sources grant me my thinking pattern as an engineer with quantitative perceptions on many aspects.

Thank you to my undergraduate research advisor and department head, Professor Andrew Zydney in PSU. You gave me strong confidence in applying straightforward to Ph.D. programs and granted my first publication. Your judgment of me as suitable for performing research was even more in-depth than myself, and you provided me with my first guidance in looking for doctoral programs.

Thank you to all the staff members in the CBE secretary's office who have helped me a lot from showing me around the campus to booking conference rooms. Erin Reavy-Fredericks, you organized my first visit in UPenn, reimbursed my flight ticket, guided me to meet professors, and invited me to the first year seminar. Tamika Easley and Alicia Pickul, you guys prepared really yummy food with different types every Friday for the fourth-year seminar, and you like to listen to me discussing recent news together with Sabra Muhammad and Courtney Johnson. I was lucky to enjoy the food in my fourth-year seminar one month before the lockdown due to

Covid. Courtney, I am glad to share my knowledge about Chinese characters to you when you were learning Japanese, hopefully that assisted you somewhat. I am pleased that Junhong, my friend, became one of the top students in biotechnology with assistance from you. Jamie Lipford, thank you for trusting me in translating the characters on the desserts from Beijing indicating their flavors, and you have always been enthusiastically giving me greetings when I walked on the 3rd floor of Towne. Kenneth Lambert Jr., it is such a pity to not be able to talk to you a lot before Covid. I have constantly received emails from you but not able to meet you face to face. Nonetheless, you gave me my most important information on graduation deadlines and will be giving me a zoom link for hosting the hybrid dissertation talk.

Thank you to the National Institutes of Health/National Cancer Institute (U54 CA193417), Human Frontiers Sciences Program grant RGP0024, National Heart, Lung, and Blood Institute award R21 HL128187, the US–Israel Binational Science Foundation, National Science Foundation grant agreement CMMI 15-48571, and the Simons Foundation (327939), also B.H.H., M.P.T., and J.C.A. supported by Graduate Research Fellowships from the National Science Foundation (DGE-1845298). Thank you to core

facilities at the University of Pennsylvania Perelman School of Medicine for instrument access and assistance: Flow Cytometry and Cell Sorting Core, Stem Cell and Xenograft Core, Molecular Pathology and Imaging Core, and the Cell & Developmental Biology Microscopy Core, The Center for Applied Genomics Core in The Children's Hospital of Philadelphia for all SNPa analyses and support. Thank you to Paul Hallberg, Shifu Tian, and Thomas Williams in Flow core from sorting for me to training me on how to sort. Thank you to Jasmine Zhao and Andrea Stout for training me initially on confocal microscopy. Thank you to Maria Lemma for constantly taking samples from me to run the raw data of SNPa, and I apologize for the inconvenience during limited opening up when your colleagues Brett, George, and Zach had to pick them up.

Thank you to my parents and American parents for emotionally supporting me during the past five years of my Ph.D. life. I talk to you every day over the phone just to report I am OK, which sounds boring but is warm given the complicated criminal situations in Philadelphia and the pandemic occurring two years ago. To some extent, my father's suffering from lymphoma 8 years ago motivated me to do cancer research, and I really wish this could have not happened. Now your prognosis is good and never had a

relapse, but the understanding of fundamental causes and factors for cancer is still important, with which we can reduce future cancer probabilities and give more assistance to other people who may suffer from cancer as well. Unfortunately, my American parents, Louise and Keith, lost your dear daughter—the sister I have never met 30 years ago due to neuroblastoma. This is another motivation for my studies, although cruel and sad. Many patients have survived after the death of my American sister, according to her oncologist. Scientific success is built upon failure which includes people sacrificing. We sincerely mourn for those who have passed away because of cancer, bless for survivors from cancer, and conscientiously appreciate all who donated cells from their diseased organs (like A549 cells). You paved the way for cancer research and provided researchers and doctors with more insights in improving understanding and treatments of future patients. As I am writing this dissertation, I feel the predestined responsibility in facilitating the field of cancer biology in assisting more people who have been suffering.

Abstract

3D-STIFFNESS MICROENVIRONMENT LEADS TO NUCLEAR ENVELOPE RUPTURE, DNA DAMAGE, AND GENOME VARIATION

Kuangzheng Zhu

Dennis E. Discher

Solid tumor cells grow in a stiff microenvironment with dense extracellular matrix (ECM) and condensed packing of adjacent cells. Tumor cells are capable of migrating through constricted pores formed by ECM or surrounded by other cells, and the nuclear envelope can break with repair factor mislocalization, further leading to DNA damage and genetic changes, or even accumulated to be genomic variations. Cell division, likewise, is confined by a stiff niche of adjacent cells and extracellular matrix, and such confinement has been reported to cause chromosome mis-segregation. The chromosome-loss live cell reporter system was developed to prove that cells undergoing specific types of chromosome missegregation can survive and

maintain heritability, resulting in permanent genomic variations. Mitotic cells under *in vitro* confinement and *in vivo* conditions exhibit more abnormal division and more fluorescence-null reporter-negative cells, for both cancer and normal types. Confinement and SAC inhibition both lead to chromosome mis-segregation but do not superimpose, and Topoisomerase IIa plays an essential role in cells to survive after confined mitosis. Myosin II was found to lead to increased nuclear envelope rupture and, therefore, more DNA damage, while it protects mitotic cell rounding within 3D confined environments, since the increase of reporter-negative cells was observed after Myosin II knockdown.

Terminologies: nuclear envelope (NE), nuclear localization sequence (NLS), lamin, myosin, chromosome (Chr), copy number variation (CNV), extracellular matrix (ECM), aneuploidy, nocodazole (Noc), reversine, microtubule (MT), spindle assembly checkpoint (SAC), topoisomerase

Contents

Appendices

List of Figures

Chapter 1

Background and introduction

1.1 Mutation, repair factor, and DNA damage

Repair of DNA has developed along with evolution of organisms, with increasing accuracy and more complicated machinery. RNA virus (represented by Covid) which cannot even reproduce without a host, carries out point mutation at a rate of 10^{-3} to 10^{-5} per base per generation, not only because RNA chain lacks another strand to confirm its parental chain, but also because its repairing machinery is underdeveloped (Peck and Lauring, 2018; Agol and Gmyl, 2018). For bacteria or unicellular eukaryotes (like fungus or protozoan) that are more developed than RNA-virus, the rate becomes 0.003 mutations per genome per cell generation (Drake et al., 1998), translating to 10^{-9} to 10^{-10} mutation per base per cell generation, 10 thousand to a million times more stable than that of RNA-virus (sample calculation A1). We human beings normally carry out DNA base pair mutation at a frequency of 10^{-8} per site per biological generation, translating to at least 10^{-20} per site per cell generation, at least 10 orders of magnitudes lower than that of E. coli (Drake et al., 1998, sample calculation A1). DNA repair can be conducted in single or double strands, and double-stranded DNA repair in mammals include homologous recombination (HR) as well as non-homologous ending joining (NHEJ) pathways, both of which are responsible for DNA repair in G1 and G2 phases to prepare for as precise mitosis procedure as possible. In general, NHEJ is a less accurate machinery than HR, with the latter requiring a DNA template while the former involving basic ligation of

phospho-diester bond at the breaking backbone (Kakarougkas and Jeggo, 2014a), but NHEJ does indeed play a major role in DNA repair before DNA synthesis in G0/G1 phase. Factors KU70 and KU80, for example, can form dimers and play an essential role in NHEJ in G0/G1 phase (Kakarougkas and Jeggo, 2014a; Boulton and Jackson, 1998). BRCA, 53BP1, msh family, and RPA, on the other hand, are involved in HR in various degrees, which function in late S to G2 phases where DNA replication has completed (Kakarougkas and Jeggo, 2014a; Boulton, 2006; Wang et al., 2001; Warmoes et al., 2012; Wang et al., 2019; Chen and Wold, 2014; Yoshida and Miki, 2004). BRCA1 and BRCA2 are also tumor suppressor genes, and are found to be mutated or non-functional in breast cancer (Friedenson, 2007; O'Donovan and Livingston, 2010; Duncan et al., 1998; Yoshida and Miki, 2004); 53BP1 binds to the famous, important tumor suppressor gene p53 (Iwabuchi et al., 1994; Iwabuchi et al., 1998; Alberts, 2015); msh family proteins are also tumor suppressors, and mutation in msh2 is related to hereditary nonpolyposis colorectal cancer (Ring et al., 2017; de Wind et al.,1995). Since these DNA repair factors are normally located inside the nuclear envelope, many of which display tumor suppressor function, their mislocalization, leading to insufficient amount or equivalent to down regulation, can be an interesting topic to study in terms of increased DNA damage as related to cancer progression (Irianto et al., 2017; Kakarougkas and Jeggo, 2014; Christmann and Kaina, 2000; von Morgen et al., 2018). In this sense, even though eukaryotes developed nuclear envelope to compartmentalize important genetic materials and relevant factors and enzymes, abnormal perturbation either intranuclear or

transnuclear indirectly bring genetic errors back to the nucleic acids, which, in turn, drastically inhibit the DNA replication error-correcting system.

1.2 Aneuploidy and genomic instability

Aneuploidy is the genomic status of a cell with an abnormal number of chromosomes, and the total number of chromosomes is not a multiple of a normal haploid of the organism. Human somatic cells are normally diploid, while many plant organs can go triploid or even tetraploid in nature, but still maintain euploidy (Vignesh Kumar et al., 2020; Zhang et al., 2019;Perrier et al., 2011). Aneuploidy, on the other hand, is the status of unequal copy numbers among all homologous chromosomes. Down's Syndrome, for instance, gives trisomy (3 copies of a chromosome) in chromosome 21, while 2 copies of the rest (Patterson, 2009). Many special sex status, like Klinefelter syndrome (nicknamed "super male" ,XXY), and Turner Syndrome (infertile woman, XO) are all results of aneuploidy in sex chromosomes (Klinefelter, 1986; Astwood, 2014; Gunther et al., 2004). Additionally, aneuploidy can exist with more or fewer copies of partial chromosomes. Jacobsen Syndrome, for example, results

from deletion of a band from the q-arm of chromosome 11 (Favier et al., 2015). All of the above examples of aneuploidy occur pre-development. In other words, the abnormality in chromosome numbers existed prior to fertilization in sperm or egg which had gone through meiosis with chromosome non-disjunction (a kind of mis-segregation) or inherited biological problems from spermatocytes or oocytes (Alberts, 2015). Therefore, as a result of a fertilized egg that divided millions of cycles, diseased patients have all of their somatic cells carrying those abnormal genomes. Unfortunately, many fetus with chromosome miscarriage are lethal, and cannot live to birth, within which Down's syndrome has already given one of the highest rates of live birth cases (Driscoll and Gross; Griffiths, 2005; Morris et al., 1999).

Cancer cells, however, survive with aneuploidy in many different formats (Duijf et al., 2013; Rajagopalan and Lengauer, 2004; Hassold and Hunt, 2001). Two thirds of human solid tumors are aneuploid (Duijf et al., 2013). Many of them result from chromosome mis-segregation in mitosis, leading to chromosome losses or gains (Nicholson et al., 2015; Santaguida et al., 2017). This process can persist for descendent cells, especially if the lost chromosome contains many tumor suppressor genes and the acquired chromosome contains oncogenes. Nonetheless, aneuploidy in other chromosomes can also trigger it if the pathway of tumor-related genes is changed by genes located on these chromosomes, or leading to mutations in tumor-related genes. Additionally, the continued process of chromosome mis-segregation in aneuploid cancer

cells would lead to genomically unidentical descendants with different phenotypes that can potentially be selected for after chemotherapy drug and give rise to bad prognosis (Schmitt et al., 2012; Mansoori et al., 2017; Nathanson et al., 2014; Benner et al., 1991; Greaves and Maley, 2012). The mixture of cancer cells with heterogeneity in genotype existent in a tumor is also termed as chromosomal mosaicism (Lichtenstein, 2018; Iourov et al., 2019). Therefore, the mutation of cancer has been well-known to contribute difficulties to cancer treatment. DNA damage, after all, represents one or some point mutations in nucleotide base pair and, therefore, amino acids, while Chromosome Copy Number Variation (CNV) leads to the change of genes in the entire chromosome or at least portion of it, covering thousands of genes and the proteins expressed by them (Yao and Dai, 2014; Northcott et al., 2017; Bittel and Butler, 2005; Shlien and Malkin, 2009; Zheng et al., 2020).

1.3 Endogenous mechanical perturbations

Biochemical and radiational perturbations have been ubiquitously admitted as a major exogenous source of cancer formation and progression (Holt, 1979; Tomasetti et al.,

2017a). Exogenous chemical processes, such as drinking alcohol, inhaling carcinogenic odor, and consuming heavily grilled meat product, have been frequently reported to lead to cancer, by increasing the chances of building up malignant genomic and genetic mutations , including but not limited to carcinogens binding to DNA or their repair factors, inhibiting function of mitotic proteins or tumor suppressors (Jiang et al., 2007; Ratna and Mandrekar, 2017; Pfeifer et al., 2002; Seitz and Stickel, 2007). Nonetheless, DNA damage and genome alterations can be triggered not only chemically but also mechanically. Cancer cells can migrate when ECM gives abnormal stiffness, which then leads to metastasis (Eble and Niland, 2019; Fattet et al., 2020; Najafi et al., 2019; Bonnans et al., 2014). Other than alcohol, cirrhosis also contributes significantly to liver cancer, providing stiff environment for liver cells (GBD 2013 Mortality and Causes of Death Collaborators, 2015; Chung et al., 2018; Dooley et al., 2018a), with extracellular matrix (Dooley et al., 2018b; Parola and Pinzani, 2019; Schwabe et al., 2020), and this could be traced back to earlier fat liver diseases where lipid droplet can squeeze and change the shape of organelles, including nuclei (Castera et al., 2019; Farrell and Larter, 2006). High stiffness is found to be frequently associated with increased genomic instability and enhanced mutation in cancer (Pfeifer et al., 2017a; López-Carrasco et al., 2020; Deville and Cordes, 2019). Tumor cells frequently pass through tortuous and constricted space formed by convoluted ECM without degrading it or releasing its tension, which further leads to breaking of nuclear envelope at high-curvature sites followed by repair factor mislocalization (Song et al., 2016; Iredale, 2003; Jackson et al., 2017; Lamalice et al., 2007; Xia et al., 2018; Irianto et al., 2017a, Fig.

1.1,1.2). Additionally, cell division under a high-stiffness tumor environment is a possible reason leading to more genomic variation (Fig. 1.1), since recent studies have disclosed that tumors with higher stiffness and more times of divisions are associated with more potential genomic variation (Deville and Cordes, 2019; Pfeifer et al., 2017b), and abnormal mitosis have been seen in many tumor biopsies (Jin et al., 2007; Sun et al., 2003), in contrast to stem cell mitosis in soft substrate such as bone marrow that doesn't give rise to error in cell division before differentiation (Swift et al., 2013; Pfeifer et al., 2017a;Tomasetti et al., 2017b).

Endogenous, direct molecular mechanisms of cancer formation and progression include but are not limited to overexpression of oncogenes and downregulation or even deletion of tumor suppressors (Weinberg, 2014; Liu et al., 2015; Mo et al., 2020; Payne and Kemp, 2005; Wang et al., 2020; Wang et al., 2016). However, interestingly, some cancer cells have normal tumor suppressor genes, like A549 cell line have normal p53 expression (Guo et al., 2014; Guntur et al., 2010). In this case, loss of tumor suppressor isn't the only way through which chromosomal gains and losses occur, while mechanically generated chromosomal CNV plays an important role. Realistically, tumor suppressor mutation and mislocalization of repair factors with tumor suppressor functions still contribute significantly to tumorigenesis, but their mutual cause-and-effect relationship with mechanical stress should be emphasized. In other words, overexpression of oncogene and deletion of tumor suppressor gene can result from completely

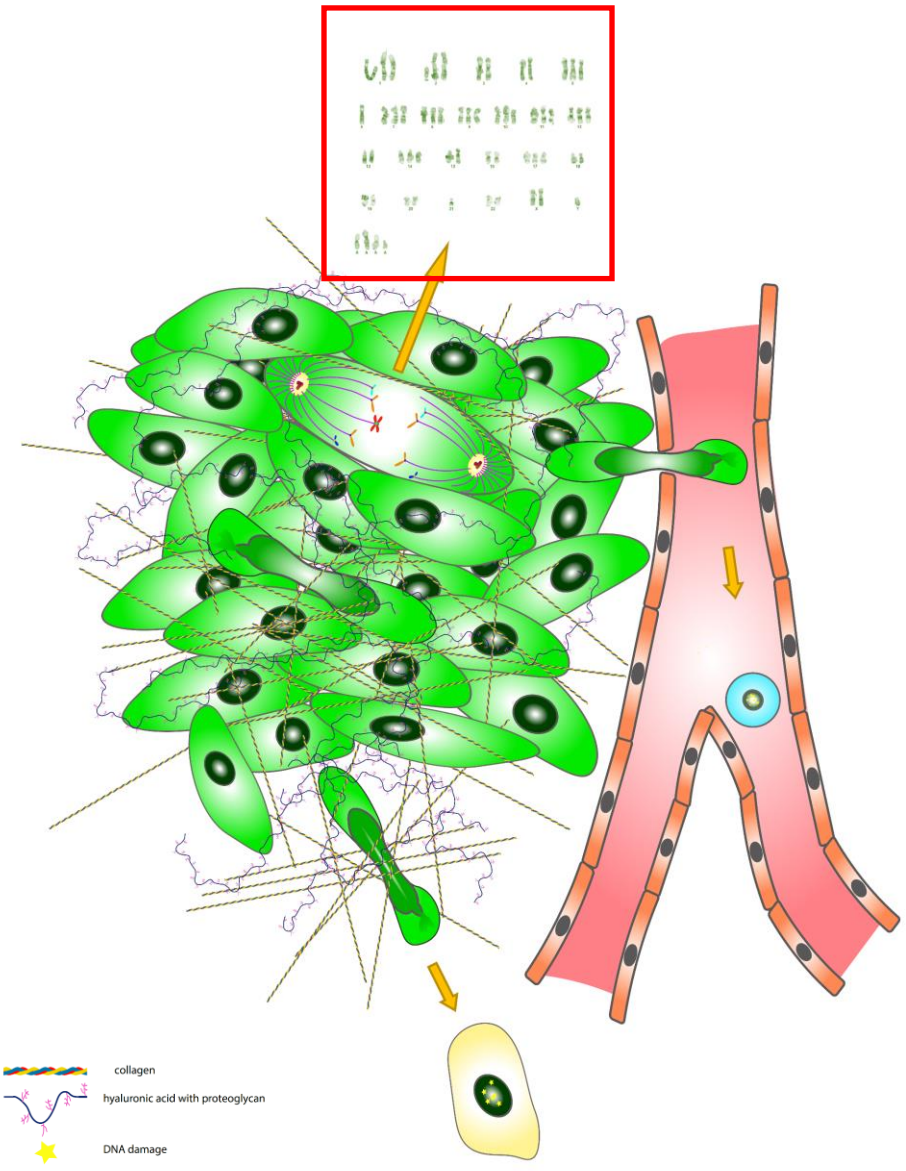

Figure 1.1: Schematic of the mechano-microenvironment of tumor cells. Tumor cells are densely packed in 3D stiff environment composed of ECM and adjacent cells. They migrate through constricted space formed by ECM (made of collagen, hyaluronic acid, etc) and result in DNA damage due to nuclear envelope rupture, and also undergo mitosis under confined space surrounded by adjacent cells and ECM, leading to chromosome copy number changes.

spontaneous random mutation, and can also be triggered by mechanical stress induced DNA damage or even chromosome copy number changes.

1.4 Myosin, microtubule, and Topoisomerase II

Thousands of proteins and factors work chemically and mechanically to stretch or compress cells and nuclei, provide them with protection and required functions to pursue the ultimate most important goal of biology---intactness of genetic material. In this study, we focus on non-muscle myosin, microtubule, and topoisomerase II.

As one of the first motor proteins to be discovered, myosin family proteins are well known for their ability to facilitate actin movement when energy is consumed through ATP hydrolysis on the head domains (Alberts, 2015; Hayashida et al., 1991). Different myosins constitute generally identical functions with subtle nuances which are enough to carry out different physical behaviors when involved in cell movement and motility (Raab et al., 2012; Pollard and Ostap, 1996). Actin functions in polymer, and also needs active contractility, for which myosin and actin work synergistically as actomyosin system which plays a significant role in cell stretching and migration (Raab et al., 2012), as well as

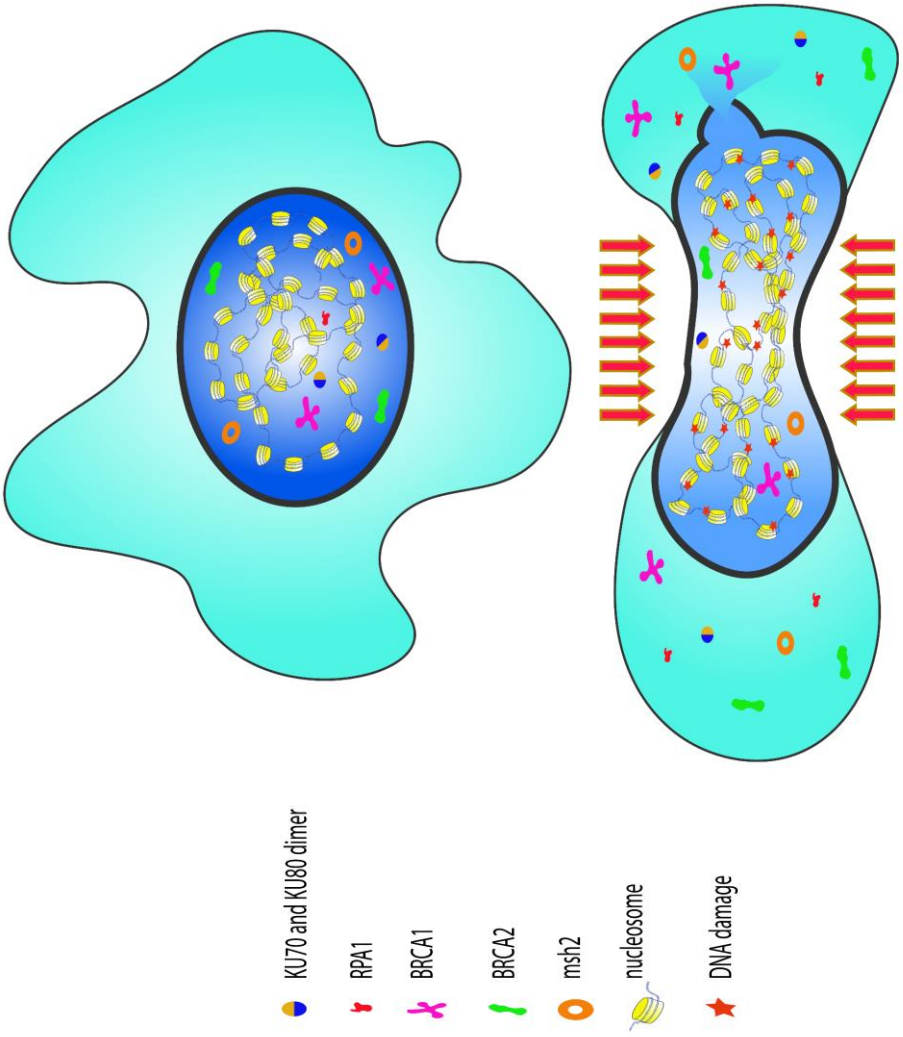

Figure 1.2: Schematic of compression leading to nuclear envelope rupture and DNA damage. Cells migrate through small pores or experience compressing force, high curvature spots formed on nuclear envelope undergo rupture with DNA repair factors (including KU70,KU80, BRCA1, BRCA2, RPA1, msh2, etc) flowing into the cytoplasm, which then leads to DNA damage.

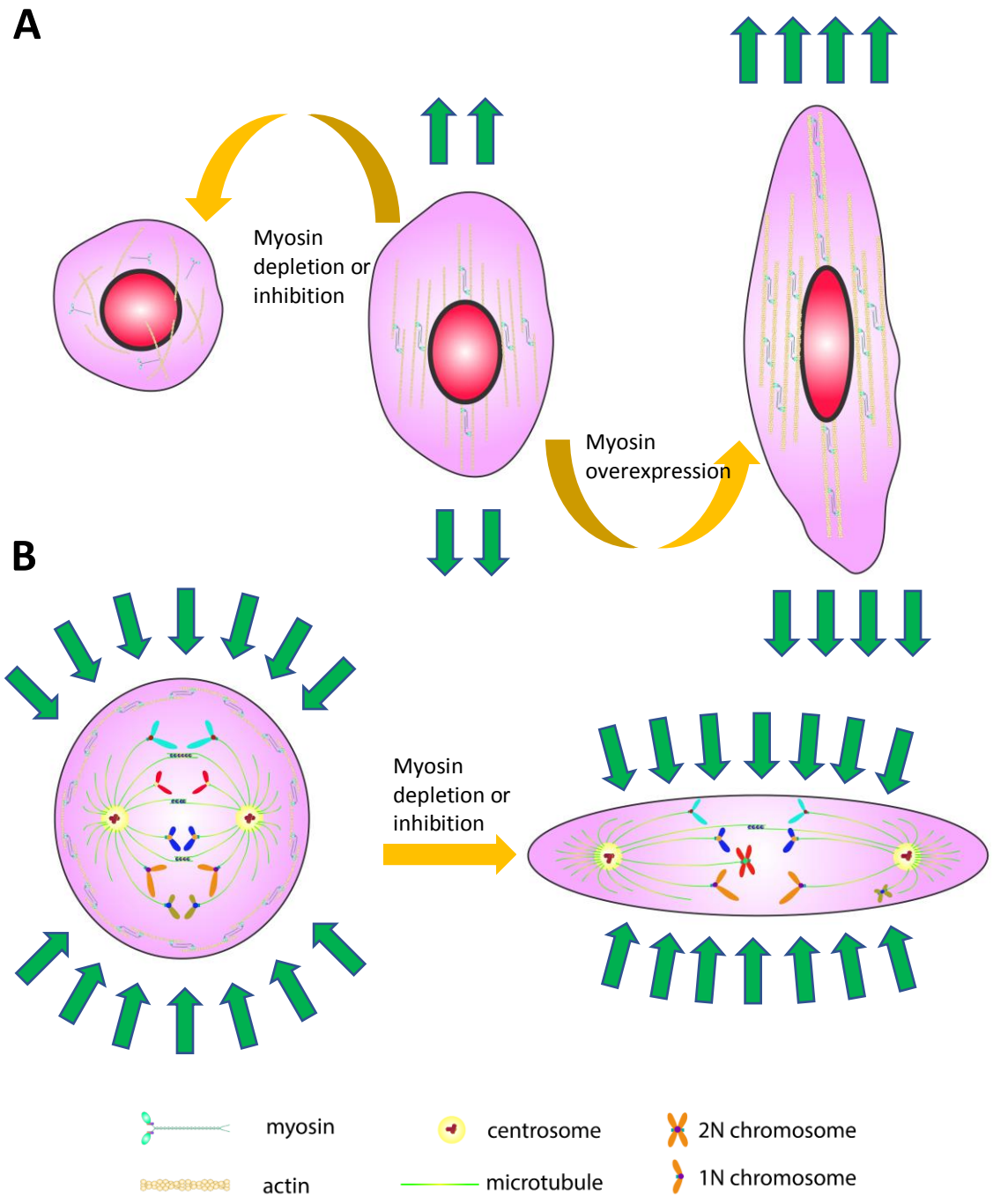
A
Myosin
depletion or
inhibition
Myosin
overexpression
B
Myosin
depletion or
inhibition
myosin
actin
centrosome
microtubule
2N chromosome
1N chromosome

Figure 1.3: Schematic of Myosin's effect on mechanical aspects of cell and nuclear shape. **(A)** myosin facilitates contraction and stretching of actin. Inhibition or depletion or inhibition of myosin leads to reduced or no actin contractility, giving nucleus and cell rounder shape; overexpression of it leads to enhanced stretching, providing cell and nucleus with elongated shape, with possible NE rupture on the site with high curvature. **(B)** actomyosin protects mitotic cell rounding shape against compressing forces from adjacent environment, without which the rounding can collapse and chromosome mis-segregation occur as a result.

protection of cell rounding cortex (Stewart et al., 2011). Inhibition of myosin gives similar, if not excessive, effects as drug-induced (latrunculin) actin depolymerization in many cases (Lancaster et al., 2013; Hu et al., 2019; Doller et al., 2015). Overexpression of myosin provides cells with more contractility, and is capable of stretching the nuclear envelope to break with increased elongation and distortion, vise versa (Fig. 1.3A). On the other hand, however, actomyosin generates force to protect mitotic cell rounding against compressing forces from external conditions, which helps maintain genome intactness by reducing errors in cell division (Fig. 1.3B). In this case, there seems to be a paradox that more myosin leads to increase in DNA damage in interphase cells but reduces chances of genomic instability after mitosis. Indeed, myosin plays a role in tumorigenesis (Ouderkirk and Krendel, 2014; Li and Yang, 2016), but is also categorized as tumor suppressor in some cases (Coaxum et al., 2017; Mazzolini et al., 2012), exhibiting a dilemma, yet unclear judgement of the protein, based upon many more pathways involved than the focus in our study (Wang et al., 2019). Nonetheless, the degree to which the genome is changed as a net consequence from the combination of NE rupture, abnormal mitosis under confinement, and other pathways, is the key to cancer generation and progression. The

degree may vary from case to case, giving myosin different directions in response to tumorigenesis.

Similar to myosin and actin, microtubule plays important roles in interphase as to cell movement and is one of the most essential mitotic proteins. Microtubule moves with a treadmilling process, with alpha, beta tubulins incorporated and eliminated alternatively (Alberts, 2015) from plus and minus ends, respectively. In mitosis, dynamics of microtubules allows chromosomes to be aligned properly at metaphase, as well as separation of sister chromatids. Both permanent disassembly (nocodazole, colchicine) and stability (paclitaxel) of microtubules prevent mitosis from proceeding, so both colchicine and paclitaxel can work as chemotherapy drugs in terms of prohibiting tumor cells from proliferating. Moreover, the length of the microtubule is critical for proper equatorial alignment of chromosomes (Lancaster et al., 2013; Dumont and Mitchison, 2009; Kapoor, 2017). Within a mitotic cell, Microtubule is emitted from the microtubule organization center (MTOC) with centrioles, and its length is controlled by the speed at which tubulins are assembled or disassembled. Confined space increases the cross-sectional area of mitotic cells, for which the original length of microtubule cannot fill the gap between MTOC and kinetochore (Dumont and Mitchison, 2009). Therefore, without proper microtubule attachment, chromosome alignment and sister chromatid segregation fail to proceed, leading to genomic variation.

The family of topoisomerase proteins contribute to DNA unwinding or untangling during cell cycle including but not limited to mitosis through single or double strand mechanisms where the backbone is temporarily broken and reannealed. Topoisomerase I, for instance, works with the single-strand annealing mechanism in interphase where DNA is being replicated (Alberts, 2015., (Girstun et al., 2017; Znojek et al., 2014). Topoisomerase II, on the other hand, unwinds DNA by breaking both strands, and is especially useful in mitosis to prevent sister chromatids from entangling and maintaining chromosome structures (Lee and Berger, 2019; Nielsen et al., 2020; Gemble et al., 2020). Our study finds that survived cells with specific genomic variation after passing through mitosis under confinement reveals an increase in Topoisomerase II expression than the same type of cells produced spontaneously, indicating that the protein is important in keeping the relative intactness of chromosome and disentangle them to pass through mitosis. It is not difficult to imagine that the extraordinary burden applied by confined space adds to more chances for chromosomes to entangle, and cells happening to express more Topoisomerase II can survive with less chromosomal damage, despite the result as genomically altered individuals.

1.5 Conclusion and outline

It has been stated prevalently that genetic and genomic errors accumulate for cancer formation and progression, and, in the past years, mechanobiological perturbations other than traditionally perceived biochemical and radial toxification have been gradually accepted as important causes of carcinogenesis. Nuclear envelope rupture, stated above as a process through which DNA becomes insufficiently repaired, is highly associated with abnormal quantity or behavior of cytoskeleton and associated proteins that introduce excessive mechanical stress, amplify pre-existing stress, and function simultaneously to yield superimposed effect. Even though DNA mutation yielded by mis-repair represents small-scale point mutation, its accumulation along with side effects of mis-repair can still have an effect on chromosome copy number variation (Irianto et al., 2017). Another important cause, or perhaps the main cause of CNV involves mitosis within a stiff 3D substrate (Pfeifer et al., 2017a). The increasing interest in cancer genomic instability or mosaicism have made popular use of microarray, single cell genome or transcriptome sequencing, and mass-spectroscopy, while the above methodologies require that cells be killed after which genetic material and peptides can be extracted. All cells to be studied have their biological processes terminate at the time of analysis, similar to the effect of Western blot, Immunofluorescence, and FISH (Mahmood and Yang, 2012; Mandrell et al., 1988; Langer-Safer et al., 1982). Therefore, our research provides a new method----Live Cell Chromosome Loss Reporter---to study genomic variation. In this case, genomically

altered cells with known chromosomes can keep growing after imaging or flow cytometry, and can also be accurately sorted and traced for heritability.

Since the background of mechanobiological causes of genomic instability was emphasized and introduced, the thesis now proceeds with the following logic: chapter 2 tends to describe cytoskeleton and ECM-introduced mechanical stress, along with and the brief mechanisms under which nuclear envelope rupture happens, followed by the effect on repair factor mislocalization and DNA mis-repair. More severe consequences—chromosome copy number variation, as a result of consecutive, repeated nuclear envelope rupture and DNA mis-repair, will also be discussed. In chapter 3, the design, fundamental ideas, and basic uses of the live cell chromosome reporter system will be introduced, to provide the basis of the new approach used in the more in-depth research related to the biophysical conditions leading to mitotic error, and, as a result, genomic variation. The reporter system is to be validated in that, 1. the loss of chromosomes can be accurately reflected by fluorescence color loss in cell; 2. Events with more mitotic error lead to more cells with color loss. In chapter 4, the topic of mitosis under confined space—an *in vitro* construct that mimics mitosis under stiff substrates *in vivo*--will be concentrated. The fact that mitosis under confined space leads to more mitotic error, and, therefore, an increase in genomic variation. Some molecular mechanisms of confinement-induced mitotic mistakes will be studied and discussed, including what proteins are up or down regulated after confinement, how mitosis under confinement is protected, and how confinement is

related to spindle assembly checkpoint inhibition in introducing aneuploidy. The viability and heritability, as a marker of presumably survived, mutated cancer cells, after perturbations including confinement, will also be displayed. In chapter 5, reporter cells *in vivo* as xenografts will be studied, to find out how and to what stage genomic variation is triggered by real somatic conditions where tumor forms, and how heritable they are. Moreover, some phenotypic changes as a result of chromosomal changes are revealed and analyzed.

Chapter 2

Mechanical Stress leads to nuclear envelope rupture and DNA damage

Data in Fig. 2.1 to 2.6 in this chapter have been published in Nuclear rupture at sites of high curvature compromises retention of DNA repair factors. *The Journal of Cell Biology*, 2018, *217*(11), 3796–3808, by Xia, Y., Ivanovska, I.L., Zhu, K., Smith, L., Irianto, J., Pfeifer, C.R., Alvey, C.M., Ji, J., Liu, D., Cho, S., Bennett, R.R., Liu, A.J., Greenberg, R.A., Discher, D.E.; data in Fig. 2.7 to 2.8 A-B have been published in Rescue of DNA damage after constricted migration reveals a mechano-regulated threshold for cell cycle. *The Journal of Cell Biology*, 2019,*218*(8), 2545–2563, by Xia, Y., Pfeifer C.R., Zhu K., Irianto J., Liu D., Pannell K., Chen E.J., Dooling L.J., Tobin M.P., Wang M., Ivanovska I.L., Smith L.R., Greenberg R.A., Discher D.E.. Dr.Yuntao Xia conducted analysis in Fig. 2.1, executed Fig. 2.3; Dr. Irena Ivanovska conducted AFM in Fig. 2.1; Fig. 2.2 was drawn by Dr. Dennis Discher; Dr. Jerome Irianto conducted Fig. 2.8 A & B. Kuangzheng Zhu plated and transfected cells for Fig. 2.1, and conducted experiments for all the rest of the figures.

2.1 Introduction

DNA damage and repair are ongoing in cell nucleus, and delayed repair along with insufficient repair are capable of leading to cumulative DNA damage, which is a source of cancer cell formation, mutation, and cell aging. One important source of DNA mis-repair is mislocalization of nuclear repair factors. In breast cancer cells, for instance, multiple repair factors mislocate, such as BRCA1 (Alshareeda et al., 2016). A conceivable mechanism for repair factor mislocalization is rupture of the nuclear envelope, as a result of increased mechanical stress, and the effect is further contributed by less sturdy nuclear envelope and/or increased curvature. Many cancer cells grow in stiff environment with overexpressed amount of ECM that leads to increased stretching, and some cancer cells (Alshareeda et al., 2016) or even abnormal somatic cells (e.g. progeria cells, de la Rosa et al., 2013) express insufficient than normal level of lamin A, leading to nuclei with reduced sturdiness (Capo-chichi et al., 2011) . High curvature, on the other hand, can occur when the nucleus undergoes squishing forces in an ECM network with limited pore size, and can result from mechanical stretching itself.

2.2 High curvature and increased contractility lead to NE rupture, repair factor mislocalization, and DNA damage

Lamina forms a protective structure inside the nucleus to provide it with physical strength, with lamin A/C and lamin B displaying different morphology and structural arrangement within the nuclear envelope. Nuclei in live U2OS osteosarcoma cells were probed with atomic force microscopy (AFM) tips of either medium or high curvature (4.5-µm sphere or pyramidal tip <0.1-µm diameter; Fig. 2.1, A and B). The force was held constant in a poly nano-Newton (nN) range similar to the contractile forces generated by cells (Saez et al., 2005). Nuclear factors that are known to be mobile within the nucleus were observed simultaneously with probing: these included YFP-NLS and GFP fusions of DNA repair factors 53BP1 and KU80 (Fig. 2.2). Sudden mislocalization to cytoplasm was frequently evident when probing with medium curvature tips after lamin A knockdown (Fig. 2.4 A), whereas WT nuclei required high-curvature tips (Fig. 2.1, A and B, bar graph). YFP or GFP signal filled the cytoplasm for minutes even after release of the AFM tip (Fig. 2.1 B, inset).

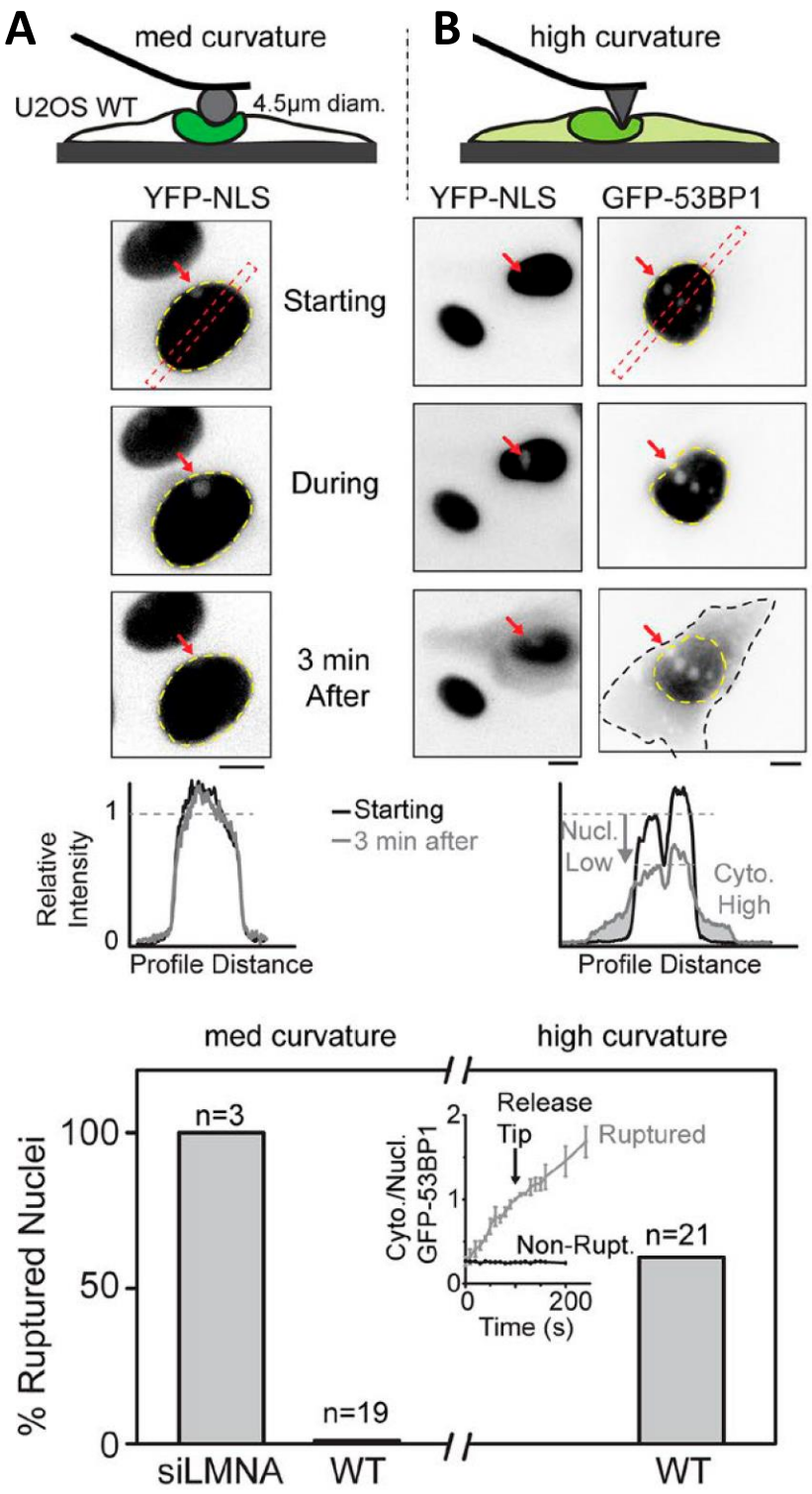

Figure 2.1:High-curvature probes rapidly rupture Nuclei, and LMNA protects nuclei from rupturing.
(A) Probing nuclei in living WT U2OS cells at constant force (~10–20 nN) with medium-curvature beads (diameter = 4.5 µm) shows no YFP-NLS mislocalization (inverse grayscale), whereas lamin A knockdown (siLMNA) causes frequent mislocalization (bar graph).

(B) High-curvature tips (diameter < 0.1 µm) rupture WT nuclei, based on mislocalization of YFP-NLS or GFP-53BP1 into cytoplasm within minutes (10/15 ruptured for GFP-53BP1 and 4/6 ruptured for YFP-NLS). Intensity profiles show decreased nuclear signal and higher cytoplasmic signal. Inset: Cytoplasmic GFP accumulates even after probe tip is removed. All scale bars = 10 µm

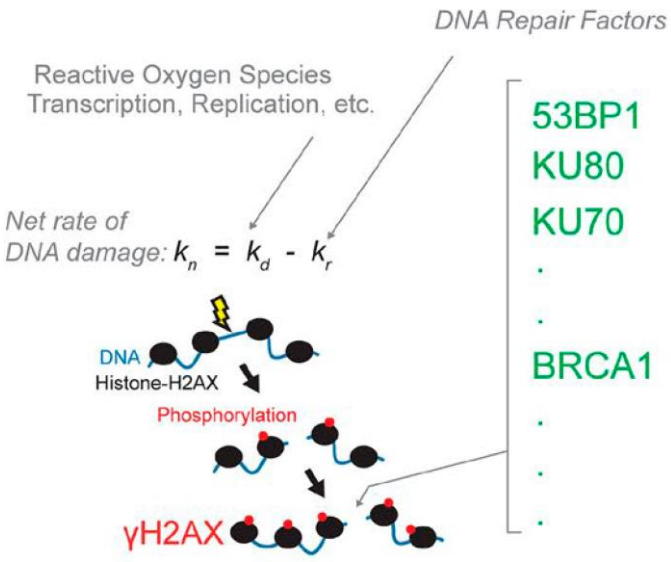

Figure 2.2: **Schematic diagram of DNA misrepair leading to DNA damage.** Various DNA repair proteins may be affected when the nuclear envelope ruptures. DNA damage triggers Histone component monomer H2AX to be phosphorylated, named γH2AX.

This indicates that both high curvature and depletion of lamin A lead to nuclear envelope rupture,and lamin A protects against high-curvature induced rupture. Repair factor relocalizes more slowly than NLS with lower weight (Fig. B1). Partial knockdown of lamin A with shLMNA was stably achieved in A549 lung carcinoma cells, whereas shLMNA-treated U2OS cells showed a growth defect (Fig. 2.4 B). These cells grew

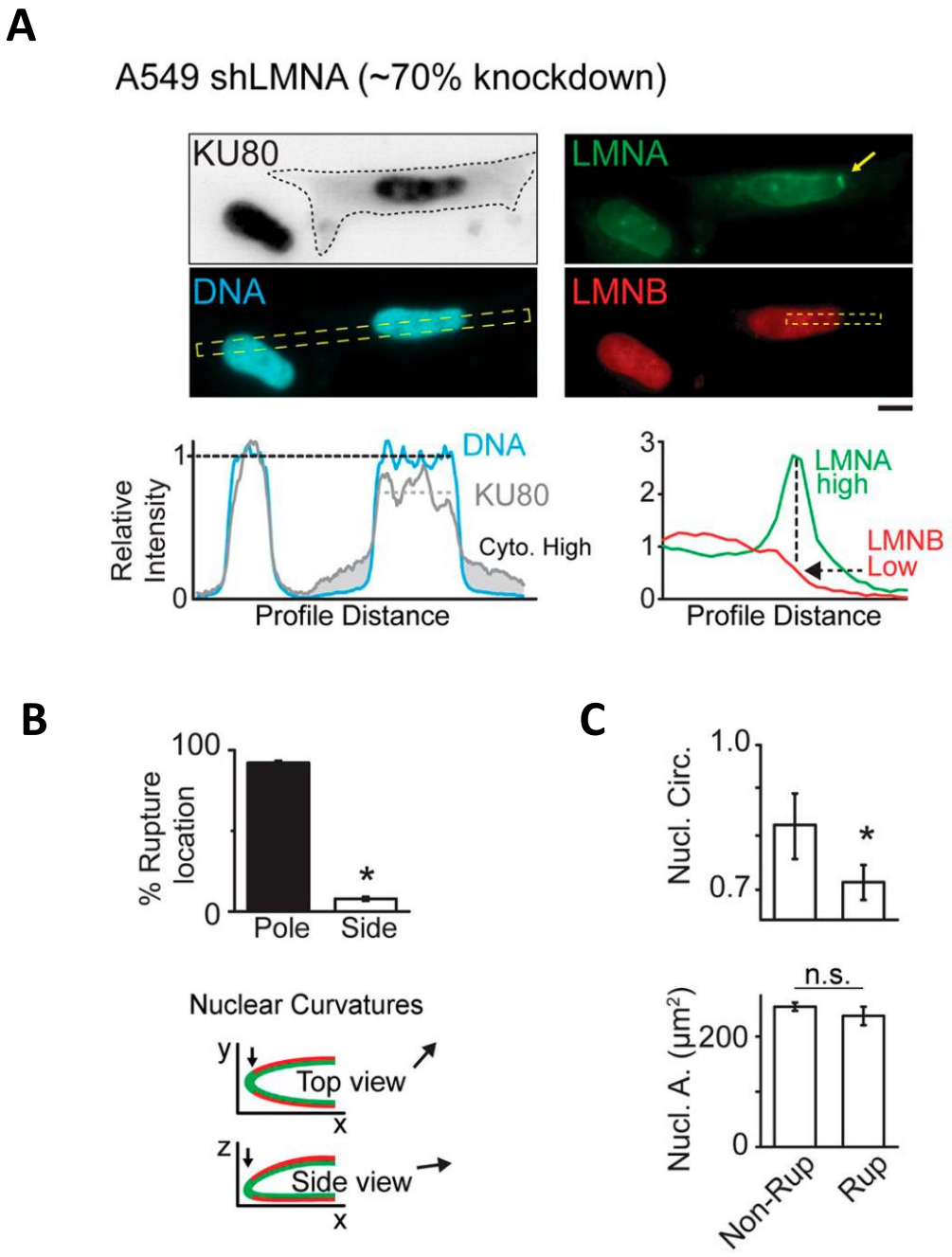

Figure 2.3: When lamin A is low in spreading cells, NE ruptures at high curvature site, enriched in lamin-A but depleted in lamin B. (A) Ruptured A549 shLMNA nuclei show high cytoplasmic KU80 by immunofluorescence; the lamina is focally enriched in lamin A (arrow) and depleted in lamin B. scale bar = 10 µm. **(B)** 92% of rupture events occur at poles of nuclei where curvature is high. Cartoon shows 2D curvature in cells. (Continued next page)

Figure 2.3: (Previous page) **(C)** Ruptured nuclei have lower circularity, indicating high curvature. Overall nuclear area remains the same. n > 150 cells in three experiments. * $p <$ 0.05, n.s., not significant.

normally (Fig. 2.4 C), but ∼10–20% of nuclei exhibited KU80 mislocalization in cells on rigid coverslips (Fig. 2.4 D). A relationship with nuclear curvature was evident: the lamina was disrupted at nuclear poles with enrichment of the residual lamin A and depletion of lamin-B (Fig. 2.3 A and B). Ruptured A549 nuclei were also more elongated, with lower nuclear circularity compared with nonruptured nuclei, while nuclear area was constant (Fig. 2.3 C). Immunostaining for the DNA damage marker γH2AX (Darzynkiewicz et al., 2011) together with KU80 indeed shows KU80 mislocalization tends to correlate with excess γH2AX foci in the shLMNA cells (Fig.B2, A & B). DNA damage foci were randomly distributed throughout the nucleoplasm rather than concentrated near sites of high-curvature lamina disruption (Fig. B2). Stable expression of GFP-LMNA rescued knockdown cells, and an electrophoretic comet assay for DNA damage confirmed the imaging (Fig. B2). Such a distribution is consistent with impeded repair of dispersed DNA damage.

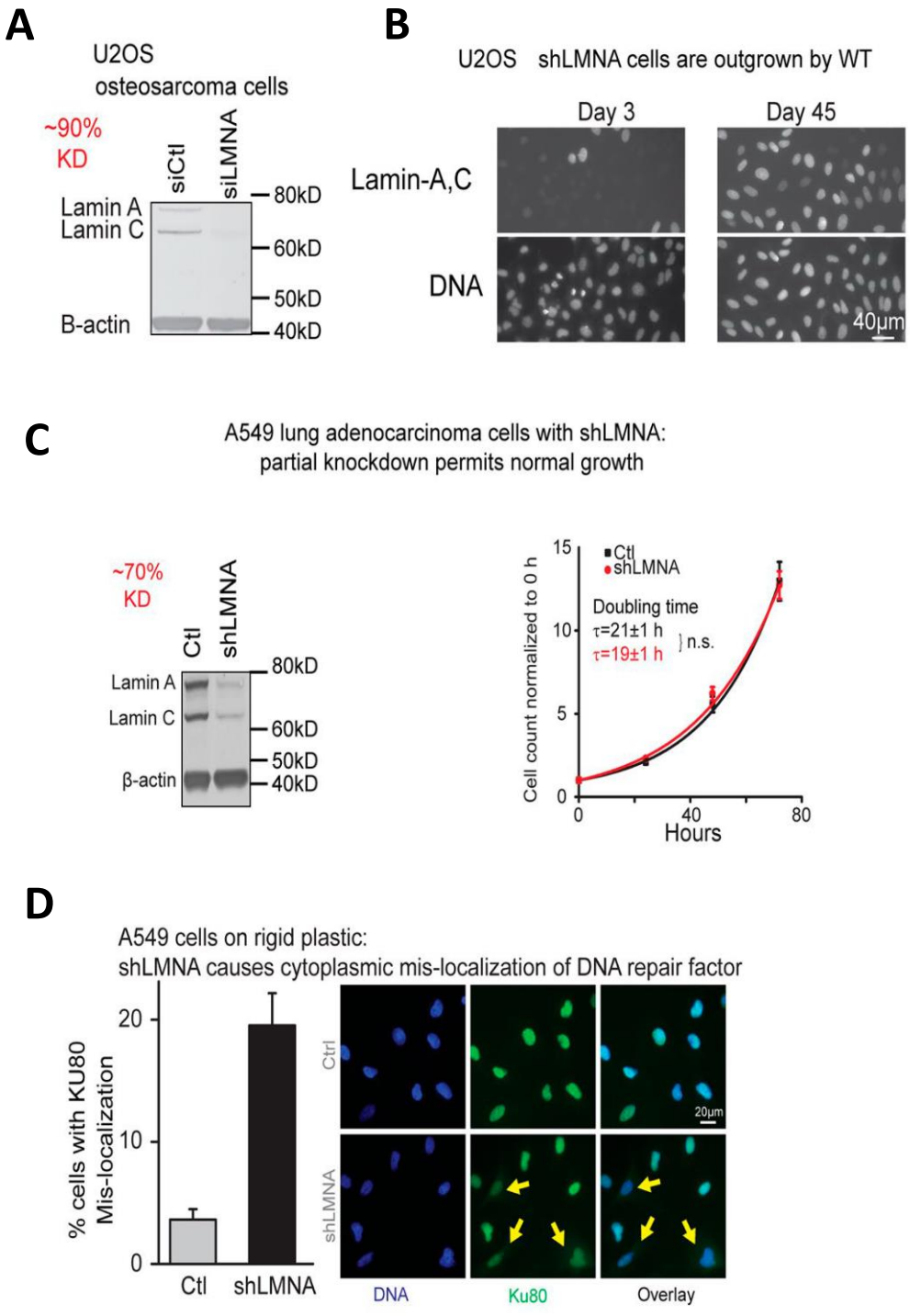
A
U2OS
osteosarcoma cells
~90%
KD
siCtl
siLMNA
Lamin A
Lamin C
B-actin
80kD
60kD
50kD
40kD
B
U2OS shLMNA cells are outgrown by WT
Day 3
Day 45
Lamin-A,C
DNA
40μm
C
A549 lung adenocarcinoma cells with shLMNA:
partial knockdown permits normal growth
~70%
KD
Ctl
shLMNA
Lamin A
Lamin C
β-actin
80kD
60kD
50kD
40kD
Ctl
shLMNA
Doubling time
τ=21±1 h
τ=19±1 h
n.s.
Cell count normalized to 0 h
Hours
D
A549 cells on rigid plastic:
shLMNA causes cytoplasmic mis-localization of DNA repair factor
% cells with KU80 Mis-localization
Ctl
shLMNA
DNA
Ku80
Overlay
20μm

Figure 2.4: Lamin A knockdown can affect cell growth and increase chances of repair factor mislocalization. (A) Approximately 90% of lamin A protein is depleted after siRNA treatment against LMNA. n = 3 experiments. **(B)** U2OS cells were transduced with shLMNA via lentiviral delivery. Some heterogeneity in lamin A levels was observed after shLMNA transduction, but the higher lamin A population dominates after long-term culture. **(C)** No difference in proliferation rate was observed between A549 Ctl and shLMNA cells. n = 5 experiments. **(D)** Approximately 20% of A549 shLMNA cells show mislocalization of KU80 when cultured on plastic. Arrows point to cells with DNA repair factor that is low in nucleus and high in cytoplasm. n > 5 fields of view per group in five experiments. Ctl, control.

DNA damage resulting from mislocalization of repair factors can be rescued by overexpression of endo-nuclear DNA repair factors. Expression plasmids for these three repair factors were thus pooled for cooverexpression (denoted GFP-3, KU70, KU80, BRCA1) in U2OS lamin A–knockdown cells (Fig. 2.5 C). GFP-53BP1 was used as a negative control (Ctl) because neither its overexpression nor si53BP1 affect DNA damage (Fig. B3). Rupture was assessed by cytoplasmic mislocalization of endogenous DNA repair factors or GFP fusions, and the latter transfections did not alter the ∼10% of ruptured cells in fixed cultures (Fig. 2.5 A). Even with rupture, nuclear GFP signal was intense relative to antibody staining for repair factors. For ruptured nuclei with cytoplasmic KU80 or GFP-53BP1, DNA damage was in equal excess, but GFP-3 rescued excess damage (Fig. 2.5 B). For nonruptured nuclei, GFP-3 had no effect on basal DNA damage (Fig. 2.5 B), and so the three DNA repair factors are not limiting except when the nucleus ruptures.

Myosin is a motor protein driving the function of actin, and the stretching of actin provides nucleus with shape deformation and elongation. Overexpression of nonmuscle

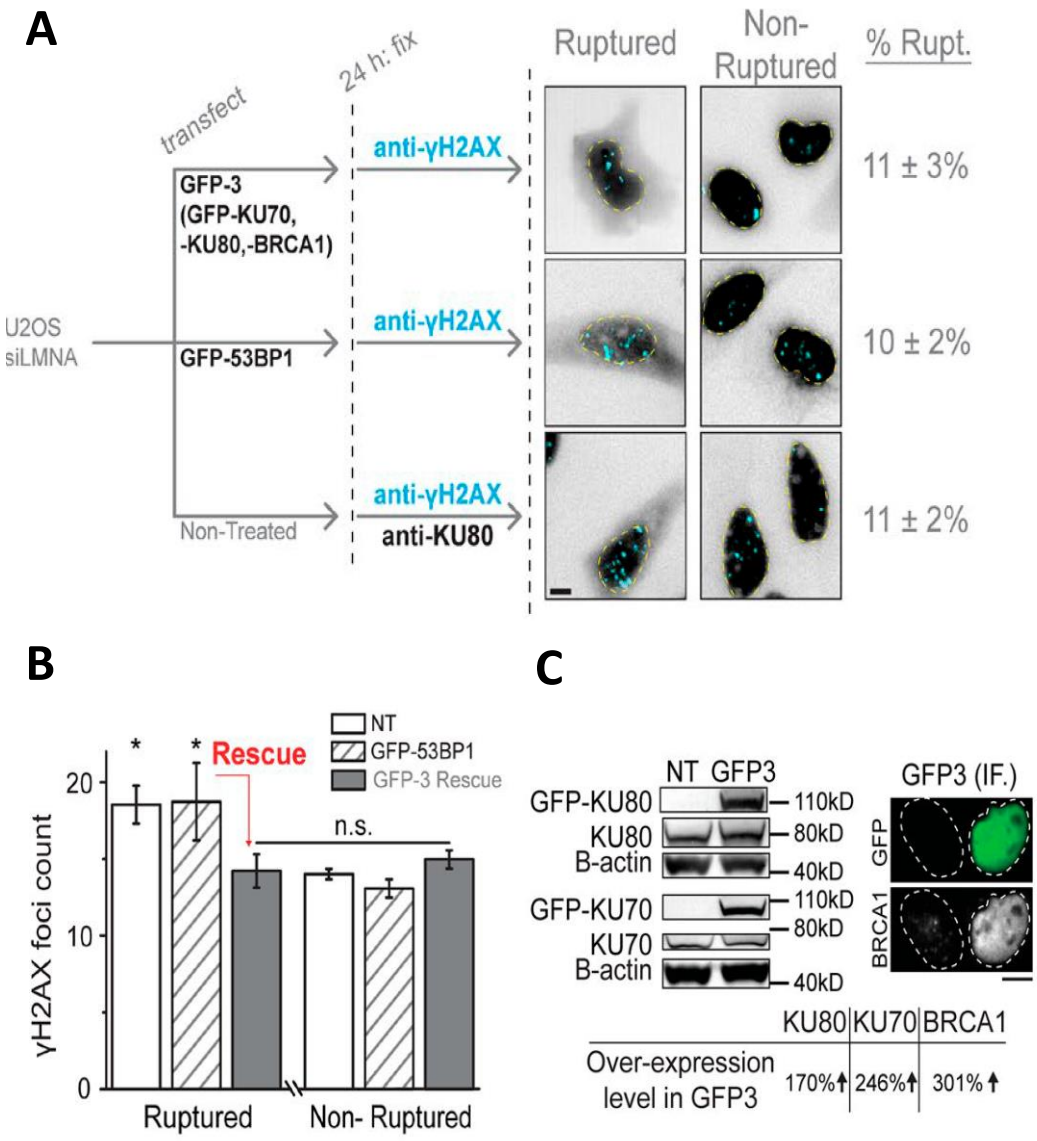

Figure 2.5: Co-overexpression of repair factors rescues DNA misrepair resulting from NE rupture. (A) siLMNA-U2OS cells were fixed after 24 h DNA repair factor transfection and immunostained for γH2AX. The nontransfected (NT) sample was also stained for KU80. Cytoplasmic mislocalization of the GFP or KU80 identifies ruptured nuclei. **(B)** Bar graph: Cotransfection of DNA repair factors KU70, KU80, and BRCA1 (GFP-3) rescues excess DNA damage in ruptured nuclei, whereas ruptured nuclei with GFP-53BP1 (and NT) maintain excess DNA damage. Nonruptured cells always show a basal level of DNA damage. n = 30–100 cells per condition in three experiments. **p* < 0.05; n.s., not significant. **(C)** Overexpression levels in GFP-3 U2OS cells. n = 3 experiments. IF, immunofluorescence; NT, nontransfected. All scale bars = 10 µm.

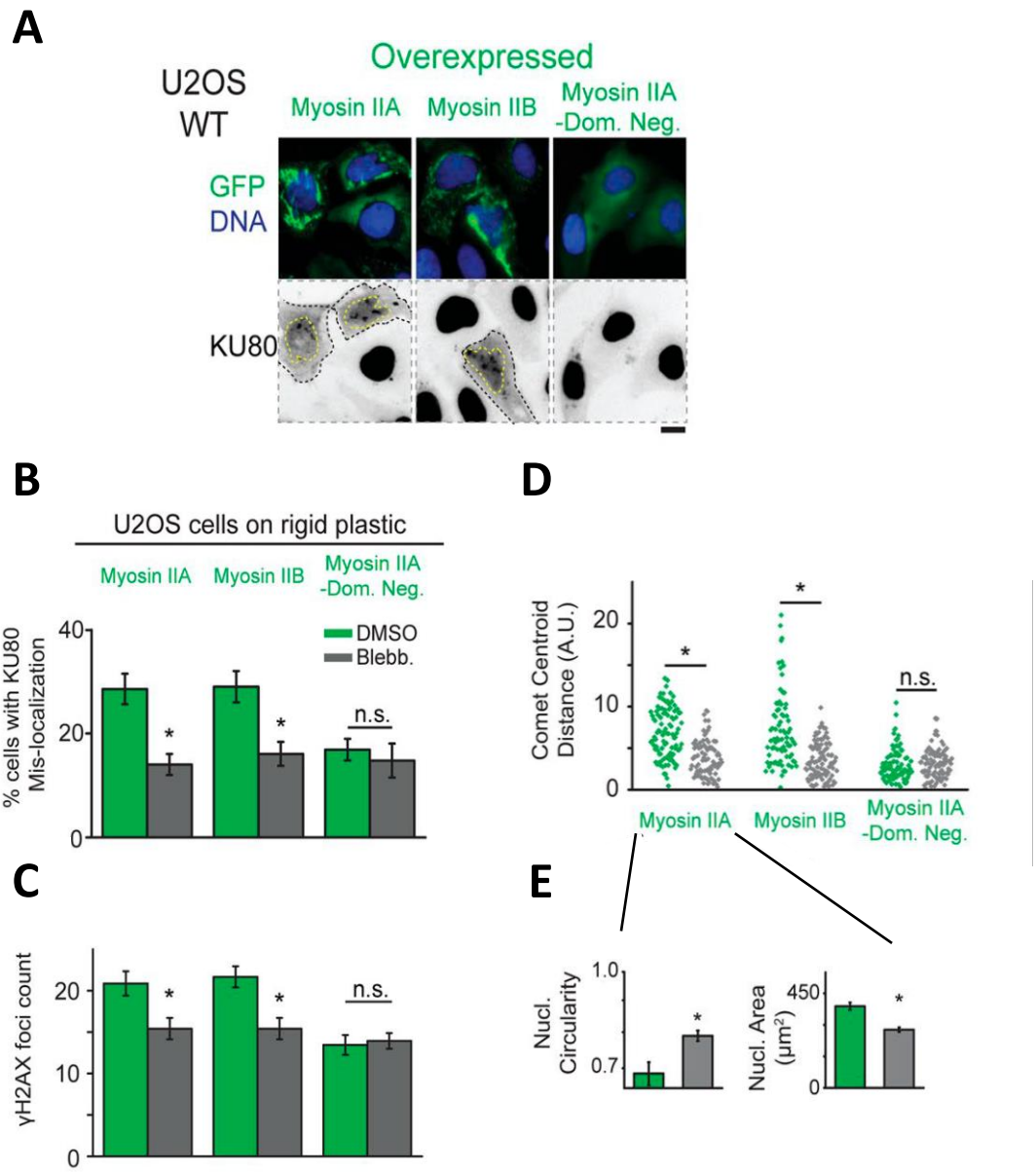

Figure 2.6: Increased actomyosin stress can increase nuclear curvature, frequency of nuclear envelope rupture, and DNA damage. (A)-(B) Compared with dominant-negative mutant (myosin IIA–Y278F) and Blebbstatin, overexpression of myosin IIA or IIB in WT U2OS cells increases nuclear rupture. **(C)-(D)** DNA damage increases in myosin IIA and myosin IIB overexpressed cells, evaluated by both gama-H2AX and comet assay. **(E)** Blebbistatin treatment leads to more rounded nuclei as shown by the increased nuclear circularity and reduced nuclear area (log scale). n > 100 cells per condition in four experiments. *$p < 0.05$; n.s., not significant. Scale bar=10 μm.

myosin II in WT U2OS cells with normal lamin A levels increase the number of cells with ruptured nuclei characterized by mislocalized KU80, in drastic comparison with overexpression of dead mutant Myosin IIA (Fig 2.6).

Moreover, as a result of GFP-myosin overexpression, DNA damage increases as evaluated by both γH2AX foci count and comet assay (Fig. 2.6. C & D). Blebbistatin, as a myosin II inhibitor, can rescue the effect in both cell shape resilience and DNA damage decrease (Fig. 2.6).

2.3 Constricted migration leads to chromosome copy number changes with repetitive NE rupture

3D Constricted migration through limited pore size is another important condition of forming a high curvature spot on the nuclear envelope with temporary depletion of lamin-B, and, therefore, leading to mis-segregation of repair factors. Essentially, all U2OS or A549 cancer cell lines undergo nuclear rupture after small pore constricted

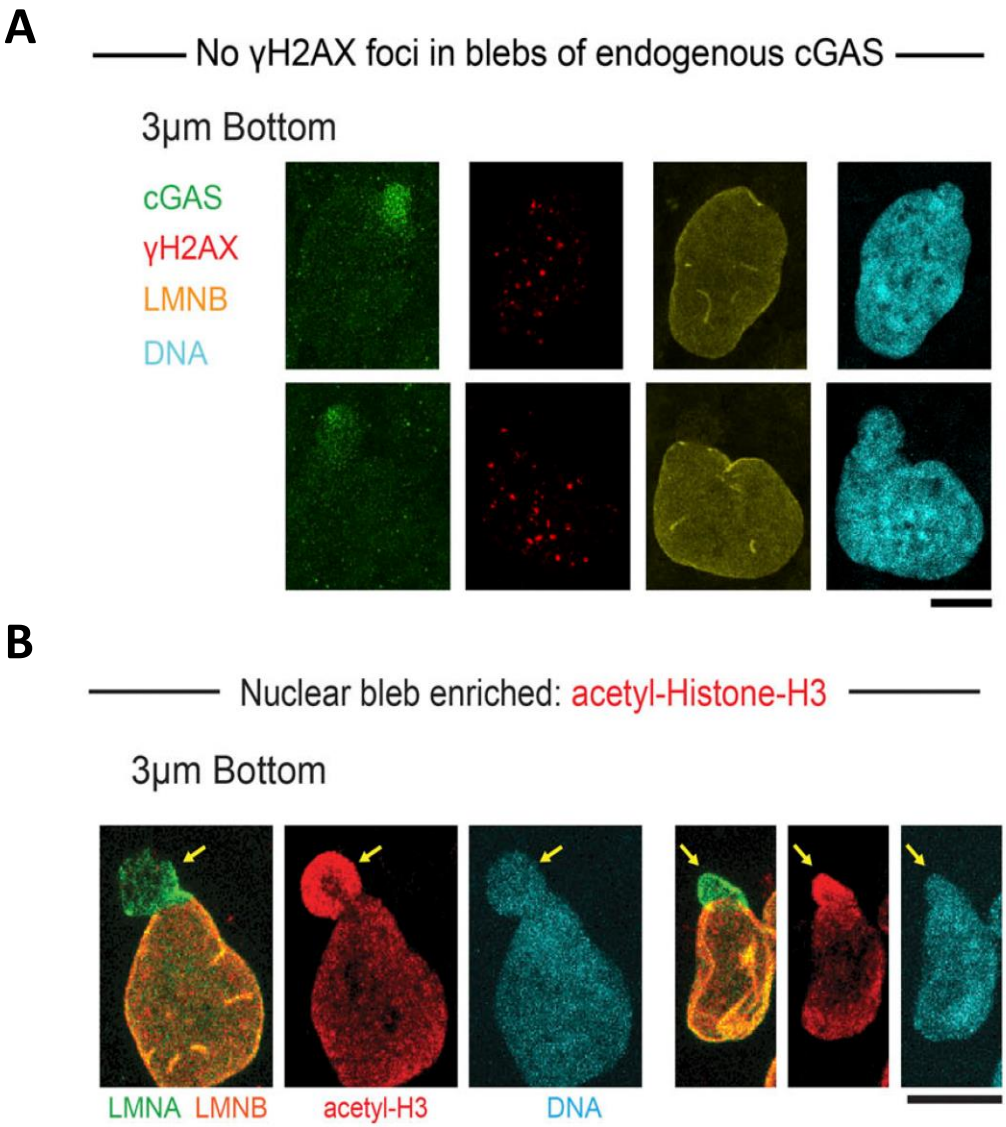

Figure 2.7: Composition of blebs at rupture site. (A) Endogenous cGAS binds to DNA in nuclear blebs, as seen in repre-sentative images of U2OS cells after 3-μm poremigration. DNA damage foci do not localize to blebs, the sites of cGAS accumulation. **(B)** Representative imagesof 3-μm pore–migrated U2OS cells show that nuclear blebs have abundant acetylated chromatin. All scale bars=10 μm.

migration (Irianto et al., 2017), at a much higher degree than perturbed by 2D LMNA knockdown or increased mechanical stress. Anticorrelated distributions of lamin A and B occur at sites of nuclear rupture (also at nuclear poles) during constricted migration (Harada et al., 2014; Denais et al., 2016, 2.7B). The bleb also immunostains for acetyl-histone-H3 (Fig. 2.7B), which is a likely marker of euchromatin (Bannister and Kouzarides, 2011) and could relate to the restricted binding of cGAS--an exo-nuclear DNA degrading factor--to the bleb, reaffirming the broken site where DNA is exposed to extranuclear environment. 3-μm pores have smaller diameter than 8-μm pores and can, therefore, lead to higher curvature of nuclei after cells migrate, which then lead to more repair factor mislocalization and DNA mutation.

Chromosome mis-segregation happens after cycles of constricted migration. A549 cells were migrated three times through either 3 or 8-μm pores, including detachment and expansion, with a final expansion of randomly chosen single cells to ∼1000,000 cells for genomic analyses (Fig. 2.8A). Although all 10 randomly chosen clones obtained after migration through 8-μm pores or from non-migrated 2D control cultures were statistically the same, 3 of 5 clones obtained after migration through 3-μm pores differed significantly from the others and each other (Fig. 2.8B). In previous studies, genome sequencing methodology has been conducted on A549 cell lines undergoing constricted migration for 17 times and conveys distinctive variation in chromosome copy numbers across different clones expanded from single cells (Irianto et al., 2017). Single Nucleotide Polymorphism

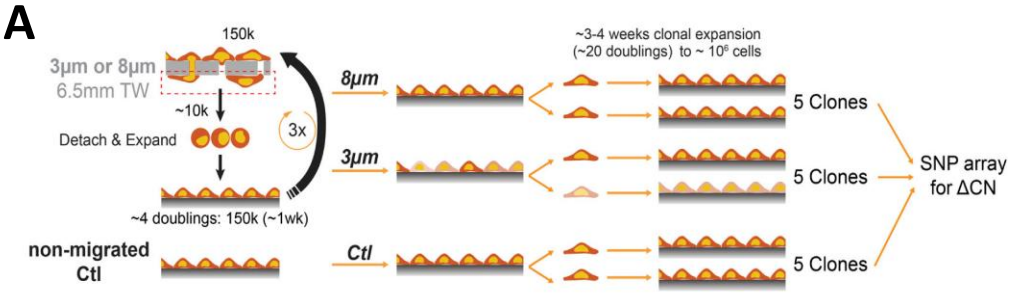
A
150k
3μm or 8μm
6.5mm TW
~10k
Detach & Expand
3x
~4 doublings: 150k (~1wk)
non-migrated
Ctl
8μm
3μm
Ctl
~3-4 weeks clonal expansion
(~20 doublings) to ~ 10⁶ cells
5 Clones
5 Clones
5 Clones
SNP array
for ΔCN


B
A549
8μm clone1
3μm clone1
3μm clone2
8μm clone2
8μm clone3
Ctl clone1
Ctl clone2
Ctl clone3
Ctl clone4
8μm clone4
Ctl clone5
3μm clone3
3μm clone4
3μm clone5
100 Mb
ΔCN
ΔLOH
n.s.
}*
}*
}*

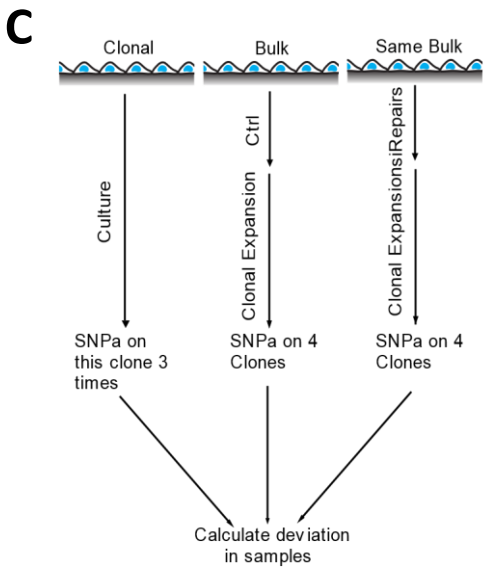
C
Clonal
Bulk
Same Bulk
Culture
Ctrl
Clonal Expansion
siRepairs
Clonal Expansion
SNPa on
this clone 3
times
SNPa on 4
Clones
SNPa on 4
Clones
Calculate deviation
in samples

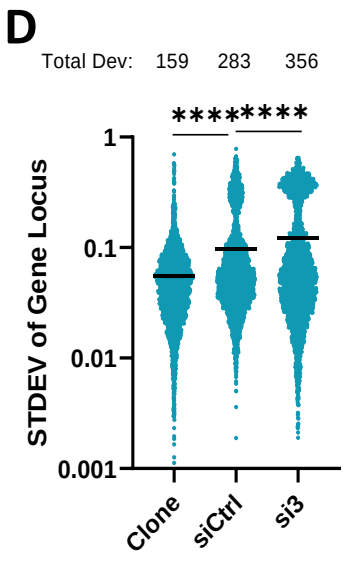
D
Total Dev: 159 283 356
****
STDEV of Gene Locus
1
0.1
0.01
0.001
Clone
siCtrl
si3

Figure 2.8: (Previous page) **Constricted migration and repair factor knockdown both lead to genomic variation based on SNP array. (A)** Schematics: A549 cells were subjected to three rounds of Transwell migration through 3- or 8-µm pores to test the hypothesis that at least some DNA damage would be survivable but misrepaired. Nonmigrated control clones were expanded in parallel. From among these thrice-migrated or nonmigrated cells, the genomes of multiple single cell–derived clones were quantified by SNP array analysis. Time span and doublings for each step are indicated. **(B)** Compared with a clone that migrated three times through 8-µm pores, significant chromosome copy number changes (ΔCN) and loss of heterozygosity (ΔLOH) above the noise level (40 Mb) are observed in three of five A549 clones that migrated through 3-µm pores. Clones are listed per hierarchical clustering of their ΔCN, and the asterisk indicates statistical significance in the overall distribution of gains (red) and losses (green); *$p< 0.05$ in Kolmogorov-Smirnov (KS) test (see Materials and methods, Genome (SNP array) analysis for details), n.s., not significant. **(C)** Schematics: A549 cells (bulk culture) were subjected to Knockdown of repair factors (si3) or Knockdown vehicle Ctrl (siCtrl), 4 clones from each condition were randomly picked, expanded, and performed SNPa as in (B). An arbitrary clone picked from A549 bulk without any perturbation was performed SNP array 3 times, to be used as technical noise basal level. **(D)** Distribution of the standard deviation (STDEV) for all measured gene loci: for each one of the five conditions, the STDEV of the copy number value of each gene locus of the clones' SNPa is calculated. The higher STDEV indicates more genomic and genetic variation. n=2908 Mega Base Pair (Mb) per condition, total number of detectable loci of each 1 million base pairs of genome. Two-tailed t-test with Welch's correction: ****$p < 0.0001$; ns, non-significant.

of A549 Cell Clones extracted from the bulk with repair factor knockdown (si3,knockdown of KU70, BRCA1, and BRCA2), also shows more variation of each gene locus and also copy number variations. Such phenomenon correlates depletion of repair factor with NE rupture through constricted migration (Fig 2.8 C, D, B4). Moreover, si-Repair factors leads to an increase in chromosome mis-segregation during mitosis, a potential cause of aneuploidy (Fig. B5).

2.4 Discussion

Mechanical stress on a strongly bended nucleus is highly likely to trigger nuclear envelope rupture. For medium to high nuclear curvature, lamin A has a protective role under AFM probing (Fig. 2A) and in adherent cells: in particular, shLMNA and Ctrl A549 cells show no significant difference in circularity as a measure of nuclear curvature (Fig. B3), and yet nuclear rupture is favored with low lamin A (Fig. 2.3; Fig. B2; Fig. 2.5; Pfeifer et al., 2017).

External mechanical perturbations like contractility and squeezing interaction imposed by excessive actomyosin function and constricted pore add to the extent to which nuclei bend and form sites with high curvature (Fig. 2.6; Fig. 2.8). The excess DNA damage quantified in this study indeed shows unusual upstream contributions from ECM rigidity and actomyosin contractility via mechanisms involving curvature-induced lamina break and loss of DNA repair factors.

Constricted migration through low-diameter transwell leads to DNA damage, as a result of relatively high curvature imposed on nuclei. Repetitive repair factor mislocalization as a result of cycles of constricted migration causes chromosome copy number changes, because mis-segregation of DNA repair factors with native functions in keeping chromosomal intactness (Difilippantonio et al., 2000; Wang et al., 2005; Irianto,

et al., 2017), and possibly because some chromosomes contain too much mis-repair of their genes to be repaired and kept in the genome anymore. This mimics cancer cells migrating through confined space formed by ECM during metastasis and, finally generating tumor genome variations. The fact that repair factor knockdown can lead to increased chromosome-mis-segregation gives an insight to an important path for cancer mutation.

2.5 Materials and methods

Cell lines and tissue culture

The following cancer cell lines for this study were: A549 lung adenocarcinoma and U2OS osteosarcoma. The A549 and U2OS cell lines were obtained from the American Type Culture Collection (ATCC). A549 cells were cultured in Ham's F-12 media (Gibco 11765047); U2OS cells in DMEM (Gibco, Catalog no. 10569010). All aforementioned cell lines were cultured in media supplemented with 10% (v/v) fetal bovine serum (FBS; MilliporeSigma, Catalog no. F2442) and 100 U ml^{-1} penicillin-streptomycin (Gibco,

Catalog no. 15140122). All cells were passaged every 2-3 days using 0.05% Trypsin/EDTA (Gibco, Catalog no. 25300054). All cell lines were incubated at 37°C and maintained at 5% CO_2.

Immunostaining

Cells were fixed in 4% formaldehyde (MilliporeSigma) for 15 min followed by 15-min permeabilization by 0.5% Triton X-100 (MilliporeSigma), 30-min blocking by 5% BSA (MilliporeSigma), and overnight incubation in primary antibodies at 4°C. The antibodies used include lamin A/C (1:500; mouse; sc-7292; Santa Cruz Biotechnology, Inc.), lamin A/C (1:500; goat; sc-6215; Santa Cruz Biotechnology, Inc.), lamin B (1:500; goat; sc-6217; Santa Cruz Biotechnology, Inc.), γH2AX (1:500; mouse; 05-636-I; MilliporeSigma), 53BP1 (1:300; rabbit; NB100-304; Novus Biological), KU70 (1:500; mouse; sc-17789; Santa Cruz Biotechnology, Inc.), KU80 (1:500; rabbit; C48E7; Cell Signaling Technology), BRCA1 (1:500; mouse; sc-6954; Santa Cruz Biotechnology, Inc.), BRCA2 (1:500; mouse; sc-293185; Santa Cruz Biotechnology, Inc.), cGAS (1:500; rabbit; D1D3G; Cell Signaling Technology). Finally, after 90 min incubation in secondary antibodies (1:500; donkey anti-mouse, -goat, or -rabbit; Thermo Fisher Scientific), the cells' nuclei were stained with 8 μM Hoechst 33342 (Thermo Fisher Scientific) for 15 min. When used, 1 μg/ml phalloidin-TRITC (MilliporeSigma) was added to cells for 45 min just before Hoechst staining

Immunoblotting

Western blotting was performed using standard methods. In brief, cells were briefly trypsinized, washed 3x with cold PBS, and then lysed in RIPA buffer (150 mM NaCl, 1% NP-40 alternative, 0.5% sodium deoxycholate, 0.1% SDS, 40 mM Tris pH 8.0) RIPA buffer containing 1x protease inhibitor cocktail (Sigma, Catalog no. P8340) , and boiled in 1x NuPage LDS sample buffer (Invitrogen, Catalog no. NP0007) with 2.5% v/v β-mercaptoethanol. Approximately 1.0×10^6 cells were used for each analysis. Proteins were separated by electrophoresis in NuPAGE 4-12% Bis-Tris gels run with 1X MOPS buffer (Invitrogen, Catalog no. NP0323) and transferred to an iBlot nitrocellulose membrane (Invitrogen, Catalog no. IB301002). The membranes were cut into strips corresponding to one lane loaded with lysate and one lane loaded with a molecular weight marker and then blocked with 5% nonfat milk in Tris buffered saline (TBS) plus Tween-20 (TBST) for 1h.The membranes were washed with TBST and incubated with 1:500 secondary antibody conjugated with horseradish peroxidase in 5% milk in TBST for 1 h at room temperature with agitation. The membranes were washed again with TBST, then TBS, and developed with a 3,3',5,5'-teramethylbenzidine (TMB) substrate (Genscript L0022V or Sigma T0565). Developed membranes were scanned and analyzed with ImageJ (National Institutes of Health).

Transfection in U2OS cells

All siRNAs used in this study were purchased from GE Healthcare (ON-TAR GETplus SMA RTpool siBRCA1 L-003461-00, 5′-CAA CAU GCC CAC AGA UCAA-3′, 5′-CCA AAG CGA GCA AGA GAAU-3′, 5′-UGA UAA AGC UCC AGC AGGA-3′, and 5′-GAA GGA GCU UUC AUC AUUC-3′; siKU80 L-010491-00, 5′-GCA UGG AUG UGA UUC AACA-3′, 5′-CGA GUA ACC AGC UCA UAAA-3′, 5′-GAG CAG CGC UUU AAC AACU-3′, and 5′-AAA CUU CCG UGU UCU AGUG-3′; siLMNA L-004978-00, 5′-GAA GGA GGG UGA CCU GAUA-3′, 5′-UCA CAG CAC GCA CGC ACUA-3′, 5′-UGA AAG CGC GCA AUA CCAA-3′, and 5′-CGU GUG CGC UCG CUG GAAA-3′; and nontargeting siRNA D-001810-10, 5′-UGG UUU ACA UGU CGA CUAA-3′, 5′-UGG UUU ACA UGU UGU GUGA-3′, 5′-UGG UUU ACA UGU UUU CUGA-3′, and 5′-UGG UUU ACA UGU UUU CCUA-3′), except for si53BP1 (5′-UAU UAC CGU CUC CUC GUUC-3′), which was a gift from R. Greenberg (University of Pennsylvania, Philadelphia, PA; Tang et al., 2013). We do not distinguish between lamin A and lamin C because mice seem equally viable expressing either lamin A or lamin C (Fong et al., 2006; Coffinier et al., 2010). GFP-BRCA1 (71116; Addgene) was a gift from D. Durocher (Lunenfeld-Tanenbaum Research Institute, Toronto, Canada); GFP-LBR was a gift from R.-H. Chen (Academia Sinica, Taipei, Taiwan); GFP-KU70 and GFP-KU80 were gifts from S.L. Rulten (University of Sussex, Brighton, UK; Grundy et al., 2013); and GFP-53BP1 and mCherry-cGAS were gifts from R. Greenberg (Harding et al.,

2017). GFP-LMNA (Swift et al., 2013), GFP-MIIA, GFP-MIIB, and GFP-MIIA-Y278F were all used in our prior research (Shin et al., 2011). Cells were passaged 24 h before transfection. A complex of siRNA oligonucleotides (25 nM) or GFPs (0.2–0.5 ng/ml) and 1 µg/ml Lipofectamine 2000 (Invitrogen; Thermo Fisher Scientific) was prepared according to the manufacturers' instructions and then added for 3 d (siRNAs) or 24 h (GFPs) to cells in corresponding media supplemented with 10% FBS. GFP-3 repair factors consists of GFP-KU70, GFP-KU80, and GFP-BRCA1 (0.2–0.5 ng/ml each). All plasmids are confirmed to produce specific functional proteins by Western blotting or immunofluorescence. Knockdown or overexpression efficiency was determined by immunoblotting or immunofluorescence following standard methods.

GFP-3 rescue experiment

U2OS siLMNA cells were plated on rigid plastic and cultured overnight, and then they were transfected with either GFP-3 (consisting of GFP-KU70, GFP-KU80, and GFP-BRCA1) or GFP-53BP1. A third Ctl sample was not transfected; we refer to these cells as nontreated (NT). After a 24-h transfection period, all cells were fixed and immunostained for γH2AX, and the NT sample was additionally immunostained for KU80. Cytoplasmic GFP signal (or KU80 signal in the NT case) was used to identify ruptured nuclei. Foci of γH2AX were counted for ruptured and nonruptured nuclei in all three samples.

Alkaline comet assay

The assay was performed according to manufacturer instructions (Cell Biolabs). First, cells were detached, mixed with liquefied agarose at 37°C, deposited on a specially treated glass slide, and dried for 15 min at 4°C. Next, the glass slide, containing cells in agarose gel, was incubated in lysis buffer for 45 min and alkaline solution for 30 min. Electrophoresis was conducted at 300 mA for 30 min, and then the slide was washed with 70% ethanol and air dried overnight. Finally, DNA dye was applied for 15 min, and epifluorescence images were taken as described above.

Single-nucleotide polymorphism arrays & analysis

Genomic DNA was isolated from a minimum of 3.0×10^5 cells with the Blood & Cell Culture DNA Mini Kit (Qiagen, Catalog no. 13323) per the manufacturer's instructions. In the event that cells were either very rare (such as reporter-negative cells) or had poor viability after FACS enrichment (specifically, iPSCs), genomic DNA was amplified post-extraction using the Illustra Single Cell GenomiPhi DNA Amplification Kit (GE Healthcare Biosciences, Catalog no. 29108107) following the manufacturer's instructions. All DNA samples were sent to The Center for Applied Genomics Core in The Children's Hospital of Philadelphia, PA, for Single Nucleotide Polymorphism (SNP) array HumanOmniExpress-24 BeadChip Kit (Illumina). For this array, >700,000 probes have an average inter-probe distance of ~4kb along the entire genome. For each sample, the Genomics Core provided the data in the form of GenomeStudio files (Illumina). Chromosome copy number and LOH regions were analyzed in GenomeStudio by using

cnvPartition plug-in (Illumina). Regions with one chromosome copy number are not associated with LOH by Illumina's algorithm. Hence, regions with one chromosome copy number as given by the GenomeStudio are added to the LOH region lists. SNP array experiments also provide genotype data, which was used to give Single Nucleotide Variation (SNV) data. In order to increase the confidence of LOH data given by the GenomeStudio, the changes in LOH of each chromosome from each sample were cross referenced to their corresponding SNV data. After extracting data from GenomeStudio, all data analysis was done on Matlab.

Statistical Analysis

All statistical analyses were performed using Excel (2013; Microsoft).Unless otherwise noted, statistical comparisons were made by unpaired two-tailed Student's t tests. Unless mentioned, all plots show MEAN ± SEM. n indicates the number of samples, cells, wells, etc. quantified in each experiment.

Chapter 3

Live cell chromosome loss reporter system

Fig. 3.1 has been recorded in Live cell monitoring for factors affecting genome variation, *Biorxiv*, 2018, by Xia, Y., Zhu, K., Irianto, J., Andrechak, J.C., Dooling, L.J., Pfeifer, C.R., Discher, D.E.. Fig. 3.1 A was drawn by Dr. Yuntao Xia; all cancer cell line (A549, U2OS, H23) gene editing tag fluorescent chromosome except for A549-RFPLMNB1, and some treatments and flow cytometry in Fig. 3.3 were conducted by Brandon Hayes. Dr. Jerome Irianto developed the code for SNPa in Fig. 3.2. Kuangzheng Zhu conducted imaging of Fig. 3.1 B, validated all reporters, and conducted some treatments and flow cytometry in Fig. 3.3.

3.1 Design and validation of reporter

To visualize loss of a chromosome and address possible external causes in live circumstances, especially biophysical in this study, as well as viability and heritability, a candidate constitutive gene on one copy of any chosen chromosome (monoallelic) is first gene-edited (with CRISPR or Zinc Finger) as a fluorescence protein fusion (Fig.3.1A). A constitutive gene expresses protein that isn't silenced epigenetically or is expressed at different levels in different stages of cell cycle. In other words, it expresses the target protein all the time within a cell. Normal regulation of expression can help avoid epigenetic silencing of a gene, and proper protein localization helps maintain normal physiology while avoiding confusion with autofluorescence. Subsequent loss of fluorescence that occurs spontaneously or by various chemical or mechanical perturbations can be tracked by single cell expansion (Fig.3.1B) or flow cytometry for reporter-negative cells, and a constitutive gene is positively identified when allele loss is documented by methods including genome array-based methods and single cell sequencing, as well as proved with traditional techniques such as karyotyping and PCR which, however, involve cell denaturation (Fig.3.2 A, Fig. C1).

Many non-constitutive genes with their proteins are tested, such as histone-H2B (Chr-6) and beta-CTNNB1 (Chr-3, Fig. 3.2 B, Fig.C3). These genes do not show chromosome loss in fluorescence-negative populations and therefore are not candidates for the reporters. Moreover, selective growth of pre-existing subpopulations rather than

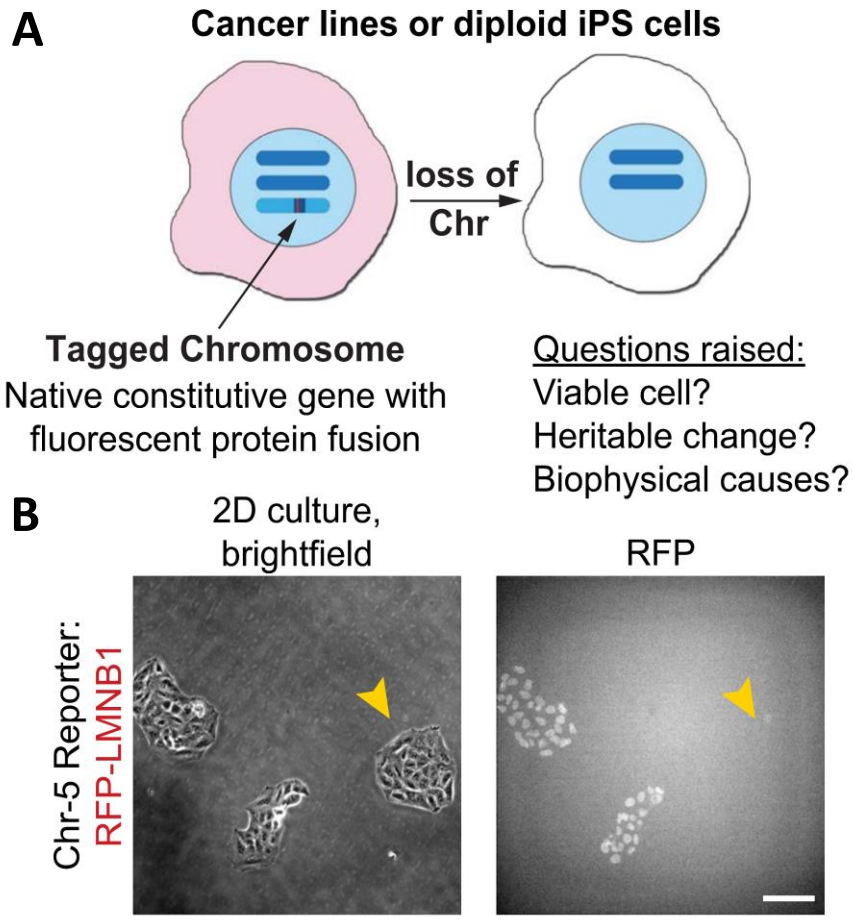

Figure 3.1: Concept of Chr-loss cell reporter. (A) Live cell chromosome reporter concept, which requires identifying alleles that are constitutively expressed even when fused to GFP or RFP. **(B)** RFP-positive and RFP-negative A549 colonies using the Chr-5 reporter in which one allele of *LMNB1* has an N-terminal RFP. A549 cells were sorted to purity via FACS, plated sparsely, and allowed to grow for a week. Scale bar = 100 µm.

de novo genetic or epigenetic change is always a concern in studies of rare cells, with initial kinetics being key to mechanism.

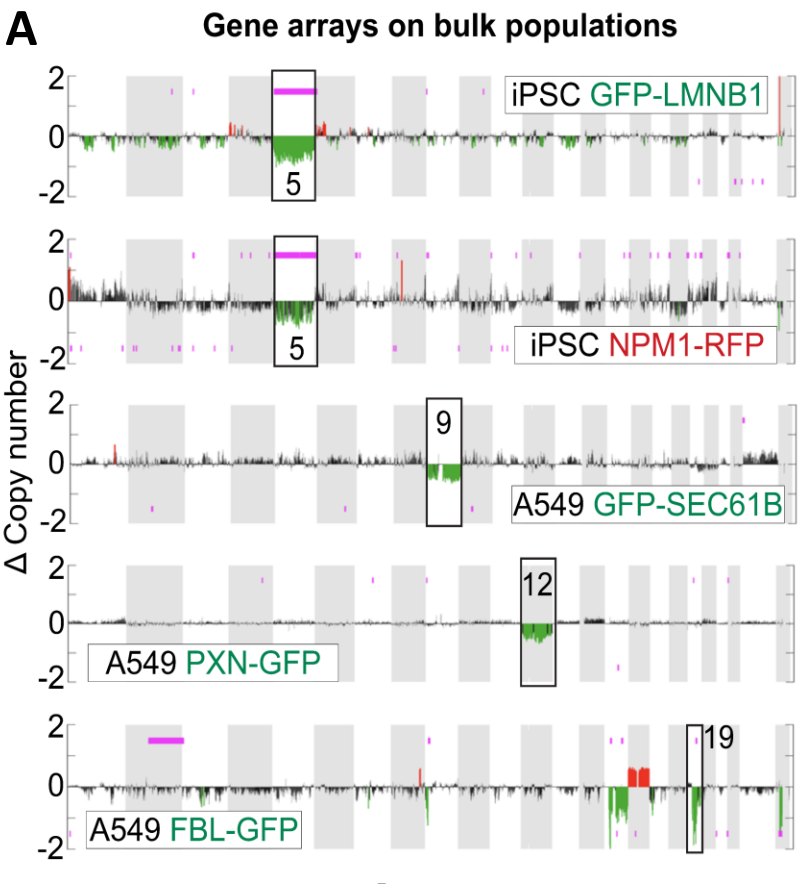

Figure 3.2: SNPa validation on Chr-loss reporters. (A) Bulk DNA from sorted reporter-pos and -neg cells was analyzed on single nucleotide polymorphism arrays (SNPa), with differences shown and independently duplicated for normal diploid induced pluripotent stem cells (iPSCs) and hypotriploid A549 lung adenocarcinoma cells. Loss of Heterozygosity (LOH) is indicated in purple.

B

Chromosome	Target locus	Tested cell lines
Validated, constitutive loci for reporter		
5	LMNB1	iPSC, A549, H23, U2OS
5	NPM1	iPSC
9	SEC61B	iPSC, A549
12	PXN	A549
19	FBL	iPSC, A549
Non-constitutive loci - not functional for reporter		
1	TOMM20	A549
3	CTNNB1	A549
6	HIST1H2BJ	A549
19	AAVS1	A549, U2OS

(B) Chr reporter designs tried for various loci and cell lines. Non-constitutive loci show fluorescence loss but fail to show chromosome loss in genetic analyses..

Even a first set of images after a fresh sort of RFP-pos cells showed similar sized colonies of RFP-neg and RFP-pos cells (Fig.3.1B, C1), consistent with natural, spontaneous creation of genetically distinct cells.

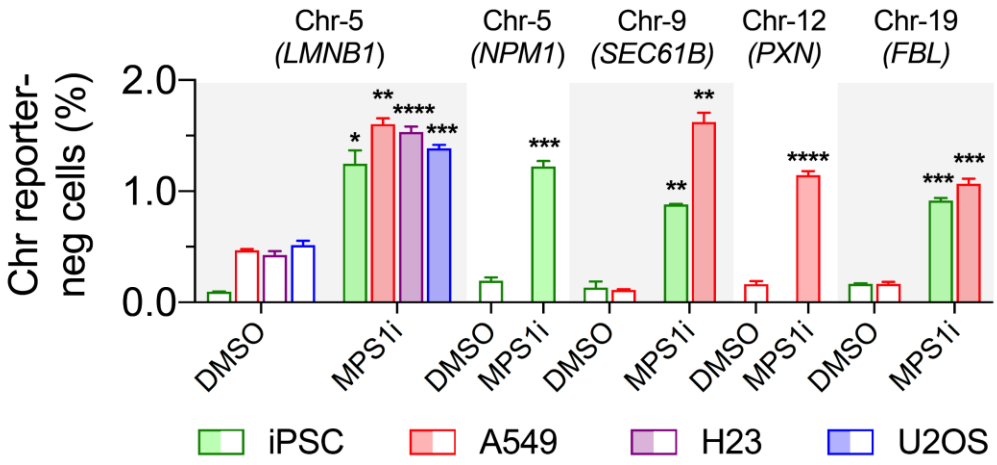

Figure 3.3: MPS1i validation of Chr-loss reporter system. Chr reporter-neg cells for all engineered lines with reporters (iPSCs, A549, H23 lung adenocarcinoma, and U2OS osteosarcoma) treated with MPS1i or DMSO control for 3 days. n = 3 replicates per condition; unpaired two-tailed t-test with Welch's correction between each MPS1i-treated and its corresponding DMSO control. *$p < 0.05$, **$p < 0.005$, ***$p < 0.0005$, ****$p < 0.0001$.

with Brandon Hayes

One or more constitutive genes were consistently identified on Chromosomes (Chr) 5, 9, 12, and 19 as well as dual-tagged combinations (Fig.3.2, C2, C4), and double chromosome loss from fluorescence-double negative cells are detected

and verified (Fig.3.2, C4), which indicates the multiplexity and universality of the system. MPS1 inhibitor reversine is known to lead to genomic instability by increasing chromosome mis-segregations during mitosis when spindle assembly checkpoint is bypassed. After treatment of the inhibitor, reporter cells show gigantic increase in reporter-neg% (Fig. 3.3), further confirming that the reporter evaluates the degree of chromosome loss.

3.2 Discussion

Based on the CRISPR/Cas9 gene editing methodology (Fig. 3.1, 3.2, C1, C2), live cell chromosome-loss reporter system is ubiquitously applicable on all cells and chromosomes. The current well-established non-overlapping fluorescence wavelengths of microscope and flow cytometry generally allow 4 channels with different colors (BFP, GFP/YFP, RFP, far-red) (Cossarizza et al., 2017; Lin et al., 2015), for which, theoretically, a maximum of 4 non-homologous chromosomes can be engineered using the reporter system given its multiplexity. Since human cells have 22 non-homologous autosomes, 4 chromosomes can cover one fourth of the genome, providing a giant range of studying

genomic variation in cancer or normal cell lines. Any perturbations, including chemical and physical, described above, can be applied to reporter cells with a readout as to how many fluorescence-neg individuals occur as a result. In this case, thousands of black-box assays can be performed with the reporter cells exposed to a series of chemicals, siRNAs, and physical conditions, respectively, to find out their reporter-neg% compared to corresponding control groups. In the end, interesting results can then be traced back to discover the mechanisms hidden within black boxes. For instance, if a chemotherapy drug, when applied on Chr-9 reporter A549 cell, shows an increase in reporter-neg%, this indicates the drug favors production of Chr-9 loss cells which somehow resist to the drug and can continue to grow. Multiplexed reporter cells, on the other hand, can present the increase and decrease in many chromosomal losses, and provide a broader general picture of genomic variation on the perturbations applied.

Nevertheless, gain of chromosomes tagged with constitutive genes expressing fluorescence cannot be accurately pinpointed, traced, and isolated with this system. The loss of fluorescent protein signal introduces a cell without nuclear or cytoplasmic signal under microscope, or a cell with multiple orders of magnitude lower signal compared to reporter-positives in flow cytometer, because fluorescent protein is no longer expressed as a result of the loss of a chromosome carrying its gene. Obtaining a reporter chromosome from abnormal mitosis doesn’t necessarily translate to a double fluorescence signal,

because protein expression is positively correlated with gene dosage but isn't completely proportional to it (Alberts, 2015). If a certain protein is saturated, increased protein expression can terminate. Even if two alleles of reporter do mean twice the amount of fluorescence protein signal, flow cytometry cannot distinguish the fold change of 2 which falls within the range of noise native to the machine and cell cycle. Therefore, the reporter has limitations in studying chromosome gains. Moreover, since mis-aligned lagging chromosomes usually end up in micronuclei with their genetic materials degraded (Zhang et al., 2015; Liu et al., 2018), loss instead of gain of chromosomes more importantly depicts the CNV after errors in mitosis.

In recent years, it has become popular to directly tag chromosomes with a focal fluorescence signal using the CRISPR/Cas method. Unlike our chromosome loss reporter which reflects the existence of chromosome by the fluorescence carried on the expressed protein, this life-FISH technique lightens the chromosome by itself by complementary base pairing to a sequence with hundreds of nucleotides in the chromosome of interest (Wang et al., 2019; Chen et al., 2020; Ma et al., 2015). Such method has been used prevalently in live cell imaging and chromatin localization/mapping. It isn't difficult to perceive that cells losing the tagged chromosome(s) can be easily identified by high-throughput imaging and would show absolutely zero focal signal, since no lagging period resulting from protein degradation would exist. However, the single focal signal instead of widespread

nucleoplasmic or cytoplasmic signal prevents negative cells from being distinguished from positive cells when flow cytometry is applied, due to the lack of signal in order-of-magnitudes of the former. Therefore, separation of the cells using flow cytometry sorting----one of the most efficient methods for separating cells based on morphology, size, and fluorescence----fails to work. Provided that imaging sample collection covers much lower sample space than the capacity of flow cytometry, our reporter system based on protein expression, which can be functional under both flow cytometry and fluorescence imaging, exhibits its advantage here.

3.3 Materials and methods

Cell lines and tissue culture

The following cancer cell lines for this study were: A549 lung adenocarcinoma, U2OS osteosarcoma, and NCI-H23 lung adenocarcinoma (referred to as H23 in text). The A549 and U2OS cell lines were obtained from the American Type Culture Collection (ATCC). The H23 cell line was a kind gift from Dr. Michael C. Bassik (Stanford University). A549 cells were cultured in Ham's F-12 media (Gibco 11765047); U2OS cells in DMEM (Gibco, Catalog no. 10569010); and H23 cells in RPMI 1640 (Gibco, Catalog no. 11879020). The original A549 RFP-LMNB1 cell line was engineered by Sigma-Aldrich. HEK293T cells used, acquired from ATCC, for lentiviral packaging were also cultured in DMEM. All

aforementioned cell lines were cultured in media supplemented with 10% (v/v) fetal bovine serum (FBS; MilliporeSigma, Catalog no. F2442) and 100 U ml^{-1} penicillin-streptomycin (Gibco, Catalog no. 15140122). All cells were passaged every 2-3 days using 0.05% Trypsin/EDTA (Gibco, Catalog no. 25300054). All cell lines were incubated at 37°C and maintained at 5% CO_2.

The following induced pluripotent stem cell (iPSC) lines were also used, all of which were acquired from the Coriell Institute for Biomedical Research and generated/validated by the Allen Institute for Cell Science: iPSC GFP-LMNB1 (AICS-0013 cl.210), iPSC RFP-LMNB1 GFP-SEC61B (AICS-0059 cl.36), and iPSC FBL-GFP NPM1-RFP (AICS-0084 cl.18). iPSCs were cultured in mTseR Plus medium (STEMCELL Technologies, Catalog no. 05825), with mTser Plus 5X supplement and 100 U ml^{-1} penicillin-streptomycin. For passaging and maintenance of iPSCs, cells were lifted with accutase (Sigma, Catalog no. A6964) at 37°C and re-plated into 10-cm plates (Corning) coated with Matrigel (Corning, Catalog no. 356231) following the Allen Institute of Cell Science's protocol. 10 mM ROCK inhibitor (Y-27632; STEMCELL Technologies, Catalog no. 72302) was added to replated cultures to help with adherence and to prevent differentiation. Passaging was done once iPSC cultures reached 70% confluency to prevent spontaneous differentiation. All iPSC lines were also cultured at 37°C and maintained at 5% CO_2.

Monoallelic chromosome tagging

For all attempted monoallelic chromosome reporters as described in Fig. 1E, all donor constructs were a gift from Allen Institute of Cell Science: AICSDP-8:TOMM20-mEGFP (Addgene plasmid #87423; http://n2t.net/addgene:87423; RRID:Addgene_87423), AICSDP-13:FBL-mEGFP (Addgene plasmid #87427; http://n2t.net/addgene:87427; RRID:Addgene_87427), AICSDP-35:AAVS1-mEGFP (Addgene plasmid #91565; http://n2t.net/addgene:91565; RRID:Addgene_91565), AICSDP-42:AAVS1-mTagRFPT-CAAX (Addgene plasmid #107580; http://n2t.net/addgene:107580; RRID:Addgene_107580), AICSDP-1:PXN-EGFP (Addgene plasmid #87420; http://n2t.net/addgene:87420; RRID:Addgene_87420), AICSDP-10:LMNB1-mEGFP (Addgene plasmid #87422; http://n2t.net/addgene:87422; RRID:Addgene_87422), AICSDP-52: HIST1H2BJ-mEGFP (Addgene plasmid #109121; http://n2t.net/addgene:109121 ; RRID:Addgene_109121), AICSDP-7:SEC61B-mEGFP (Addgene plasmid # 87426; http://n2t.net/addgene:87426; RRID:Addgene_87426).

All knock-in reporter lines were generated following the protocol established in (1) using CRISPR/Cas9 technology. Donor plasmids were designed such that unique designs for each target locus contain 5’ and 3’ homology arms (1 kb each) for the desired insertion site, based on the GRCh38 reference human genome. For editing, we use the ribonucleic protein (RNP) method with recombinant wild type *S. pyogenes* Cas9 protein pre-complexed with a synthetic CRISPR RNA (crRNA) and a trans-activating crRNA

(tracrRNA) duplex. Recombinant wild-type Cas9 protein was purchased from the University of California–Berkeley QB3 Macrolab, while crRNA and tracrRNA oligonucleotides were designed by and purchased from Horizon Discovery. For transfection of donor templates into target cells, we used the electroporation using a Gene Pulser Xcell Electroporation System (Bio-Rad). 700,000 targets cells were lifted using 0.05% Trypsin/EDTA, resuspended in 200 ul of fresh media without penicillin-streptomycin, and loaded into a 0.4-cm cuvette. 4 µL of both 10 µM crRNA:tracrRNA duplex and 10 µM recombinant Cas9 protein were added to the cell solution, as well as 8 µg of donor plasmid. Electroporation conditions were as follows: (1) A549 and H23: 200V with 45 ms pulse length using a square-wave protocol; (2) U2OS: 160V with 30 ms pulse length using a square-wave protocol. After electroporation, cells were allowed to expand for ~1 week and then enriched via fluorescence-activated cell sorting (FACS), as described below. 3-5 FACS enrichment cycles were performed to achieve a pure reporter-positive population.

Single-cell CNV-sequencing and analysis.

A549 cells from RFP-pos clone-3, RFP-neg clone-1 and RFP-neg clone-2 were plated in a 24 well plate at 60,000 cells per well and cultured for 2 days. RFP-pos clone-3 was used as the reporter-positive sample, and a 1:1 mixture of the two reporter-negative clones served as the overall reporter-negative sample. The DNA library was constructed using the

Chromium Single Cell CNV kit from 10X Genomics (Catalog no. PN-1000041; PN-1000057; PN-1000032; PN-1000036, Pleasanton, CA) per the manufacturer's instructions. The libraries were submitted to the University of Pennsylvania's Next Generation Sequencing Core (12-160, Translational Research Center, University of Pennsylvania) for sequencing using HiSeq 4000, 150 bp paired-end from Illumina (San Diego, CA). For each sample, the copy number data was generated using Cell Ranger DNA pipeline (10X Genomics) and was visualized using Loupe scDNA Browser (10X Genomics). The data were then exported to Python to remove the noise. Cells that were flagged as "noisy" by the Cell Ranger pipeline were removed from further analysis. Cells with more than 69 copies of chromosomes were removed from the CNV analysis to avoid potential influence of cell cycle effects. Built-in hierarchical clustering from 10X Genomics was also used to rearrange the cells.

Cell type annotations

Raw expression matrices were used as the input for the singleR (1.4.1) package (Aran et al., 2019). The cell types were annotated based on Human Primary Cell Atlas (Mabbott et al., 2013).

Karyotyping

Cells used for karyotyping were plated in T25 flasks (Corning), cultured for 2-3 days to reach ~50% confluency. The media was then discarded and replaced with fresh media to fill the entire flask with a closed lid, after which the flask was wrapped with parafilm. The samples were then sent to Cell Characterization Services for metaphase-spread karyotyping.

Polymerase chain reaction (PCR) for reporter validation

DNA was extracted as previously described for SNP arrays. The isolated DNA was then mixed with materials from KAPA HiFi PCR Kit (Roche, Catalog no. 07958838001) to start each PCR reaction. Each reaction contains 5 µL 5X HiFi Fidelity Buffer, 0.75 µL 10 mM KAPA dNTP Mix, 0.5 µL 1U/µL KAPA HiFi DNA Polymerase, 0.75µL of 10 µM forward and reverse primers, respectively, and 1 ng of extracted DNA template. PCR grade water was then filled up to 25µL. All materials suggested by the kit were placed on ice prior to mixing. The reaction mix was placed on the thermocycler with the following temperature cycling protocol: Initial denaturation at 95^{o}C for 3 min; 35 cycles of denaturation at 98^{o}C for 20 sec, annealing at 65^{o}C for 15 sec, extension at 72^{o}C for 60 sec/kb; and final extension at 72^{o}C for 1 min. All PCR products were then run on a 1% (v/v) agarose (Invitrogen, Catalog no. 16500500) gel at 100V for 1h and then imaged using a ChemiDoc MP Imaging System (Bio-Rad, Catalog no. 17001402).

Reporter validation via single-nucleotide polymorphism arrays & analysis

Genomic DNA was isolated from a minimum of 3.0×10^5 cells with the Blood & Cell Culture DNA Mini Kit (Qiagen, Catalog no. 13323) per the manufacturer's instructions. In the event that cells were either very rare (such as reporter-negative cells) or had poor viability after FACS enrichment (specifically, iPSCs), genomic DNA was amplified post-extraction using the Illustra Single Cell GenomiPhi DNA Amplification Kit (GE Healthcare Biosciences, Catalog no. 29108107) following the manufacturer's instructions. All DNA samples were sent to The Center for Applied Genomics Core in The Children's Hospital of Philadelphia, PA, for Single Nucleotide Polymorphism (SNP) array HumanOmniExpress-24 BeadChip Kit (Illumina). For this array, >700,000 probes have an average inter-probe distance of ~4kb along the entire genome. For each sample, the Genomics Core provided the data in the form of GenomeStudio files (Illumina). Chromosome copy number and LOH regions were analyzed in GenomeStudio by using cnvPartition plug-in (Illumina). Regions with one chromosome copy number are not associated with LOH by Illumina's algorithm. Hence, regions with one chromosome copy number as given by the GenomeStudio are added to the LOH region lists. SNP array experiments also provide genotype data, which was used to give Single Nucleotide Variation (SNV) data. In order to increase the confidence of LOH data given by the GenomeStudio, the changes in LOH of each chromosome from each sample were cross referenced to their corresponding SNV data. After extracting data from GenomeStudio, all data analysis was done on Matlab.

Flow cytometry and FACS

All flow cytometry was performed on a BD LSRII (Benton Dickinson) and analyzed with FCS Express 7 software (De Novo Software). All studied cell lines were detached by brief trypsinization (for all cancer lines in 2D culture) or with accutase (for iPSCs), washed, and resuspended in FACS buffer (PBS + 5% FBS) with 1.0 µg ml^{-1} DAPI (MilliporeSigma, Catalog no. 09542). For fluorescence-activated cells sorting, or FACS, cells were prepared in the same way as described above except that freshly prepared sterile FACS buffer was used and no DAPI was included. FACS was performed on either a BD FACS Aria II or a BD FACS Jazz. Prior to any assay that assessed reporter-negative subpopulation generation, cells were FACS-enriched for only reporter-positive cells.

For gating, forward scatter parameters FSC-A vs. FSC-H and side scatter parameters SSC-A vs. SSC-H were used to remove aggregates from analysis. Live cells were gated on using forward scatter and side scatter (FSC-A vs. SSC-A). DAPI was further used to discriminate between live cells and debris/dead cells.

Treatment

For all cancer cell treatments, either 300,000 cells were plated per well in a 6-well plate (Corning) or 60,000 cells per well in a 24-well plate (Corning). For iPSC treatments, 60,000 cells were plated per 6-well plate. MPS1 inhibitor reversine (Cayman Chemical,

Catalog no. 10004412) and dimethyl sulfoxide (DMSO; Millipore Sigma, Catalog no. D2438) were used for treatment. The reversine concentrations and treatment times used, unless otherwise stated, are: for A549, 0.1 μM for 72h; for U2OS and H23, 1.5 μM for 24h followed by washout and 48h recovery; for iPSCs, 0.25 μM for 24h followed by washout and 24-48h recovery.

Immunoblotting

Western blotting was performed using standard methods. In brief, cells were briefly trypsinized, washed 3x with cold PBS, and then lysed in RIPA buffer (150 mM NaCl, 1% NP-40 alternative, 0.5% sodium deoxycholate, 0.1% SDS, 40 mM Tris pH 8.0). RIPA buffer also contained 1X protease inhibitor cocktail (Millipore Sigma, Catalog no. P8340). After lysis, centrifugation was done to discard lipids and other contaminants. Samples were then boiled in 1X NuPage LDS sample buffer (Invitrogen, Catalog no. NP0007) with 2.5% v/v β-mercaptoethanol. Approximately 1.0×10^6 cells were used for each analysis. Proteins were separated by electrophoresis on NuPAGE 4-12% Bis-Tris gels run with 1X MOPS buffer (Invitrogen, Catalog no. NP0323) and transferred to an iBlot nitrocellulose membrane (Invitrogen, Catalog no. IB301002). The membranes were cut into strips corresponding to one lane loaded with lysate and one lane loaded with a molecular weight marker and then blocked with 5% nonfat milk in Tris buffered saline (TBS) plus Tween-20 (TBST) for 1h. The membranes were washed with TBST and incubated with 1:1000 primary antibody (anti-LMNB1 (Abcam, Catalog no. ab16048), anti-beta-actin (santa

Cruz, Catalog no. sc-47778) overnight.The membranes were washed with TBST and incubated with 1:2000 secondary antibody conjugated with horseradish peroxidase in 5% milk in TBST for 1 h at room temperature with agitation. The membranes were washed again with TBST, then TBS, and developed with a 3,3',5,5'-tetramethylbenzidine (TMB) substrate (Genscript L0022V or Sigma T0565). Developed membranes were scanned and analyzed with ImageJ (National Institutes of Health).

Imaging

Epifluorescence imaging was performed using an Olympus IX71 with a digital camera (Photometrics) and a 20x/0.4 NA objective.

Data reporting

Statistical methods were not used to predetermine sample size. The experiments were not randomized. Investigators were not blinded to allocation during experiments and outcome assessment.

Statistics and reproducibility

The statistical methods for each experiment are included in the corresponding Figure legends. All statistical analyses were done on GraphPad Prism 9.0. All experiments were biologically repeated and confirmed. Unless otherwise mentioned, all plots show MEAN±

SEM, and statistical comparisons are considered significant if $p<0.05$. n indicates the number of samples, cells, wells, etc. quantified in each experiment. Additionally, at least two separate investigators performed each experiment separately for reproducibility.

Chapter 4

Mitosis under confinement leads to viable and heritable descendants, results from mechanically triggered MT mis-attachment, and is protected by Myosin II

Fig. 4.1, 4.8 F were designed by Dr. Dennis Discher and drawn by Brandon Hayes. Brandon Hayes conducted some analyses and flow cytometry for Fig. 4.4 A, performed some confinement assays in Fig. 4.4 C-D, conducted experiments for MPS1i treatment in Fig. 4.5, analyzed Chr-5 reporters in Fig. 4.7 C, contributed half to Fig. 4.10 A, and performed confinement assays for Fig. 4.10 D; Mai Wang contributed some replicated data to Fig. 4.4 A, and performed RNA sequencing in Fig. 4.9 A. Junhong Du performed some confinement assays in Fig. 4.4 C-D, analyzed Chr-9 reporters in Fig. 4.7 C; Kuangzheng Zhu conducted Fig. 4.2, 4.3, 4.6, 4.8, Fig.4.4 B, 4.5 A-B, 4.7 A-B, 4.9 B-D, 4.10 B-C, conducted some analyses and flow cytometry for Fig. 4.4 A, performed some confinement assay in Fig. 4.4 C-D, did all data fitting in Fig. 4.5, analyzed Chr-19 reporters in Fig. 4.7 C, prepared cells for Fig. 4.9 A, contributed half to Fig. 4.10 A, performed control experiments for Fig. 4.10 D.

4.1 Introduction

Mechanical aspects of a cell's microenvironment such as matrix stiffness and 3D rigid confinement can exert diverse effects on a cell in mitosis as well as interphase, including changes in cell shape and key cytoskeletal and nuclear structures (Uhler and Shivashankar, 2017; Nava et al., 2020; Przybyla et al., 2016; Paszek et al., 2014; Segel et al., 2019; Meng et al., 2018; Engler et al., 2006;Petridou et al., 2021). Normal tissue cells nonetheless seem to show genetic differences *within* the same person (Yizhak et al., 2019), and such variation *across different tissues* positively correlates with microenvironment stiffness *E* of each tissue (Swift et al., 2013; Pfeifer et al., 2017). In our previous studies (Chapter 2, Irianto et al., 2017), we showed that constricted migration, as mimicking the environment of extracellular matrix in stiff tissues, causes nuclear envelope rupture and repair factor mislocalization, yielding DNA damage. However, chromosome gains or losses (Δ) contribute to cancer variation even more than point mutations in DNA. A recent study of medulloblastoma, for example, shows that the most frequently detected mutation (in *MYC*) occurs in only 17% of patients whereas every one of more than a dozen copy number changes occur in more than 30% of patients (Northcott et al., 2017). In clinical trials by Yamanaka and colleagues on two aged patients (>65 yrs), induced pluripotent stem (iPS) cells generated from one of the patients exhibited copy number variations that prevented their use for fear of carcinogenesis (Mandai et al., 2017). Such trends motivate

the hypothesis that mitosis within rigidly confining 3D microenvironments favors *heritable mechanogenetic* changes.

Mechanical contributions to changes in a cell's DNA sequence seem reasonable to infer from recent studies of myosin-II, which is key to animal cell mechanosensing of microenvironments (Parajón et al., 2021;Stewart et al., 2011; Sedzinski et al., 2011; Rancati et al., 2008) and to driving mitotic rounding (Ramanathan et al., 2015). In yeast and non-adherent cells, myosin-II also drives cytokinesis, and deletion of myosin-II somehow leads to multiple chromosomal gains and losses in viable yeast (Rancati et al., 2008), which indicates that myosin-IIA protects the genome. Interestingly, mouse knockdowns of nonmuscle myosin-IIA within dense 3D tissues such as skin induces squamous cell carcinoma in embryos (Schramek et al., 2014; Conti et al., 2015), and since most cancers typically involve multiple genetic changes (Davoli et al., 2013; Tomasetti and Vogelstein, 2015), myosin-IIA knockdown could be a key initiator that couples to microenvironment. Indeed, while a rigid cell wall shelters yeast from mechanical stresses and microenvironments, abnormal 3D tissue architectures have been observed with mouse and human cells to enhance chromosome mis-segregation (Knouse et al., 2018). For an isolated mitotic animal cell, strong compression between two rigid surfaces distorts the mitotic spindle and increases mis-segregation relative to standard 2D cultures - but such squashing also kills cells (Dumont and Mitchison, 2009; Lancaster et

al., 2013). Whether 3D microenvironments including rigid confinement can exert heritable mechanogenetic effects is thus unclear.

To address such issues, we first identify GFP/RFP tagged genes that are suitable as live-cell reporters. Visualizing an individual cell *before*, *during*, *and after* a genetic change can provide key evidence of viability and heritability that is at best inferred from sequencing approaches which require cells to be killed for nucleic acid extraction----as conducted in our previous studies (Fig. 2.8). Rare changes (e.g. ~0.1 to 1% of cells) are also a challenge for sequencing, in part because of error rates (Yizhak et al., 2019), but an initially rare change is the causal origin for any sub-population of viable, non-senescent cells that emerges via subsequent selection and competitive expansion. For a normal cell type, we focus on induced Pluripotent Stem cells (iPSC's) as a model stem cell relevant both to tumor and tissue stem cells and to major concerns over Chr instability in pluripotent cells (Mandai et al., 2017; Skamagki et al., 2017). We also study several solid tumor derived lines (A549 and H23 lung adenocarcinomas, and U2OS osteosarcoma). Heritable changes are ultimately shown in live viable cells to be a genuinely genetic form of mechanotransduction from stiff 3D microenvironments, with a surprisingly diminished role for a mitotic checkpoint but significant contributions from chromosome compaction and actomyosin.

4.2 Confined mitosis causes chromosome loss

Confined mitosis lengthens the MT spindle and increases abnormal divisions relative to mitotic rounding in standard 2D cultures (Dumont and Mitchison, 2009; Lancaster et al., 2013; Cadart et al., 2014), but applied confinement can also kill many cells (Fig.4.1, 4.2, D4). Viability of cells that have lost or gained Chr's in confined mitosis has thus been unclear and is of concern given the toxicity of pertinent drugs such as MPS1i. Physiological relevance of confined mitosis has also been unclear, and so mitotic cells in human-in-mouse xenografts were 3D-imaged by confocal microscopy. Mitotic chromatin and interphase nuclei show the same height in iPSC-derived teratomas and A549 tumors -- unlike standard 2D cultures (Fig. 4.3). The teratomas have palpable rigidity similar to the tumors, which are not only collagen rich and stiff (~5 kPa) (Swift et al., 2013).

To assess the *in vitro* effects of rigid confinement on Chr reporters in cells dividing in culture, we applied a ring-weight on top of an upper glass coverslip after sparsely mixing rigid polystyrene microbeads with the cells so as to limit the compression. Confinement even for ~8h suffices to increase abnormal mitosis in terms of evident chromosome mis-segregation (Fig.4.3). Recovery in 2D culture for 16-48h was followed by flow cytometry quantitation and also sorting to verify Chr-loss (Fig.4.4 C). Reporter loss of ~1% after

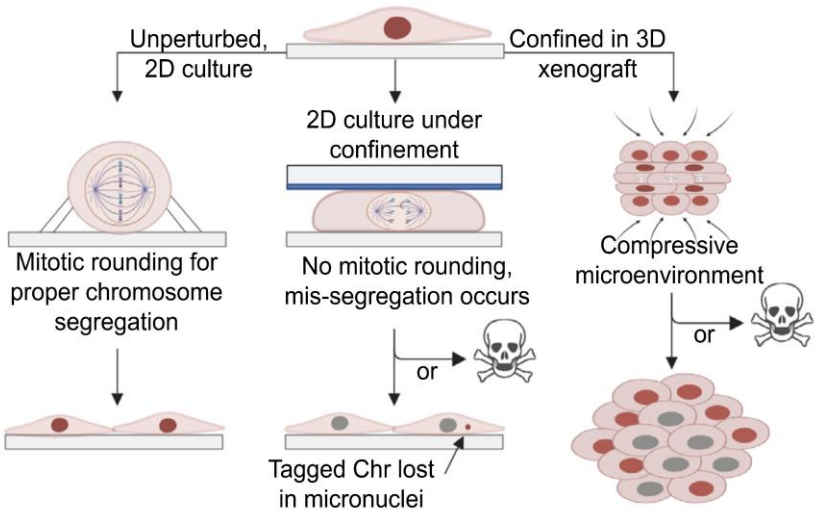

Figure 4.1: Schematic of confinement on Chr-loss reporter cells. Mitotic perturbations might affect Chr loss and/or viability: maximal rounding in 2D culture is suppressed when cells are rigidly confined *in vitro* or surrounded *in vivo* by cells and matrix. Confinement is capable of killing cells.

confined mitosis of iPSCs and A549s (for multiple Chr's) proves quantitatively higher than 2D (Fig.4.4 C,D), and losses correlate with observed levels of abnormal mitosis (Fig.4.4 A,B). Loss of any one of the Chr reporters is far below abnormal mitosis frequencies (by ~15-fold for iPSCs and ~60-fold for A549s) which is consistent with numerous Chr's being lost. Because A549s divide every ~24h, cells were Noc-synchronized before confinement

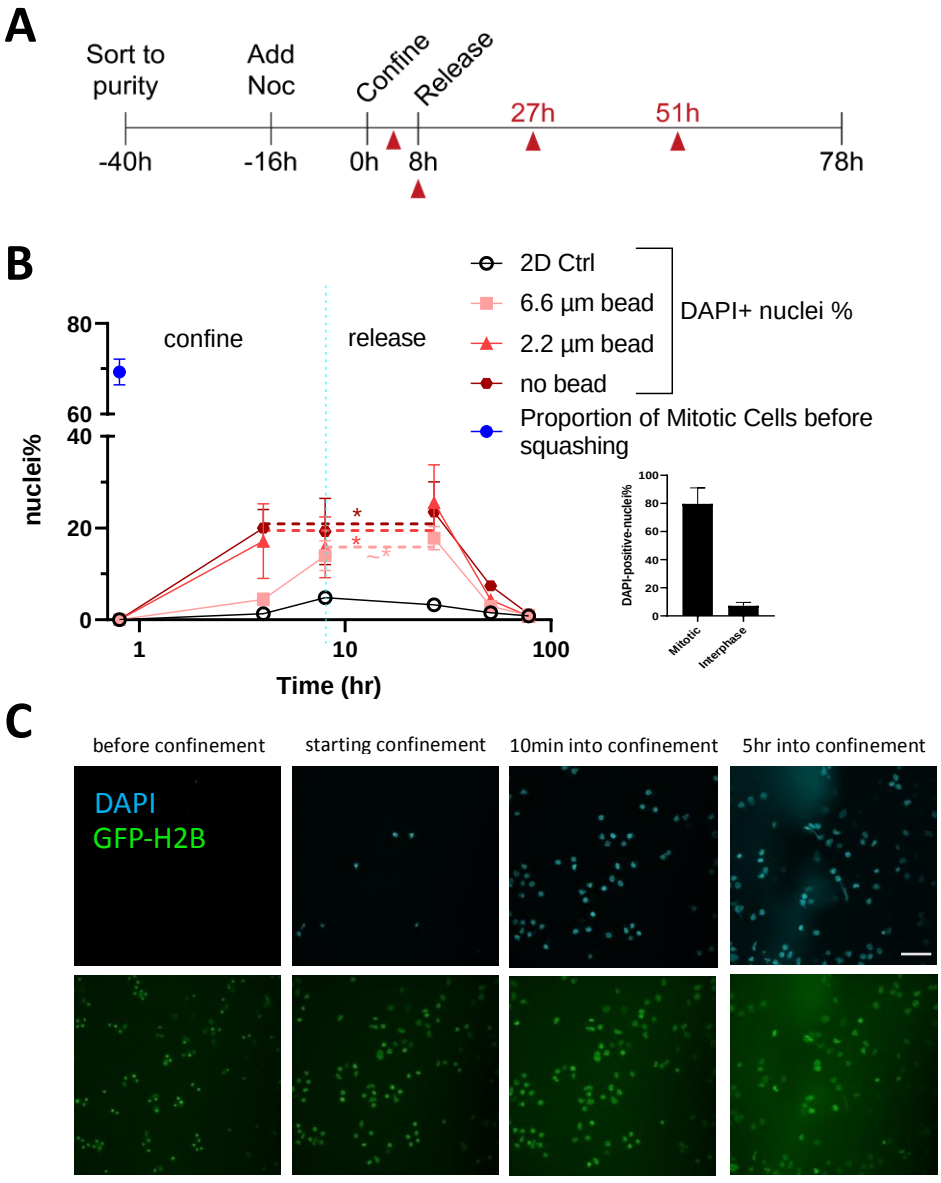

Figure 4.2: Confinement spacing optimization to minimize death. (A) Timeline of Confinement Application for cell death tracking. **(B)** Confinement with 6.58µm spacer beads requires longer time to cause mitotic cell death than with 2.16 µm spacer beads and without spacer, and the former doesn't cause as much death as the latter. So 6.58µm spacer is the primary choice of spacers for our assays. Majority of cells start as mitotic after nocodazole-induced synchronization. **(C)** Confinement without spacer beads leads to large scale of mitotic cell death within 10 minutes. $*p < 0.05$, $\sim*p = 0.05$. Scale bar = 100 µm.

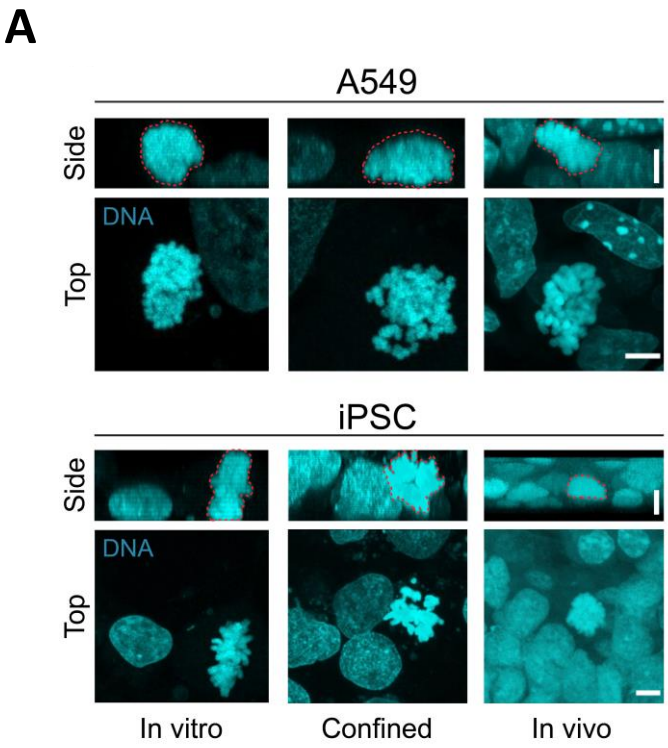

Figure 4.3: Mitotic nuclei *in vivo* or under confinement exhibit lower height than *in vitro* control.

(A) Images of chromatin and plots of chromatin height in iPSCs and A549 cells in either standard 2D culture, rigidly confined culture, or 3D *in vivo* teratomas or tumors engrafted at subcutaneous sites in immunodeficient mice. All scale bars = 5 μm.

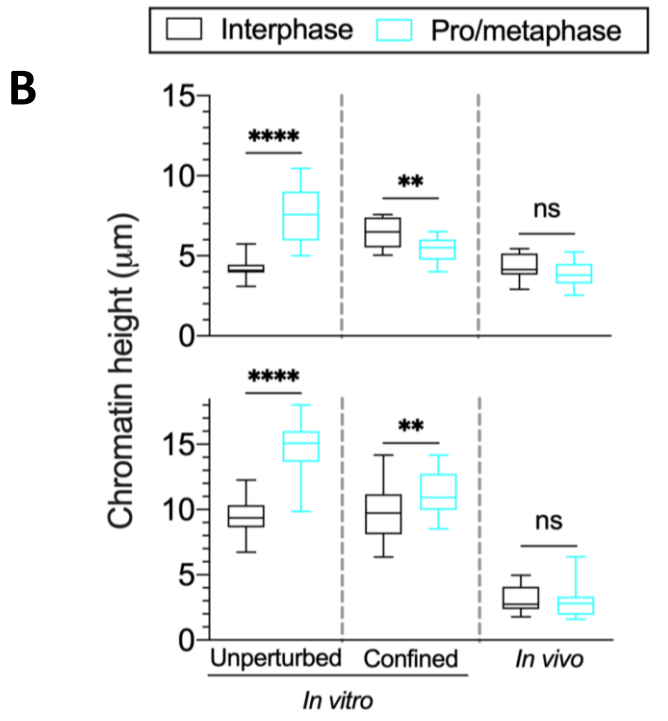

(B) Comparison among mitotic and interphase chromatin height in standard 2D, rigidly confined culture, or 3D *in vivo* teratoma/tumors. Mean and SEM (n = 3 replicates; Mann-Whitney U-rank test: $**p < 0.005$; $****p < 0.0001$; ns, not significant.

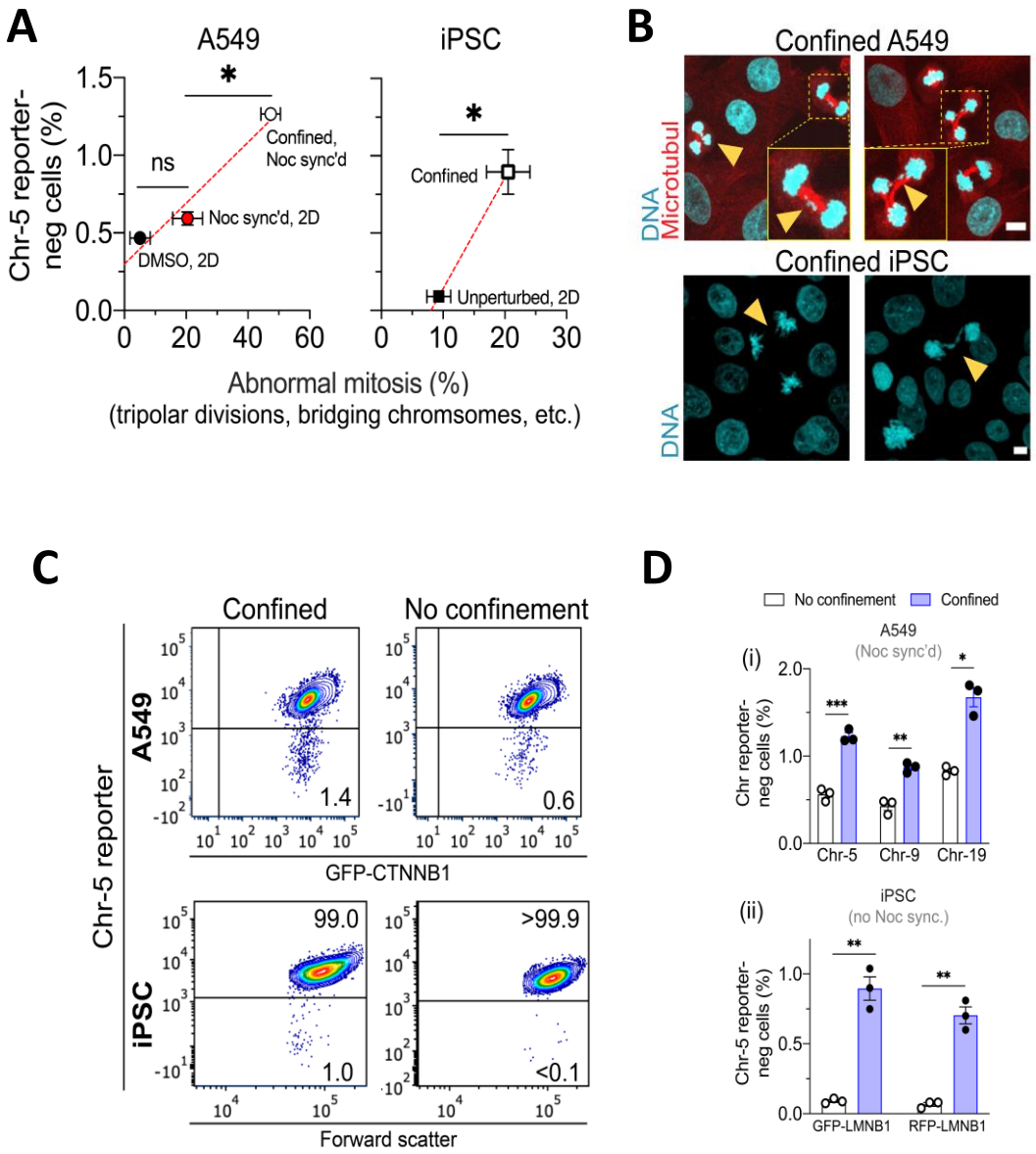

Figure 4.4: Confinement leads to increase in mitotic abnormality and more reporter-neg cells. (A) Flow cytometry measures of the percentage of Chr-5 reporter-neg cells plotted against percentage of abnormal mitosis for A549s and iPSCs. **(B)** Images of abnormal mitosis of A549 and iPSCs. Scale bar = 5 μm. **(C)–(D)** Flow cytometry analyses of Chr-5 reporter loss in iPSCs and A549s in either confined or standard 2D cultures; **(D)** *(i)* Noc-synchronized A549 cells with three different reporters, or *(ii)* two distinct iPSC clones (but no synchronization because iPSCs double in ~10h, which is faster than A549s). (Continued next page)

Figure 4.4: (Previous page) (A) & (D): n = 3 replicates; unpaired two-tailed t-test with Welch's correction: $*p < 0.05$, $**p < 0.005$, $***p < 0.0005$, ns, not significant.

A: with/Brandon Hayes, replicated by Mai Wang C: with Brandon Hayes D: with Brandon Hayes and Junhong Du

in some studies – with small residual effects fitting the trend. Synchronization of iPSCs was unnecessary because these cells double in ~10h, and while microscopy detection of abnormal mitosis is useful, it does not predict Chr loss: some iPSCs show abnormal mitosis without Chr reporter loss, but A549s show the opposite.

4.3 Chromosome loss in cells generated from confined mitosis and MPS1 inhibition are viable and heritable

Formation of colonies and maintenance of proportion of reporter-neg cells within the bulk population, which is higher in perturbed condition than basal level, both provide evidence for viability and heritability (Fig.4.7 C). A549s in 2D culture show basal levels of reporter-neg cells and colonies for the various Chr Reporters even after 2-3 wks, and 9-

4. Mitosis under confinement leads to viable and heritable descendants, results from mechanically triggered MT mis-attachment, and is protected by Myosin II

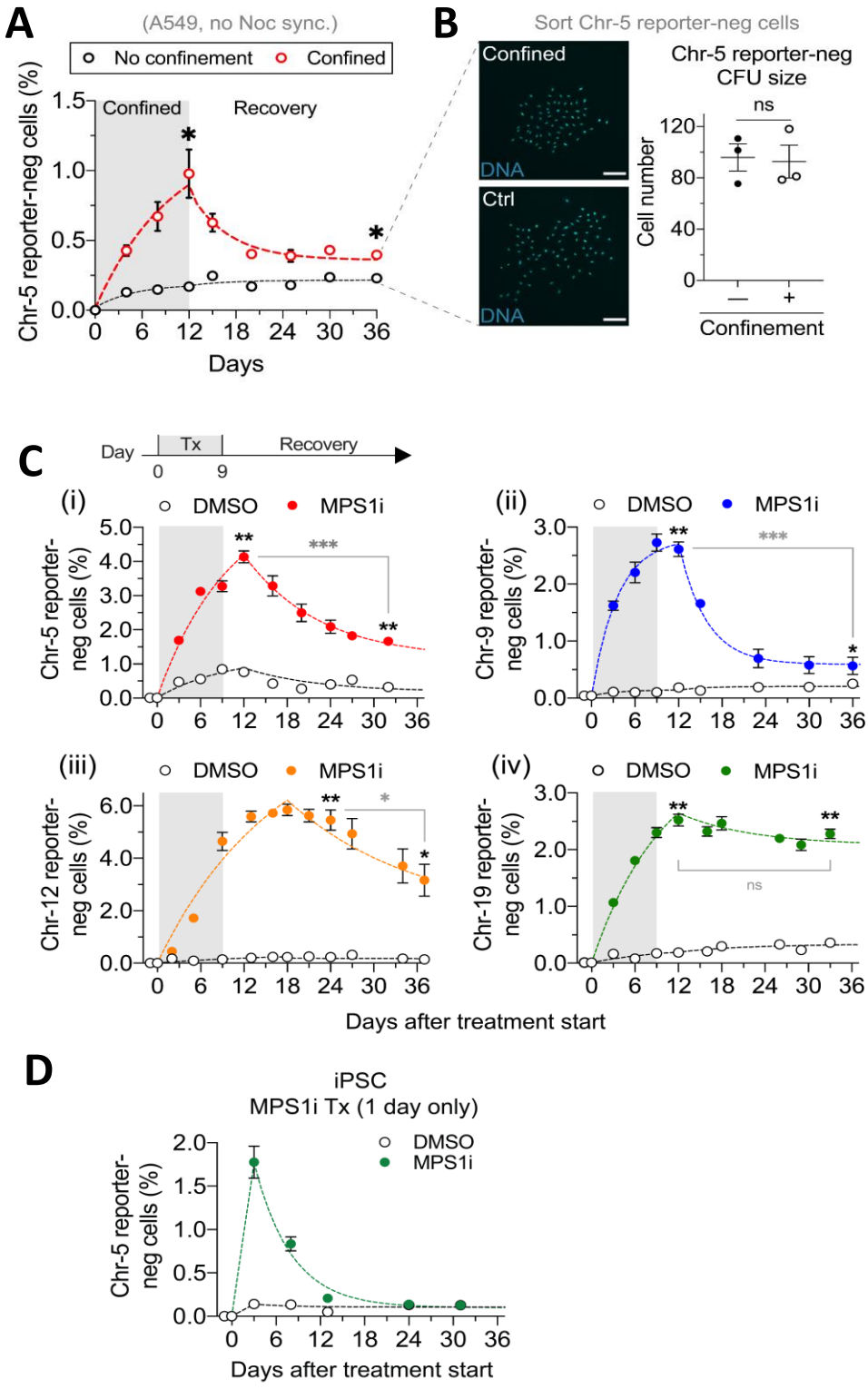

Figure 4.5: (Previous page) **Mathematical model shows confinement and MPS1i lead to reporter-neg population surviving in long-term after perturbation withdrawal in A549 but not iPSC.** Chr-5 reporter-negative kinetics for A549s after repeated cycles of rigid confinement for 12 days and recovery in 2D culture **(A)**, or MPSi treatment and recovery of A549s with multiple reporters **(C)** or iPSCs **(D)**. For the former, after 36 days, flow-sorted RFP-neg cells were plated back sparsely at 1:1 mixture with RFP-pos cells **(B)**; RFP-neg cell numbers in CFUs after 1 week are the same, and the mixture also showed the same total cell numbers for all RFP-pos and -neg sample conditions. (A)-(D): n = 3 replicates; unpaired two-tailed t-test with Welch's correction between each treatment condition at the same timepoint: $*p < 0.05$, $**p < 0.005$, $***p < 0.0005$, ns, not significant. Scale bar = 100 μm.

MPS1i-treated experimental result from Brandon Hayes

days of MPS1i not only tends to increase reporter loss and colony counts but drug withdrawal also leads to variable levels of viable cells with sustained loss of all Chr reporters (Fig.4.5 C). Likewise, for compression-generated reporter-negative A549s, once the confinement cycles are stopped, a decay to a stable fraction of reporter-negative cells greater than the controls is again observed (Fig.4.5 A). To again address possible concerns over selection and expansion versus *de novo* genetic change, we sorted RFP-neg and RFP-pos cells from confinement or control conditions, mixed 1:1 the neg: pos cells for either condition, and cultured in 2D for 1 week. The same total number of RFP-neg cells and RFP-pos cells were obtained from all conditions, with heritable loss of reporter evident in equally large and viable colonies (Fig. 4.5 B). The results are not only consistent with *de novo* genetic change but also with a similarity in mechanism between MT-disrupting MPS1i and mitotic compression. Viable interphase A549s after confinement re-spread

4. Mitosis under confinement leads to viable and heritable descendants, results from mechanically triggered MT mis-attachment, and is protected by Myosin II

A

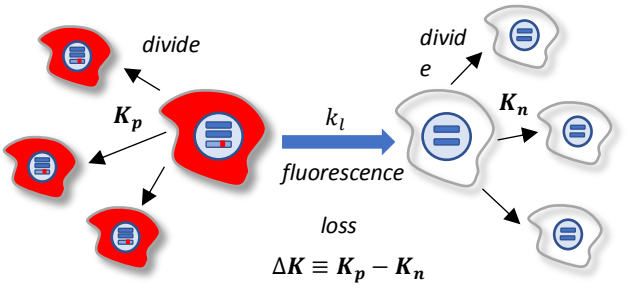

$$r(t) = 1 - \frac{1}{1+\frac{k_l}{\Delta K - k_l}+\left(\frac{r_0}{1-r_0}-\frac{k_l}{\Delta K - k_l}\right)Exp[-(\Delta K - k_l)t]},$$

$$r_0 = r(0)$$

B

Fitted parameters: $\frac{\Delta K}{K_{P,\,Ctrl}}$ $\quad K_{P,\,DMSO} = 0.86\ day^{-1}, K_{P,\,unconfined} = 0.42\ day^{-1}$ $\quad$ Fitted parameters: $\frac{k_l}{K_{p,\,Ctrl}} \times 10^3$

	Confine	Reversine			
	Chr-5	Chr-5	Chr-9	Chr-12	Chr-19
Ctrl-treat	0.47	0.12	0.32	0.07	0.12
Ctrl-release	0.24	0.12	0.33	0.07	0.12
Perturb-treat	0.47	0.12	0.32	0.07	0.12
Perturb-release	0.47	0.12	0.32	0.07	0.12

Confine	Reversine			
Chr-5	Chr-5	Chr-9	Chr-12	Chr-19
0.90	1.52	0.46	0.26	0.33
1.01	0.21	0.64	0.12	0.40
3.06	7.12	9.10	6.77	4.44
1.87	1.40	1.87	1.17	2.45

C

$$r(t) = \begin{cases} 1 - \dfrac{1}{1 + \dfrac{k_{l_{treat}}}{\Delta K_{treat} - k_{l_{treat}}} + \left(\dfrac{r_0}{1-r_0} - \dfrac{k_{l_{treat}}}{\Delta K_{treat} - k_{l_{treat}}}\right) Exp[-(\Delta K_{treat} - k_{l_{treat}})t]}, & t \le u \\ 1 - \dfrac{1}{1 + \dfrac{k_{l_{release}}}{\Delta K_{release} - k_{l_{release}}} + \left(\dfrac{r(u)}{1-r(u)} - \dfrac{k_{l_{release}}}{\Delta K_{release} - k_{l_{release}}}\right) Exp[-(\Delta K_{release} - k_{l_{release}})(t-u)]}, & t > u \end{cases}$$

$u = 12\ days$ for Chr-5, 9, and 19; $u = 18\ days$ for Chr-12.

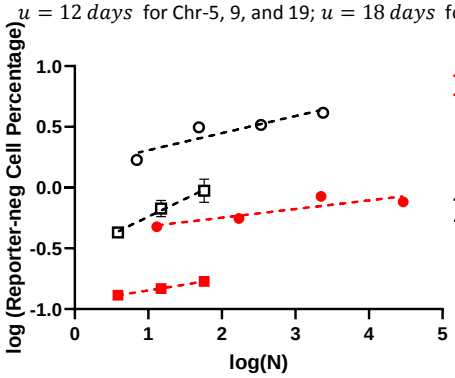

		slope(power exponent)	R^2
Chr-5 Unconfined		0.099	0.99
Chr-5	DMSO	0.071	0.78
Chr-9	DMSO	0.059	0.51
Chr-12	DMSO	0.033	0.17
Chr-19	DMSO	0.043	0.15
Chr-5 Confined		0.29	0.99
Chr-5	Reversine	0.14	0.85
Chr-9	Reversine	0.085	0.81
Chr-12	Reversine	0.35	0.87
Chr-19	Reversine	0.15	0.89

Figure 4.6: (Previous page) **Modeling and scaling of MPS1i and confinement generating stable reporter-neg populations. (A)** Schematic Diagram of the model of chromosome loss indicated by fluorescence loss. Cell division and fluorescence loss are both proportional to cell density, with K_p, K_n, k_l being net proliferation coefficient of positive cells, net proliferation coefficient of negative cells, and fluorescence-loss coefficient, respectively. The Fluorescence-null cell proportion model is then derived to be a function of $r\ (t)$. What's shown in figure 2 is $100\ r\ (t)$, as is expressed as percentage. Derivation of the model is shown in supplementary material D1. **(B)** Data fitting parameters are listed, as normalized to the fixed value $K_{p,\ DMSO}$, corresponding to fitting curves in Fig. 4.5. For each reporter, $k_{l,\ Rv,treat} >> k_{l,\ DMSO,treat}$, consistent with the fact that MPS1 inhibition leads to increased chromosome loss.

Fitting is based on the following assumptions:

Because protein degradation doesn't happen immediately after chromosome loss, the effect of MPS1 inhibitor reversine as to pos-to-neg conversion is delayed until day 12 for Chr-5, 9, 19, and day 18 for Chr-12, while the drug is actually released at day 9.

For each reporter, k_l for each phase is not necessarily the same, but ΔK is identical for all the phases except for reversine-treat phase.

(C) Treatment phase of all reporters as well as Chr-5 reporter under confinement scale with numers of divisions with power-law. In the plot, Chr-5 treated with DMSO/Reversine and with/without confinement are displayed. Other reporters are not displayed in the plot but scaled power law exponents (slope in log-scale) are presented. The perturbed processes have steeper slope than its corresponding control, with a fold change ranging from 1.5 to 10.

their decondensed chromatin after exiting mitosis, re-assemble their lamina, and proliferate normally (Fig. D2).

All of the data fit a three-parameter kinetic model that accounts for rates of reporter loss and net proliferation with or without loss (Fig.4.5 A,C, D, 4.6). All fits indicate slower net proliferation with loss; Chr-5 is lost ~4-fold faster from cells treated with MPS1i or by confinement, relative to controls. We also fit reporter loss with power laws versus N. For 2D Ctrl cultures (where $E = 0$ for an overlying fluid phase), Chr-5 reporter loss $\Delta \sim N^a$ with

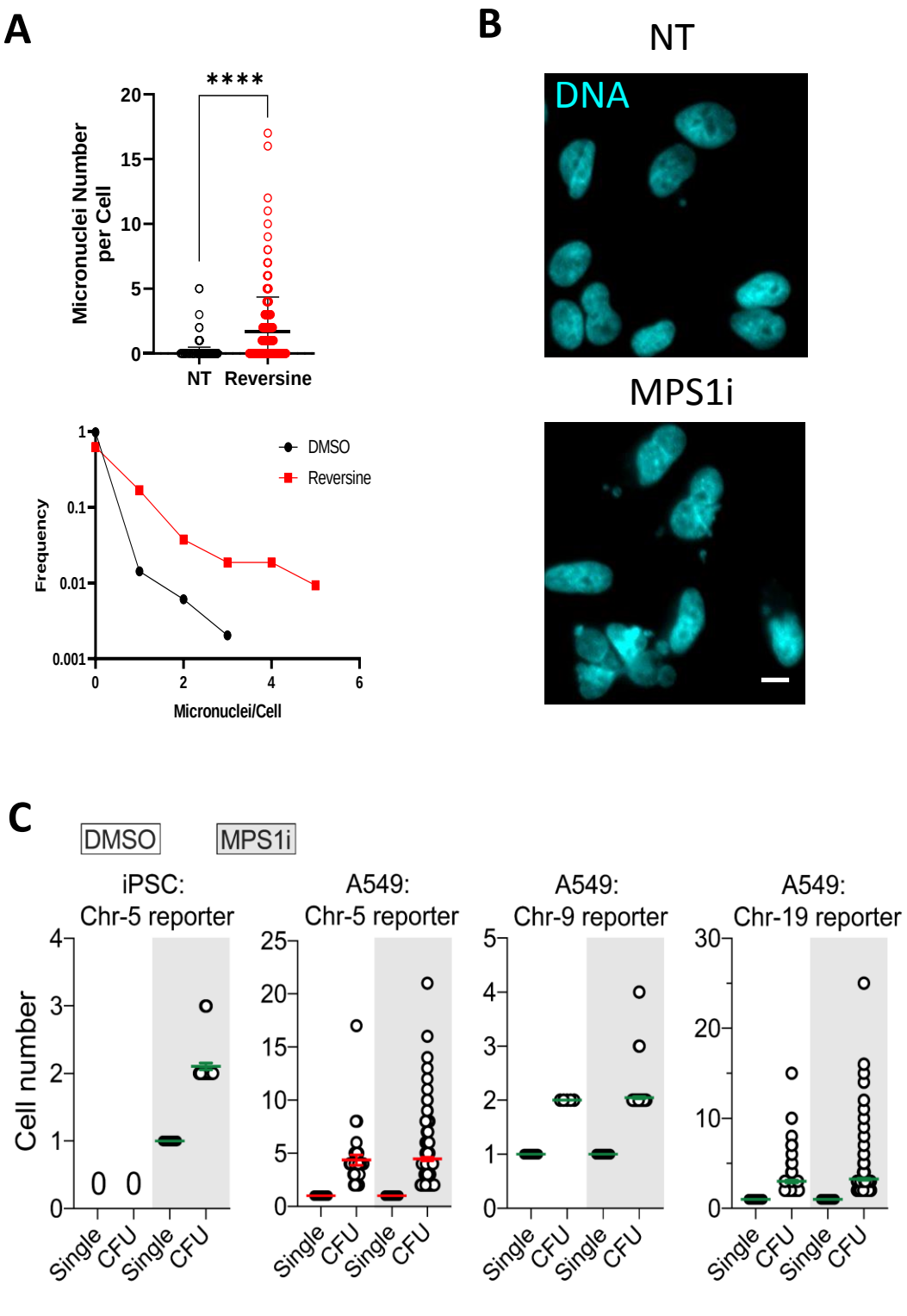
A
****
Micronuclei Number per Cell
20
15
10
5
0
NT
Reversine
DMSO
Reversine
Frequency
1
0.1
0.01
0.001
0
2
4
6
Micronuclei/Cell
B
NT
DNA
MPS1i
C
DMSO
MPS1i
iPSC: Chr-5 reporter
A549: Chr-5 reporter
A549: Chr-9 reporter
A549: Chr-19 reporter
Cell number
0 0
Single
CFU
Single
CFU

Figure 4.7: (Previous page) **MPS1i leads to viable reporter-neg colonies and more micronuclei. (A)** MPS1 inhibitor reversine-treated cells have more micronuclei, and have a broader distribution of cells with more than 1 micronuclei, compared with non-treated vehicle control. (n >200 cells per condition; unpaired two-tailed t-test with Welch's correction. ****$p < 0.0001$. Scale bar = 10 μm. **(B)** Images of cells with more micronuclei after MPS1 inhibition. **(C)** Cell numbers in reporter-negative colony forming units (CFUs) of iPSCs (with Chr-5 reporter) or A549s (with Chr-5, Chr-9, or Chr-19 reporters) when treated with a continuous low-dose reversine or control for 3-5 days.

C. with Brandon Hayes and Junhong Du

$a \sim 0.03$ to 0.1 (i.e. weak scaling), whereas for rigid confinement ($E >> 0$) and for MPS1i perturbations, $\Delta \sim N^b$ with $b/a \sim 2.5$. Power law analyses and kinetic model fits consistently show Chr-5 loss is stress-driven by several-fold but also varies much more (~2 to 10-fold) for other Chr's (Fig.4.6 C). After induced loss, growth or viability in 2D also shows Chr- and cell-type specific differences.

Micronuclei are also evident especially in perturbed cells, and are well-known to harbor mis-segregated Chr's that accumulate massive DNA damage, especially when lamin-B levels are low (Liu et al., 2018; Hatch et al., 2013; Fig 4.7 A). Micronuclei in perturbed cells show even more DNA damage (Fig D3). Confinement favors Chr mis-segregation during abnormal mitosis (Fig.4.4 A), with A549s showing many micronuclei post-confinement. However, micronuclei are comparatively rare in iPSCs, which could relate to near-zero tolerance of iPSCs and colonies to Chr loss in 2D-culture without MPS1i (Fig.4.7 B, C). Indeed, MPS1i-driven Chr loss in iPSCs almost vanishes after drug

withdrawal (Fig.4.5 D), even when using low doses and times that maintain viability of these normal cells.

4.4 Mitosis under confinement doesn't superimpose with MPS1 inhibition in leading to viable chromosome-loss descendants

Standard, well-established perturbations that cause losses and gains of Chr's in cultured cells include chemical inhibitors of microtubule (MT)-related pathways, such as drugs targeting the MPS1 kinase that coordinates attachment of MTs to chromosomes in the mitotic spindle (Dumont and Mitchison, 2009; Lancaster et al., 2013). Physical confinement of mitotic cells leads to increase in cell and nuclear area, and, therefore, makes it more difficult for microtubule to attach to kinetochore due to the relatively shorter length of MTs emitted from centromere to kinetochore (Dumont and Mitchison, 2009; Lancaster et al., 2013; Fig 4.8 D, E, D2).

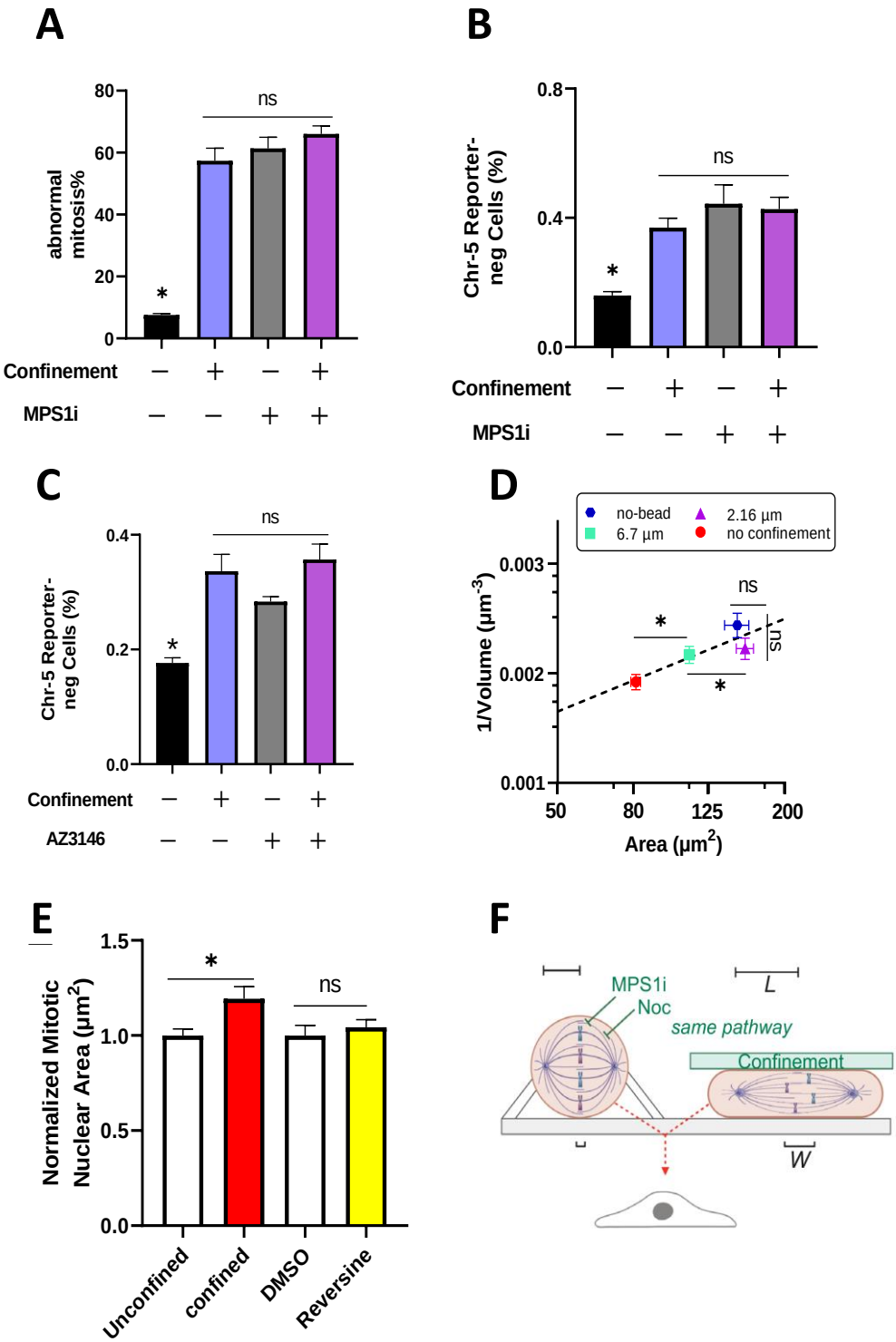
A
abnormal mitosis%
80
60
40
20
0
ns
*
Confinement
MPS1i
B
Chr-5 Reporter-neg Cells (%)
0.8
0.4
0.0
ns
*
Confinement
MPS1i
C
Chr-5 Reporter-neg Cells (%)
0.4
0.2
0.0
ns
*
Confinement
AZ3146
D
no-bead
6.7 µm
2.16 µm
no confinement
1/Volume (µm-3)
0.003
0.002
0.001
ns
*
ns
*
50
80
125
200
Area (µm2)
E
Normalized Mitotic Nuclear Area (µm2)
1.5
1.0
0.5
0.0
*
ns
Unconfined
confined
DMSO
Reversine
F
MPS1i
Noc
same pathway
L
Confinement
W

Figure 4.8: (Previous page) **Confinement and MPS1i lead to chromosome mis-segregation both through the Microtubule-dependent pathway and show no additive effect. (A)** Abnormal Mitosis% in dividing cells with MPS1i reversine, confinement, or combination. **(B)** Confinement and MPS1 inhibitory drug reversine combined perturbation and flow cytometry measures of Chr-5 reporter-negative A549 cells. Sub-saturating dose of MPS1i (reversine), confinement, or combination for 4 days. **(C)** Another MPS inhibitory drug AZ3146 with the optimal dose (one that gives similar RFP-neg% as confinement) was applied, instead of reversine, to give flow cytometry measures of AZ3146 only, confinement only, or combination for 4 days. **(D)** Inverse of volume (proportional to density) of mitotic chromatin is plotted against its projected area, with different heights of spacers applied. Enhanced confinement effect gives increased area and denser compactness. $n \geq 30$ cells per condition. **(E)** MPS1 inhibition (with reversine) doesn't enhance mitotic nuclear area of A549 cells, in contrast to confinement. $n \geq 45$ cells. **(F)** Pathway and colony formation schematic for MPS1i, nocodazole, and rigid confinement that all cause chromosome loss. Confinement increases spindle length L_{MT} and $W_{chromatin}$. Statistics: (A)-(C): n=3 replicates; two-way ANOVA for multiple comparisons. $*p < 0.05$; ns, not significant. (D), (E): Mann-Whitney U-rank test: $*p < 0.05$; ns, not significant.

Two different MPS1 inhibitors at sub-saturating dose generating similar reporter-neg% as confinement, respectively, do not show superimposed effect when applied simultaneously with confinement, and no more increase in abnormal mitosis was observed in the perturbation that combined MPS1i reversine and confinement compared with each one applied individually (Fig. 4.8 A, B, &C). This further conveys that confinement and MPS1 inhibition both cause abnormal mitosis with perturbing MT attachment onto kinetochore. MPS1i, however, doesn't increase mitotic area, indicating it deregulates MT attachment to kinetochore not through physically elongating the distance between centrosome and kinetochore, but perturbing such attachment through biochemically interfered SAC pathways. Moreover, nocodazole, as a microtubule disrupter, when treated at sub-saturating dose, doesn't show additive effect when combined with MPS1i as well, once

again confirming that MPS1i leads to mis-segregation through MT-dependent pathway (Fig. D2). Overall, MPS1i, confinement, and nocodazole all lead to chromosome mis-segregation through MT-mis-attachment, but as a result of chemically triggered mis-attachment, physically triggered, and not enough microtubules (Fig. 4.8 F).

4.5 Chromosome loss is favored by TOP2A-driven compaction but opposed by Myosin-II

To assess possible pathways of confinement-induced changes in viable cells that lost a chromosome, single-cell RNA-seq was applied after confinement of cells. RFP-neg cells show down-regulation of Chr-5 transcripts, consistent with gene-dosage effects (Fig.4.9A). These confined cells that clearly possess a genetic change are compared to spontaneously generated RFP-neg cells and show increased expression of multiple MTs and spindle factors (Fig.4.9A). These include the anti-apoptotic factor survivin (*BIRC5*) (Li et al., 2019; Castedo et al., 2004), which suggests that mitotic cells under rigid confinement must possess robust MT-spindle connections in order for even a fraction of stressed cells to survive. Topoisomerase-IIα (coded by *TOP2A gene*) was the most

upregulated and acts to compactify mitotic chromosomes in G2/M phase (Samejima et al., 2012; Farr et al., 2014). Vertical confinement spreads the chromatin (Fig.4.8 D,E,D2) as well as the cell and its mitotic spindle (Dumont and Mitchison, 2009), thus working against chromatin compaction and potentially requiring more TOP2A for at least some cells to maintain viability with a heritable loss. Indeed, RFP-neg cells and colonies have lost Chr-5 but gain the most anti-TOP2A signal when such cells are generated by confinement (Fig.4.9 B).

To assay TOP2A function in confined mitosis, a low, non-toxic dose of the TOP2A-specific inhibitor etoposide (Etop) was added to confined A549s after sorting and synchronizing cells, with unbound drug washed out after the 8h confinement. RFP-neg cells in 2D + Etop conditions are rare and show extremely low TOP2A (Fig.4.9 C, D). Confinement + Etop maintains the same high TOP2A and shows significantly more RFP-neg cells than 2D + Etop, albeit far below the normal level imposed by confinement without drug (Fig.4.9 C).

Distortion of mitotic chromatin within a compressed cell is opposed not by the nuclear lamina but by the acto-myosin cortex that contributes to stiffness (Stewart et al., 2011; Sedzinski et al., 2011). To test the role of myosin-II in protecting genetic integrity,

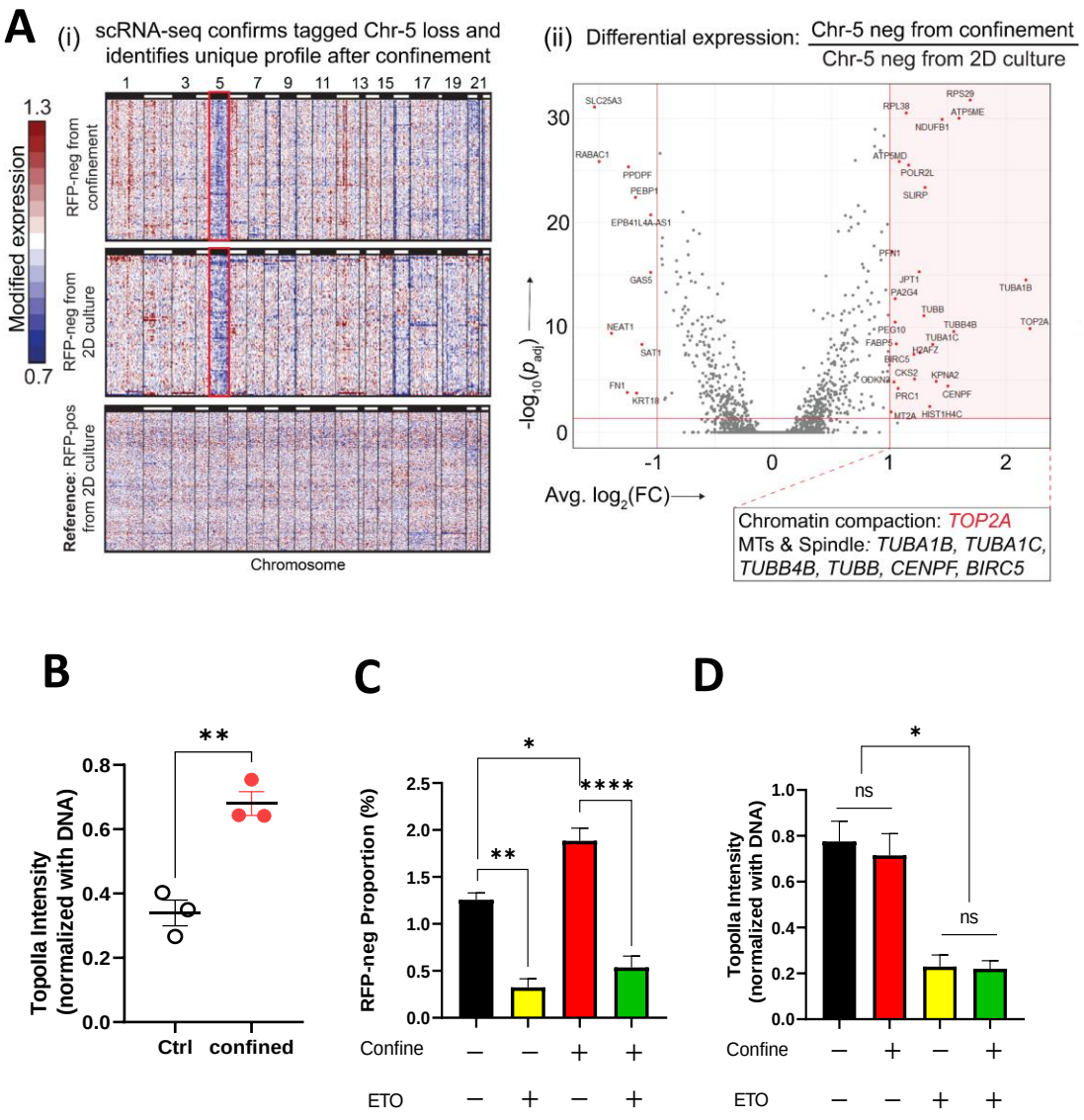

Figure 4.9: Single-cell RNA sequencing shows compression-induced Chr loss associates with chromatin-compacting Topoisomerase-IIa. (A) ***(i)*** Chr-5 loss inferred from single-cell RNA-seq of ChReporter-neg, Noc-synchronized A549s after either confinement for 8h (143 cells) or 2D culture for 8h (87 cells), plus 48h recovery. ChReporter-pos cells from 2D culture were used as a reference (163 cells). ***(ii)*** Differentially expressed genes in Chr-5 ChReporter-neg A549s generated either from confinement or spontaneously in 2D culture. (Continued next page)

Figure 4.9: (Previous page) *TOP2A* is the most upregulated gene in confined cells, with other upregulated genes being microtubule and other mitotic genes. **(B)** Reporter-neg cells after confinement shows significantly more Topoisomerase IIa intensity based on immunofluorescence. Two-tailed t-test with Welch's correction. **(C)** Top2A inhibitor Etoposide leads to decrease in reporter-neg% regardless of confinement, but confinement still increases reporter-neg% when Etoposide exists. Two-way ANOVA for multiple comparisons. **(D)** Etoposide, as an inhibitor, decreases TopoIIa signal by more than 2 folds. Two-way ANOVA for multiple comparisons. (B)-(D): n=3 replicates. *$p < 0.05$; **$p < 0.005$, ***$p < 0.0005$, ****$p < 0.0001$, ns, not significant.

A: sequencing: Mai Wang

knockdown of the major non-muscle myosin-II isoform, myosin-IIA *(*coded by *MYH9* gene), was done in rapidly dividing iPSCs with the Chr-5 reporter system (Fig.4.10 C). Similar knockdown with shRNA in embryonic mouse skin by Fuchs & coworkers led to carcinoma (Schramek et al., 2014), suggesting myosin-IIA has a tumor suppressor role as described also by others (Picariello et al., 2019). Evidence of genetic changes (as required for cancer) has remained unclear as has relevance to human cells, but skin is a relatively stiff and 3D microenvironment (Martincorena et al., 2015).

Compression of myosin-IIA knockdown cells not only increases visibly abnormal mitosis (Fig. D5) but also increases the percentage of RFP-neg cells versus controls (Fig.4.10 D). Importantly, the same increase is seen with myosin-II inhibitor blebbistatin added only during the 8h confinement, with such a brief drug treatment affecting the levels of very few proteins compared to knockdown (Raab et al., 2012). Neither blebbistatin nor

knockdown enhance the basal instability for percentage of RFP-neg cells in 2D cultures. Although myosin-IIA depletion can increase proliferation of some cancer cell types in 2D (Picariello et al., 2019) and 3D (Han et al., 2020), it has the opposite effect on normal stem cells in mechanically stressed skin (Aragona et al., 2020), and we find knockdown slows A549 proliferation only slightly and that mitosis in confinement is delayed but not stopped. To provide an additional test of the effects of abnormal mitosis versus proliferation rate, A549 cells were plated on a dense collagen-coated substrate that can severely limit spreading of some cell types (Engler et al., 2004) and indeed increases abnormal mitosis while *slowing* proliferation (Fig. D5). Myosin-IIA knockdown and shCtrl A549s show equal increases in the percentage of RFP-neg cells relative to standard 2D cultures, which again indicates that microenvironment-regulated abnormal mitosis better predicts chromosome loss than does the simple number of divisions *N* (Fig. 4.10 A, D5).

To better model division in dense 3D collagenous tissues (e.g. dermis; Schramek, et al., 2014;), A549s on the collagen-coated substrates were compressed. Only knockdown cells showed an increase in RFP-neg cell %, which suggests that myosin-IIA mechano-protects a cell's genetic integrity in microenvironments that are highly constraining laterally as well as vertically (Fig.4.10 A, B, D6). Hence, the general finding that shMYH9 and transient blebbistatin *do add* to confinement-induced instability differs again from transient MPS1i but aligns well with blebbistatin *not* disrupting MT-driven mitosis in

standard 2D culture (Straight et al., 2003), unlike MPS1i and Noc (Fig.4.8). Earlier observations that myosin-IIA has a tumor suppressor role in that its knockdown can lead to cancer in a relatively stiff tissue such as skin (Schramek, et al., 2014) might thus be explained by actomyosin protecting against chromosome loss in constraining 3D microenvironments.

4.6 Discussion

The hypothesis that mitosis within rigidly-constraining 3D microenvironments causes *heritable mechanogenetic* changes is supported by the mono-allelic chromosome reporter approach that directly reveals stress-driven, stiffness-associated generation of rare GFP/RFP-negative cells (~1%) that are to varying extent viable *in vitro* with conditions simulating *in vivo*. Traditional and Next-generation Genetic methods all support the approach. Although such conclusions seem to be lacking from reports of single cell genetic analyses to date, various genetic changes across normal tissues and tumors do appear maximal at high tissue stiffness and high tissue proliferation, with the efficacy of cancer immunotherapy also showing the same trend and highlighting a broader significance.

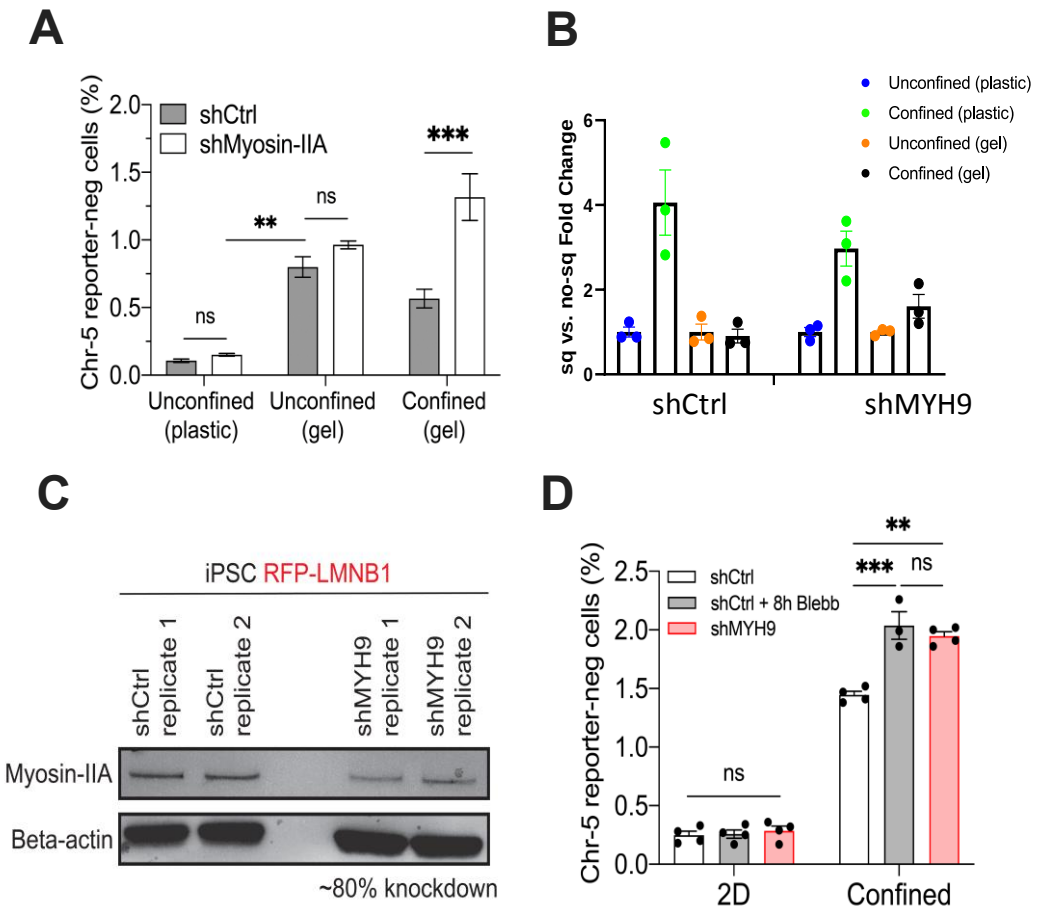

Figure 4.10: Myosin IIa protects against mitotic rounding and leads to more reporter-neg% once inhibited or knocked down. (A) RFP-neg cells occur more frequently on collagen-coated gels versus plastic, independent of Myosin-IIa knockdown, unless confined under a rigid coverslip. **(B)** Confinement applied on A549 shCtrl cells without doesn't lead to more RFP-neg%, while on A549 shMYH9 cells does more, albeit the fold change is still lower than on plastic. Data is normalized with respect to each unconfined counterpart. **(C)** Western blot shows successful 80% knockdown of Myosin Iia. **(D)** Flow cytometry analysis of iPSC Chr-5 reporter-negative cells with myosin-IIA knockdown or inhibition (with blebbistatin) under rigid confinement or not. Myosin-IIa knockdown and Inhibition both show increase in reporter-neg% with confinement compared to shCtrl. n = 4 replicates; 3-way ANOVA with Tukey's correction for multiple comparisons. *$p < 0.05$, **$p < 0.005$, ***$p < 0.0005$, ns, not significant.

A. Some data recruited from Brandon Hayes's experiment. C. shMYH9 Engineering: Brandon Hayes; D. confined: Brandon Hayes

A solid tissue such as normal lung (with high stiffness *E*) and its associated tumors shows low proliferation but more genetic change than a highly proliferative liquid tissue such as blood (*E*=0) and its associated hematopoietic cancers. Unsurprising is the fact that mechanical stress and 3D-rigidity can kill cells, and so the question becomes whether some stressed cells survive with changes as visibly tracked by the reporter approach. Assumptions of error-free division are clearly flawed and become unnecessary compared to standard approaches with "clonal expansion" and genetic analyses. Visible and sustained functional genetic changes can quickly result from 3D compression (Fig.4.4) that can distort the mitotic spindle and increase chromosome mis-segregation as is associated, for example, with altered tissue architecture (Dumont and Mitchison, 2009; Lancaster et al., 2013; Matthews et al., 2020; Knouse et al., 2018). The approach could further address whether viable changes to a cell's DNA also result from 2D matrix stiffness modulation of the lifetime of chromosome bridges (Umbreit et al., 2020).

Cytokinesis in rigid yeast *normally* requires myosin-II, with its deletion somehow causing viable chromosome losses and gains (Rancati et al., 2008), which suggested a genome protective role. Indeed, under the stresses of rigidity confined mitosis and distinct from standard 2D-culture, genetic integrity is regulated (positively) by MYH9 and (negatively) by TOP2A. MYH9 might directly regulate the "guardian of the genome" p53 and explain the presumed genetic changes that lead to cancer in MYH9 knockdown mouse skin but results for mouse tongue seem to differ (Schramek et al., 2014; Conti et al., 2015).

In standard 2D-cultures of a cardiomyocyte tumor line, nonmuscle myosin-II depletion increases abnormal mitosis and cell death as well as MT acetylation-stabilization (Ma et al., 2010), which has been linked to a phosphatase that inhibits both myosin-II contractility and a MT-targeting de-acetylase (Joo and Yamada, 2014) but also linked to aneuploidization in breast cancer (Sudo, 2018). Although increased Chr loss with MYH9 depletion in 3D-confinement is distinct from MT based processes and from processes in 2D (Fig.4.8 *vs* Fig.4.10), the reporter approach allows molecular mechanisms to be further addressed by specifically interrogating cells with clear, heritable loss of Chr's. Indeed, unbiased analyses of cells with heritable Chromosome loss after confined mitosis revealed TOP2A induction (Fig.4.9), and this could reflect mechanosensitive pathways based on ChIP-Seq showing serum response factor (SRF) binding to *TOP2A* as well as *MYH9* genes. The finding that TOP2A remains high for days or more after confinement (>1-2 cell cycles) is further consistent with a 'mechanical memory' such as that associated with proliferation-regulating transcriptional co-factor YAP1 (YES-associated protein-1) in cells grown on rigid but not soft substrates (Yang et al., 2014). Stretching of mouse skin also induces nuclear translocation of YAP1 and key SRF factors downstream of MYH9, with both pathways essential to DNA replication in epidermal stem cells (Aragona et al., 2020). Physically, lateral stretching tends to vertically compress cells via the Poisson effect, with direct roles on mitosis and specific factors such as TOP2A requiring further study - particularly while focused on viable, rare cells with a specific heritable genetic change.

DNA sequence certainly confers long-term biological memory, and so mechanogenetic changes to a cell's DNA likewise confer mechanical memory.

4.7 Materials and methods

Cell lines and tissue culture

A549 cells were cultured in Ham's F-12 media (Gibco 11765047) supplemented with 10% (v/v) fetal bovine serum (FBS; MilliporeSigma, Catalog no. F2442) and 100 U ml^{-1} penicillin-streptomycin (Gibco, Catalog no. 15140122). All cells were passaged every 2-3 days using 0.05% Trypsin/EDTA (Gibco, Catalog no. 25300054). All A549 cells were incubated at 37^{o}C and maintained at 5% CO_2.The original A549 RFP-LMNB1 cell line was engineered by Sigma-Aldrich. The A549 cell line was obtained from the American Type Culture Collection (ATCC).

The following induced pluripotent stem cell (iPSC) lines were also used, all of which were acquired from the Coriell Institute for Biomedical Research and generated/validated by the Allen Institute for Cell Science: iPSC GFP-LMNB1 (AICS-0013 cl.210), iPSC RFP-LMNB1 GFP-SEC61B (AICS-0059 cl.36), and iPSC FBL-GFP NPM1-RFP (AICS-0084

cl.18). iPSCs were cultured in mTseR Plus medium (STEMCELL Technologies, Catalog no. 05825), with mTser Plus 5X supplement and 100 U ml^{-1} penicillin-streptomycin. For passaging and maintenance of iPSCs, cells were lifted with accutase (Sigma, Catalog no. A6964) at 37^{o}C and re-plated into 10-cm plates (Corning) coated with Matrigel (Corning, Catalog no. 356231) following the Allen Institute of Cell Science's protocol. 10 mM ROCK inhibitor (Y-27632; STEMCELL Technologies, Catalog no. 72302) was added to replated cultures to help with adherence and to prevent differentiation. Passaging was done once iPSC cultures reached 70% confluency to prevent spontaneous differentiation. All iPSC lines were also cultured at 37^{o}C and maintained at 5% CO_2.

Single cell RNA-sequencing

RNA libraries were constructed using the Chromium Single Cell Gene Expression kit (v3.1, single index, Catalog no. PN-1000128; PN-1000127; PN-1000213) from 10X Genomics per the manufacturer's instructions. The libraries were submitted to the University of Pennsylvania's Next Generation Sequencing Core for sequencing using NovaSeq 6000 (100 cycles) from Illumina. Raw base call (BCL) files were analyzed using CellRanger (version 5.0.1) to generate FASTQ files and the "count" command was used to generate raw count matrices aligned to GRCh38 provided by 10x genomics. For teratoma samples, FASTQ files were aligned to both GRCh38 and GRCm38. The cells are labeled to be human/mouse cells if more than 90% of the UMIs are aligned to GRCh38/GRCm38.

The data generated was imported as a Seurat object (4.0.0) for future downstream analysis (2). Cells were filtered to make sure that they expressed 500 and 6,000 genes inclusive and had less than 10 percent mitochondrial content. Data was normalized using the "LogNormalize" method or sctransform package (0.3.2) (3). Differential expression analysis was performed using the "FindAllMarkers" command and the output was used for the volcano plot. The very first 30 dimensions were used to generate UMAP. Cell cycle analysis was performed using "CellCycleScoring" command.

Cell type annotations

Raw expression matrices were used as the input for the singleR (1.4.1) package (Aran et al., 2019). The cell types were annotated based on Human Primary Cell Atlas (Mabbott et al., 2013).

Monoallelic chromosome tagging

For all attempted monoallelic chromosome reporters as described in Fig. 1E, all donor constructs were a gift from Allen Institute of Cell Science: AICSDP-8:TOMM20-mEGFP (Addgene plasmid #87423; http://n2t.net/addgene:87423; RRID:Addgene_87423), AICSDP-13:FBL-mEGFP (Addgene plasmid #87427; http://n2t.net/addgene:87427; RRID:Addgene_87427), AICSDP-35:AAVS1-mEGFP (Addgene plasmid #91565;

http://n2t.net/addgene:91565; RRID:Addgene_91565), AICSDP-42:AAVS1-mTagRFPT-CAAX (Addgene plasmid #107580; http://n2t.net/addgene:107580; RRID:Addgene_107580), AICSDP-1:PXN-EGFP (Addgene plasmid #87420; http://n2t.net/addgene:87420; RRID:Addgene_87420), AICSDP-10:LMNB1-mEGFP (Addgene plasmid #87422; http://n2t.net/addgene:87422; RRID:Addgene_87422), AICSDP-52: HIST1H2BJ-mEGFP (Addgene plasmid #109121; http://n2t.net/addgene:109121 ; RRID:Addgene_109121), AICSDP-7:SEC61B-mEGFP (Addgene plasmid # 87426; http://n2t.net/addgene:87426; RRID:Addgene_87426).

All knock-in reporter lines were generated following the protocol established in (1) using CRISPR/Cas9 technology. Donor plasmids were designed such that unique designs for each target locus contain 5' and 3' homology arms (1 kb each) for the desired insertion site, based on the GRCh38 reference human genome. For editing, we use the ribonucleic protein (RNP) method with recombinant wild type *S. pyogenes* Cas9 protein pre-complexed with a synthetic CRISPR RNA (crRNA) and a trans-activating crRNA (tracrRNA) duplex. Recombinant wild-type Cas9 protein was purchased from the University of California–Berkeley QB3 Macrolab, while crRNA and tracrRNA oligonucleotides were designed by and purchased from Horizon Discovery. For transfection of donor templates into target cells, we used the electroporation using a Gene Pulser Xcell Electroporation System (Bio-Rad). 700,000 targets cells were lifted using 0.05% Trypsin/EDTA, resuspended in 200 ul of fresh media without penicillin-

streptomycin, and loaded into a 0.4-cm cuvette. 4 µL of both 10 µM crRNA:tracrRNA duplex and 10 µM recombinant Cas9 protein were added to the cell solution, as well as 8 µg of donor plasmid. Electroporation conditions were as follows: (1) A549 and H23: 200V with 45 ms pulse length using a square-wave protocol; (2) U2OS: 160V with 30 ms pulse length using a square-wave protocol. After electroporation, cells were allowed to expand for ~1 week and then enriched via fluorescence-activated cell sorting (FACS), as described below. 3-5 FACS enrichment cycles were performed to achieve a pure reporter-positive population.

Lentiviral packaging and delivery

MYH9 silencing was performed by lentiviral-driven expression of short-hairpin RNAs purchased from Sigma-Aldrich, using the pLKO backbone construct. The following shRNA were used: TRCN0000285480, TRCN0000029468, TRCN0000029466, TRCN0000276055, and TRCN0000276070. For non-targeting shRNA control, the pLKO-sh-HSC plasmid was a gift from Do-Hyung Kim (Addgene plasmid # 46896 ; http://n2t.net/addgene:46896 ; RRID:Addgene_46896). Lentivirus was produced in HEK293T cells using MirusBio TransIT-Lenti Transfection Reagent (Catalog no. MIR 6604) following the manufacturer's protocol. Lentiviral production was allowed to occur for 48h, after which the supernatant was collected. Lentivirus was concentrated and purified from traces of fetal bovine serum using the PEG-it Virus Precipitation Solution (System Biosciences, Catalog no. LV810A-1) following the manufacturer's protocol.

Infected cells were selected by incubation using 1 μg ml^{-1} puromycin (Corning, Catalog no. 61385RA).

Treatments

For all cancer cell treatments, either 300,000 cells were plated per well in a 6-well plate (Corning) or 60,000 cells per well in a 24-well plate (Corning). For iPSC treatments, 60,000 cells were plated per 6-well plate. The following chemical treatments were used: MPS1 inhibitor reversine (Cayman Chemical, Catalog no. 10004412), MPS1 inhibitor AZ3146 (Cayman Chemical, Catalog no. 19991), TOP2A inhibitor etoposide (Cayman Chemical, Catalog no. 12092), nocodazole (MilliporeSigma, Catalog no. M1404), blebbistatin (MilliporeSigma, Catalog no. 203389), GSK-3 inhibitor CHIR-99021 (MilliporeSigma, Catalog no. SML1046), and dimethyl sulfoxide (DMSO; Millipore Sigma, Catalog no. D2438). The reversine concentrations and treatment times used, unless otherwise stated, are: for A549, 0.1 μM for 72h; for U2OS and H23, 1.5 μM for 24h followed by washout and 48h recovery; for iPSCs, 0.25 μM for 24h followed by washout and 24-48h recovery. All AZ3146 treatments were done at 1.5 μM for 24h followed by washout and 48h recovery. Non-confinement etoposide studies were done at 1 μM for 24h followed by washout and 48h recovery. For APC complex antagonism, 5 μM CHIR-99021 was used. For myosin-IIA inhibition studies, blebbistatin was used at 20 μM for 24h followed by washout and 48h recovery or used at the same concentration for the entire of

a confinement session. For all cell-cycle synchronization, nocodazole was added to cells at a final concentration of 50 ng ml^{-1} for 12-18h. For reversine treatments paired with either nocodazole or confinement, ony 50 nM concentration was used.

Flow cytometry and FACS.

All flow cytometry was performed on a BD LSRII (Benton Dickinson) and analyzed with FCS Express 7 software (De Novo Software). All studied cell lines were detached by brief trypsinization (for all cancer lines in 2D culture) or with accutase (for iPSCs), washed, and resuspended in FACS buffer (PBS + 5% FBS) with 1.0 µg ml^{-1} DAPI (MilliporeSigma, Catalog no. 09542). For fluorescence-activated cells sorting, or FACS, cells were prepared in the same way as described above except that freshly prepared sterile FACS buffer was used and no DAPI was included. FACS was performed on either a BD FACS Aria II or a BD FACS Jazz. Prior to any assay that assessed reporter-negative subpopulation generation, cells were FACS-enriched for only reporter-positive cells.

For gating, forward scatter parameters FSC-A vs. FSC-H and side scatter parameters SSC-A vs. SSC-H were used to remove aggregates from analysis. Live cells were gated on using forward scatter and side scatter (FSC-A vs. SSC-A). DAPI was further used to discriminate between live cells and debris/dead cells.

Antibodies

Antibodies used in this study are as follows: anti-alpha/beta tubulin (Cell Signaling Technology, Catalog no. 2148S), anti-Myosin-IIA (Cell Signaling Technology, Catalog no. 3403S), anti-TopoIIalpha (Santa Cruz Biotechnology, Catalog no. sc-365916), anti-beta-actin (santa Cruz, Catalog no. sc-47778), and AlexaFluor 647 donkey anti-mouse IgG (H+L) secondary (Invitrogen, Catalog no. A31571), and AlexaFluor 647 donkey anti-rabbit IgG (H+L) secondary (Invitrogen, Catalog no. A31573). For Western blotting, ECL anti-mouse IgG horseradish peroxidase (HRP) linked whole antibody (Cytiva, Catalog no. NA931V) and ECL-anti-rabbit IgG HRP linked whole antibody (Cytiva, Catalog no. NA934V) were used.

Immunoblotting

Western blotting was performed using standard methods. In brief, cells were briefly trypsinized, washed 3x with cold PBS, and then lysed in RIPA buffer (150 mM NaCl, 1% NP-40 alternative, 0.5% sodium deoxycholate, 0.1% SDS, 40 mM Tris pH 8.0). RIPA buffer also contained 1X protease inhibitor cocktail (Millipore Sigma, Catalog no. P8340). After lysis, centrifugation was done to discard lipids and other contaminants. Samples were then boiled in 1X NuPage LDS sample buffer (Invitrogen, Catalog no. NP0007) with 2.5% v/v β-mercaptoethanol. Approximately 1.0×10^6 cells were used for each analysis.

Proteins were separated by electrophoresis on NuPAGE 4-12% Bis-Tris gels run with 1X MOPS buffer (Invitrogen, Catalog no. NP0323), or 3-8% Bis-Tris gels run with 1X Tris Acetate buffer (Invitrogen, Catalog No. LA0041; Myosin-IIA samples only) and transferred to an iBlot nitrocellulose membrane (Invitrogen, Catalog no. IB301002). The membranes were cut into strips corresponding to one lane loaded with lysate and one lane loaded with a molecular weight marker and then blocked with 5% nonfat milk in Tris buffered saline (TBS) plus Tween-20 (TBST) for 1h. The membranes were washed with TBST and incubated with 1:500 secondary antibody conjugated with horseradish peroxidase in 5% milk in TBST for 1 h at room temperature with agitation. The membranes were washed again with TBST, then TBS, and developed with a 3,3',5,5'-tetramethylbenzidine (TMB) substrate (Genscript L0022V or Sigma T0565). Developed membranes were scanned and analyzed with ImageJ (National Institutes of Health).

Immunofluorescence and imaging

Cells were fixed in 4% formaldehyde (Thermo Fisher Scientific, Catalog no. 28908) for 15 min, followed by permeabilization by 0.5% Triton-X (MilliporeSigma, Catalog no. 112298) for 15 min, and blocked with 5% bovine serum albumin (BSA; MilliporeSigma, Catalog no. A7906) for 30 min and overnight incubation in primary antibodies (1:500 dilution). The cells were then incubated in secondary antibodies (1:500 dilution) for 1.5h, and their nuclei were stained with 8μM Hoechst 33342 (Thermo Fisher, Catalog no. 62249) for 15 min. When mounting is involved, Prolong Gold antifade reagent was used

(Invitrogen, Catalog no. P36930). Micronucleated cells were classified manually by distinct staining by Hoescht 33342 of structures outside of the main nucleus. Epifluorescence imaging was performed using an Olympus IX71 with a digital camera (Photometrics) and a 40x/0.6 NA objective. For certain samples, confocal imaging was performed on a Leica TCS SP8 system with a 63x/1.4 NA oil-immersion. Live imaging was performed on an EVOS FL Auto Imaging System with 10× or 20x/0.6 NA object in normal culture conditions (37°C and 5% CO2; complete culture medium as specified above).

MPS1 inhibition kinetics and CFU studies

For MPS1i studies, A549 cells were originally plated at a density of 30,000 cells per 24-well after FACS enrichment for reporter-positive cells and then treated with 0.1 μM reversine continuously for 9 days. Cells were then allowed to recover for 3-4 weeks. Cells were passaged whenever they approached ~80% confluency (every ~3 days) and a sample of the passaged population was analyzed via flow cytometry. Whenever cells were passaged within the first 9 days, they were replated in fresh media with reversine.

For all colony-forming units (CFU) studies, A549 cells were continuously treated with 0.1 μM for 3-5 days to allow for generation of identifiable reporter-negative CFUs. Cells were plated at a low density (~20,000 cells per 6-well) to avoid passaging in the

allotted time frame. For iPSCs, cells were treated with reversine following the previously described treatment. CFUs were identified via microscopy using an Olympus IX inverted microscope with a 40x/0.6 NA or 20x/0.4 NA objective and equipped with a sCMOS camera (Photometrics Prime). Images were quantified using ImageJ software.

In vitro mechanical confinement assays

Prior to all mechanical confinement assays, A549 cells were FACS-enriched for reporter-positive cells only, as described in *Flow cytometry and FACS*. iPSCs did not have to be FACS-enriched, as these cultures usually maintained below a 0.1% reporter-negative population even after continuous culture for ~1 year, suggesting genomic stability. The night prior to assay, 30-mm glass coverslips were coated with RainX (glass water repellent PDMS; RainX Company, Catalog no. 1597562) and then left in PBS under ultraviolet light for sterilization overnight. For assay, A549 cells were plated at 300,000 cells per 6-well. Roughly 24h later after which cells had settled and adhered, they were treated with nocodazole at a concentration of 50 ng ml^{-1} to allow for synchronization. At the same time, 6.58-µm polystyrene beads (SpheroTech, Catalog no. SVP-60-5) were added at the same density as the cells during this time. These polystyrene beads served as spacers to control the height of mechanical confinement and would also adhere to the cell culture plastic after the synchronization time period. After 12-18 hours of nocodazole synchronization, cells were gently washed 5X with PBS and then replenished with 1.5 mL of fresh media. Then,

sterile, RainX (PDMS)-coated 30-mm glass coverslips were gently placed on top of the cells. A sterilized, stainless steel weight was then placed on top of the coverslip to complete confinement. The complete confinement setup (stainless steel weight with PDMS-coated glass coverslip) was removed after 8-10h, cells were gently washed with PBS, and fresh media was added to the recently confined cultures. Cells were allowed to grow for 2 days before brief trypsinization and flow cytometry quantification of the generation of reporter-negative cells. A subset of these cells were also plated back for repeated confinement cycles as necessary. Etoposide studies (Fig.2C) follows the synchronization protocol, and the drug was added only during confinement, and washed out afterwards.

All iPSC and non-nocodazole synchronized A549 confinement studies followed the same exact procedure as the original nocodazole-synchronized A549 experiment with the exception of nocodazole synchronization. iPSCs were plated at 600,000 cells per 6-well, while A549s were still plated at the original density. Roughly 2h before confinement, spent media was discarded and replaced with fresh media containing the 6.58-μm polystyrene spacer beads to allow beads to settle. Then, cells underwent the same exact mechanical confinement assay. iPSCs only underwent a single cycle (one ~8h confinement). Unsynchronized A549 cells underwent four sessions of 8h confinement for short-term studies or 12 sessions for long-term kinetics studies. These A549 cells were passaged as needed to avoid over-confluency.

The MPS1 inhibitors reversine and AZ3146, when applied simultaneously with confinement (Fig.2A-B), followed the schematic timeline outlined in (Fig. S3D). Drugs were gently washed out with PBS after confinement. Their corresponding dose testing experiments (Fig.S9D) were conducted with the same timeline, except that confinement was replaced with different doses of MPS1 inhibitory drugs.

Live-imaging of *in vitro* mechanical confinement

For live-imaging of mechanical confinement, A549 cells with monoallelic GFP-H2B cells or iPSCs with Hoescht 33342 staining were used and prepared accordingly as described previously. Images were taken while cells underwent confinement every 20 min using Olympus IX71 with a digital camera and a 20x/0.4 NA objective. For all confinement assays, an unconfined 2D control was maintained. The 2D control culture was plated at roughly a quarter of the density used for the confined cultures so that both samples could be passaged simultaneously later on. For abnormal mitosis analysis of MPS1i combined with confinement, samples were first synchronized. Then, MPS1i was added to the samples for the same duration as a confinement experiment (with or without actual confinement occurring). Measurements were taken at specified time points, but the locations were not strictly maintained.

To quantify cell death resulting from confinement, we used A549 cells with the Chr-5 RFP-LMNB1 reporter and a GFP-H2B tag for nuclear localization and viability assessment. Cells were synchronized with nocodazole as previously described, and after

nocodazole washout, fresh media with 1 µM DAPI was added. Cells were then incubated at 37^{o}C for ~5 min for DAPI to diffuse and penetrate. Well plates were marked with dots on bottom prior to assay, and images were taken to define the status of cells prior to confinement. Afterwards, confinement continued normally for ~8h as described previously, with images taken at distinct timepoints at the same marked locations. Spent media was discarded and replaced with fresh media with 1 µM DAPI again 27h for a ~10-min incubation after the assay initially began (and for all subsequent imaging timepoints) for live/dead discrimination. Images were taken again at marked locations. Media with DAPI was always discarded after imaging and replaced with fresh culture media.

Quantification of abnormal mitosis during confinement using confocal microscopy

Both A549 cells and iPSCs were plated at the same densities described in *In vitro mechanical confinement assays* on top of sterile 30-mm glass coverslips. For A549s, nocodazole synchronization was done as previously described. Polystyrene spacer beads were also added to cultures as previously described. On the day of assay, 1.5 mL of complete culture media per well was added to as many wells of an ultra-low attachment 6-well plate (Corning) as needed. The 30-mm glass coverslips with the cells adhered to them were then flipped upside down and transferred to the ultra-low attachment 6-well to create a "sandwich" in which the cells were between plastic and glass layers. A sterile stainless weight was then added to the top of the glass coverslip to begin confinement. After 1-2h

had elapsed, the weight was removed, and the glass coverslip with cells was flipped back to its original position (so cells were no longer sandwiched) and transferred to a clean 6-well plate for fixation using 4% paraformaldehyde. Confocal imaging was performed on a Leica TCS SP8 system with a 63x/1.4 NA oil-immersion.

Image acquisition for measurement of chromatin height during confinement

For unconfined measurements of chromatin, both A549 cells and iPSCs were plated at the same densities described in *In vitro mechanical confinement assays* on top of sterile 35-mm glass bottom petri dishes (MaTek, Catalog no. p35G-1.5-14-C). For A549s, nocodazole synchronization was done as previously described. After nocodazole release, cells were stained with 8 μM Hoechst 33342 for at least 15 min prior to imaging. For measurements under confinement, both A549 cells and iPSCs were plated at the same densities described in *In vitro mechanical confinement assays* on 30-mm glass coverslips. For A549s, nocodazole synchronization was again done as previously described. After nocodazole release, cells were replenished with fresh culture media with 8 μM Hoechst 33342 for DNA staining. The glass coverslip with cells was then flipped upside down and placed on top of a 40-mm length rectangular glass coverslip with 30 μl droplet of 6.58-μm polystyrene spacer beads in complete media (prepared prior to DNA staining) to complete the confinement sandwich. One or more stainless steel metal weights were then added on top of the top coverslip to initiate confinement. For tumor/teratoma chromatin height

measurements, freshly harvested samples were fixed overnight using 4% paraformaldehyde at 4°C, permeabilized using 0.5% (v/v) Triton-X for 1h at room temperature, and finally stained with Hoescht 33342 overnight at 4°C. Small tumor/teratoma sections were sliced, submerged in 20-40 μl of PBS on a rectangular coverslip (either 35x50 or 45x50 mm^2). All samples were imaged using a Leica TCS SP8 system with a 63x/1.4 NA oil-immersion. All images were taken every 0.5 μm along the focus (Z stack) to cover the entire nuclei, whether it be interphase or mitotic. All image stacks were 3D-reconstructed using ImageJ. The first frame was used as the top view, and the tenth frame was used as the side view in a 36-frame 3D construction profile. For tumor/teratoma sections, the thinnest portion of the nucleus is treated as the height, due to the 3D nature of the sample preventing determination of the nucleus orientation.

Cell growth curves

At t = 0h, RFP-positive and RFP-negative clones (P3 and N3, respectively) were each seeded in a 24-well plate at extremely low density (2.6×10^2 cells/cm^2). Starting at t = 24 h, every 24h for 96h total, tile scanning was used to image one-half of each sample well. Imaging was performed on an Olympus IX71—with a 10x/0.2 NA objective—and a digital EMCCD camera. For every timepoint, the number of cells in each half-well was manually counted from the images, and then multiplied by two to get the total number of cells per

well, or the total population of each experimental condition. Fits to the exponential growth equation $y = ae^{kx}$ exclude t = 0h, where cell density is merely an estimate, and fits to $y = 10^{mx + b}$ exclude t = 0h and t = 96h.

Data reporting

Statistical methods were not used to predetermine sample size. The experiments were not randomized. Investigators were not blinded to allocation during experiments and outcome assessment.

Statistics and reproducibility

The statistical methods for each experiment are included in the corresponding Figure legends. All statistical analyses were done on GraphPad Prism 9.0. All experiments were biologically repeated and confirmed. Unless otherwise mentioned, all plots show MEAN ± SEM, and statistical comparisons are considered significant if $p<0.05$. n indicates the number of samples, cells, wells, etc. quantified in each experiment. Additionally, at least two separate investigators performed each experiment separately for reproducibility.

Chapter 5

In vivo condition and cell division lead to increase in genomic variation

Fig. 5.2 (A) iPSC-GFPLMNB1 part, some replicated data in Fig. 5.3 B, Fig. 5.5 B & C have been recorded in Live cell monitoring for factors affecting genome variation, *Biorxiv*, 2018, by Xia, Y., Zhu, K., Irianto, J., Andrechak, J.C., Dooling, L.J., Pfeifer, C.R., Discher, D.E. All mouse injections involved in this chapter (displayed in Fig. 5.1) were conducted by Jason Andrechak. Cell dissociation was conducted by Kuangzheng Zhu, Jason Andrechak, and Brandon Hayes. Dr. Yuntao Xia took iPSC-GFPLMNB1 images for Fig. 5.2 A, conducted sequencing in Fig. 5.5 B along with Dr. Jerome Irianto, and drew path for Fig. 5.5 C; Brandon Hayes took iPS-RFPLMNB1 images for Fig. 5.2 A, performed iPSC-RFPLMNB1 flow cytometry for Fig. 5.2 B, calculated all bottom panel data for Fig. 5.3 and executed flow analyses for Fig. 5.3 A and some Fig. 5.3 B, contributed to *in vivo* data to Fig. 5.4 D; Dr. Charlotte Pfeifer drew Fig. 5.5 A, arranged and replotted data for Fig. 5.5 E-F. Kuangzheng Zhu conducted Fig. 5.4 A-C, 5.5 D, took A549-RFPLMNB1 images for Fig. 5.2 A, performed iPSC-GFPLMNB1 and A549-RFPLMNB1 flow cytometry for Fig. 5.2 B, executed flow analyses for Fig. 5.3 C and some Fig. 5.3 B, prepared cells for Fig. 5.5 B, performed experiments and generated raw data for Fig. 5.5 C, performed experiments and calculated persistence length, cell shape information raw data for Fig. 5.5 E-F.

5.1 Introduction

Adherent cells growing *in vitro* and suspending cells are surrounded by a microenvironment more similar to liquid tumor and soft tissues than solid, stiff tumor. Adherent cells, with one side anchored on a petri dish while the other side submerged in liquid media (with similar density to water and serum), do not receive stretching and compressing forces from cells located on another layer, and can freely form rounded shape at prometaphase for chromosome alignment, while cells in 3D conditions or divide within confined space cannot. Last chapter has concentrated on applying mechanical confinement on cells growing in 2D culture to lead to chromosome mis-segregation followed by increase in reporter-neg%, while this chapter proceeds from mimicking to realistic 3D *in vivo* conditions, where different reporter cell types grow as xenografts to form tumors or teratoma with their reporter-neg% measured as the evaluation marker of genomic variation. The relationship between cell division in tumor and *in vitro* are compared, to further prove that both stiff 3D environment and cell division contribute to genomic variation.

Additionally, different A549 reporter-positive clones used for xenografts have phenotypical differences that bring our insights to chromosomes that can potentially be targeted with reporter system, as well as the meaningful consequences in phenotype

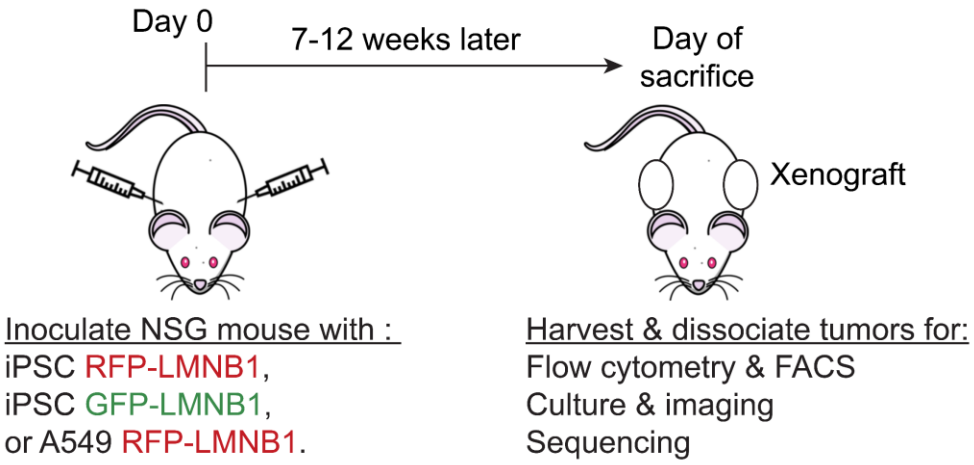

Figure 5.1: Schematic diagram of xenograft formation and harvest. Human cells xenografted at subcutaneous sites in immunodeficient NSG mice. When the iPSC teratomas or A549 tumors grew to a diameter of ~2 cm, they were harvested, disaggregated, and analyzed for Chr-5 reporter loss.

changes from genotype, once again confirming the widespread concept of central dogma: DNA-RNA-Protein.

5.2 *In vivo* condition generates heritable Chr loss reporter cells, and reporter-neg% scales with division more than *in vitro*

Immunodeficient mice were subcutaneously inoculated with human iPSCs or A549s expressing the *LMNB1* Chr-5 reporters (Fig.3.1,3.2). Teratomas derived from iPSCs

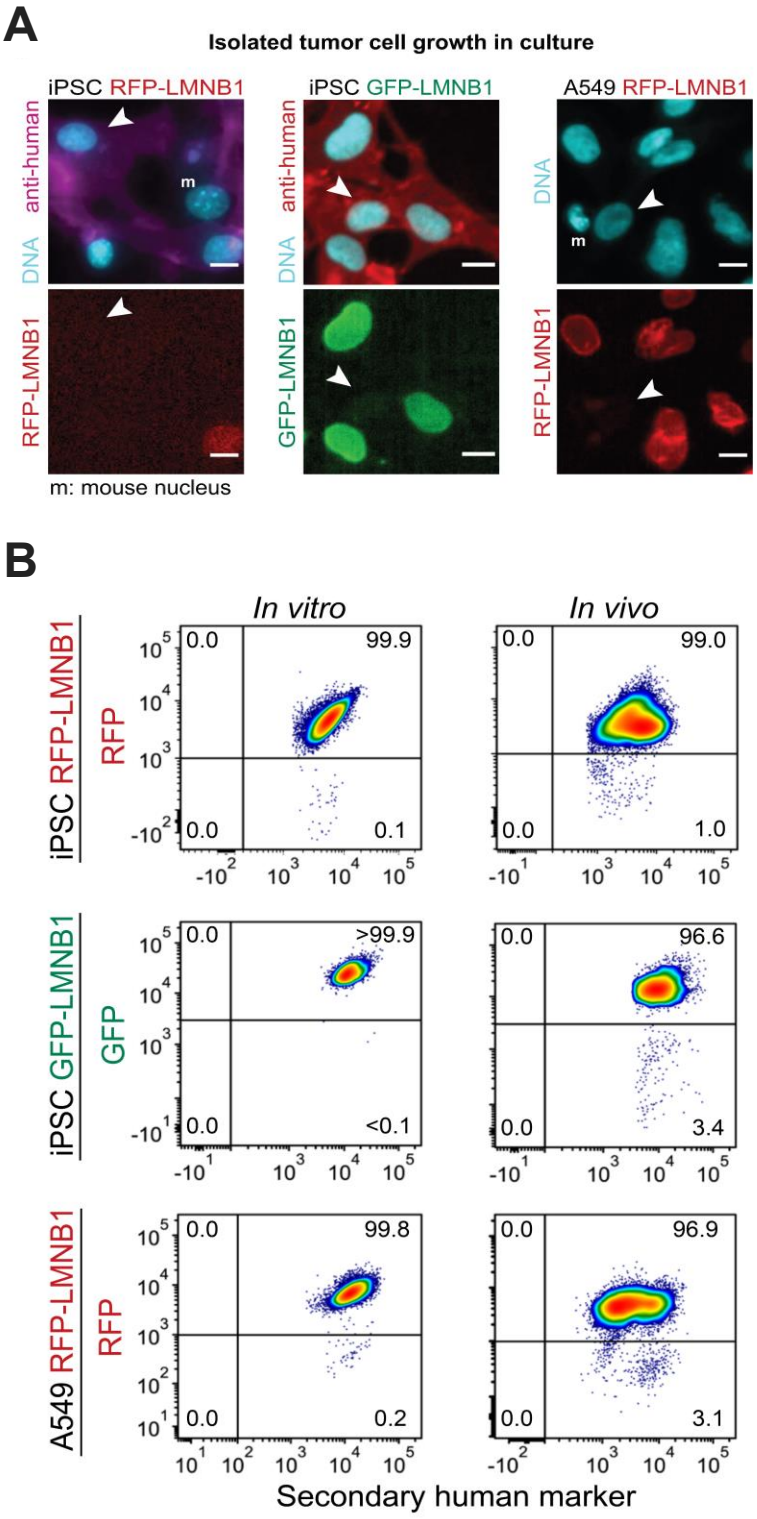

Figure 5.2: Flow cytometry shows increase of reporter-neg% *in vivo* than *in vitro*, verified by imaging.

(A) Images of Chr-5 reporter loss (LMNB1 protein) in 2D-cultures (~1 wk) of cells derived from iPSC teratomas (both clones) or from A549 tumors. Mouse cells show distinctive chromocenters in Hoechst stain of DNA. All Scale bars = 10 µm.

(B) Representative flow charts and gating strategies of reporter positive and negative distribution of *in vitro* reporter cells or reporter cells dissociated from mouse xenografts.

A: with Yuntao Xia and Brandon Hayes

B: with Brandon Hayes

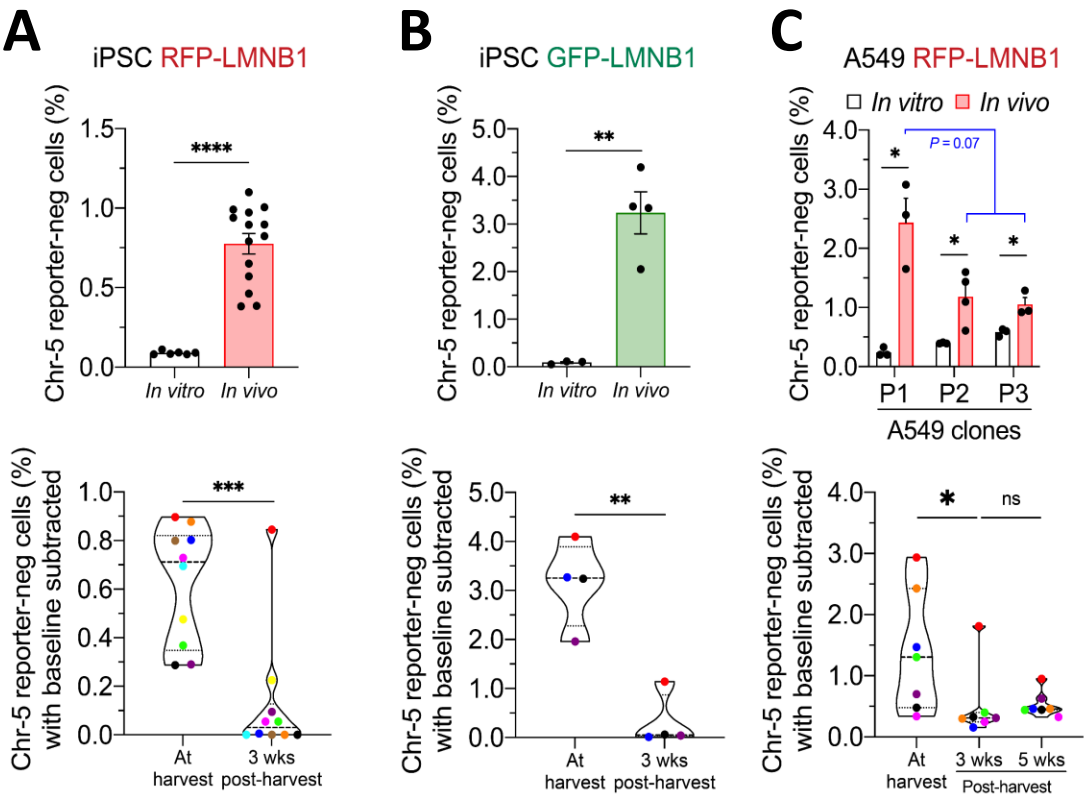

Figure 5.3: Increased reporter-neg% cells in iPSCs end up dead in most xenografts, while A549s show some growth. Quantitation of Chr-5 reporter-negative cells from various teratomas or tumors versus *in vitro* cultures, including 3-5 wk cultures post-harvest for assessments of persistent viability. n = 3 - 14 replicates; unpaired two-tailed t-test with Welch's correction between each confinement condition and its respective unconfined, standard 2D control. $^{**}p < 0.005$, $^{***}p < 0.0005$, $^{****}p < 0.0001$, ns, not significant. **(A)** iPSC RFP-LMNB1; **(B)** iPSC GFP-LMNB1 **(C)** A549 RFP-LMNB1, clones P1,P2,P3.

with Brandon Hayes

have not yet been reported to *cause* genetic changes despite their wide use in stimulating differentiation (Gutierrez-Aranda et al., 2010; Nelakanti et al., 2015, Cunningham et al., 2012), and bulk genetics analyses of tumor xenografts have argued against de novo changes (Woo et al., 2021). iPSC teratomas and A549 tumors (Fig.5.1) were harvested after ~2-3 months, flow-sorted for fluorescent-negative cells, and analyzed by bulk genetics methods,

which confirmed *in vivo* loss of Chr-5 (Fig. C3). The result rules out rare epigenetic changes (Shaffer et al., 2017). Cultures of disaggregated teratomas and tumors show rare human cells lack nucleus-localized GFP/RFP-LMNB1 (Fig.5.2 A) while immunostaining for human proteins including lamin-A (Fig. E1). The latter also serves as a differentiation marker for teratomas. A few mouse cells adhere in culture but possess distinctive nuclei with chromocenters (Fig.5.2 A). Importantly, flow cytometry analyses showed Chr-5 reporter-negative cells increased in all teratomas and tumors (Fig.5.2 B, Fig.5.3 top) based on identification with various human-specific markers (e.g. GFP-SEC61B in iPSCs; Fig. 3.2, 3.3). The iPSCs showed ~30-fold more loss of GFP-LMNB1 than time-matched, genetically stable controls; and distinctly edited iPSCs showed ~4-fold more loss of RFP-LMNB1 than time-matched 2D cultures. A549 tumors of three sub-clones (P1, P2, P3) also showed 2- to 10-fold more loss of Chr-5 versus standard 2D cultures.

Reporter-negative disaggregated cells are generally out-proliferated by reporter-positive cells, across multiple 2D cultures. Teratoma-derived reporter-negative cells mostly died by 3 weeks, with crucial exceptions of viable cells from two teratomas (Fig.5.3 A,B-bot); infrequent genetic changes in iPSCs are known to limit their use (Mandai et al., 2017). Reporter-negative A549s from tumors also decreased in percentage by 3 weeks of culture but then tended to grow (Fig.5.3 C-bot), consistent with robust persistence of the abnormal cancer cells versus normal iPSCs. Genetic change under the distinct stresses of 3D is nonetheless highlighted by the uniformly higher percentages of

reporter-negative cells from freshly harvested teratoma/tumor cells versus 2D cultures of the same cells. Proliferation under 3D stress *in vivo* is a likely determinant because differences in the percentage of RFP-neg cells between the three A549 RFP-LMNB1 clones (Fig.5.3 C-top) correlate with the distinct growth rates of the tumors. Indeed, cell volume estimates from confocal images (Fig.4.3) allow us to convert measured tumor sizes at harvest to total cell numbers (N), yielding a much stronger power-law of [% RFP-neg] ~ N^a (a = 0.44) for *in vivo* relative to standard *in vitro* cultures where cells round up and divide unstressed by the overlying fluid and [% RFP-neg] ~ N^b (b = 0.005) (Fig.5.4 A). A549 clone P3 leads to higher RFP-neg% under *in vitro* confinement than P1, while giving lower RFP-neg% with less proliferation *in vivo* than P1. This indicates that genetic changes are favored not only by high stiffness but also proliferation (Fig.5.4 A, C). This is also consistent with our *in vitro* studies of rigid confinement versus 2D-control (e.g. Fig.4.10).

To assess myosin-IIA's role in chromosome loss within solid tissue microenvironments, teratomas of myosin-IIA knockdown, *LMNB1*-edited iPSCs were harvested and disaggregated for comparisons to controls including time-matched 2D cultures. The latter again showed uniformly low levels of reporter loss, and teratomas showed the typical 1% loss that increased by ~50% in knockdown cells (Fig.5.4D), which is consistent with *in vitro* effects of knockdown in rigid confinement of iPSCs (Fig.4.10). Whereas solid teratoma masses have the same consistency as subcutaneous tumors rich in

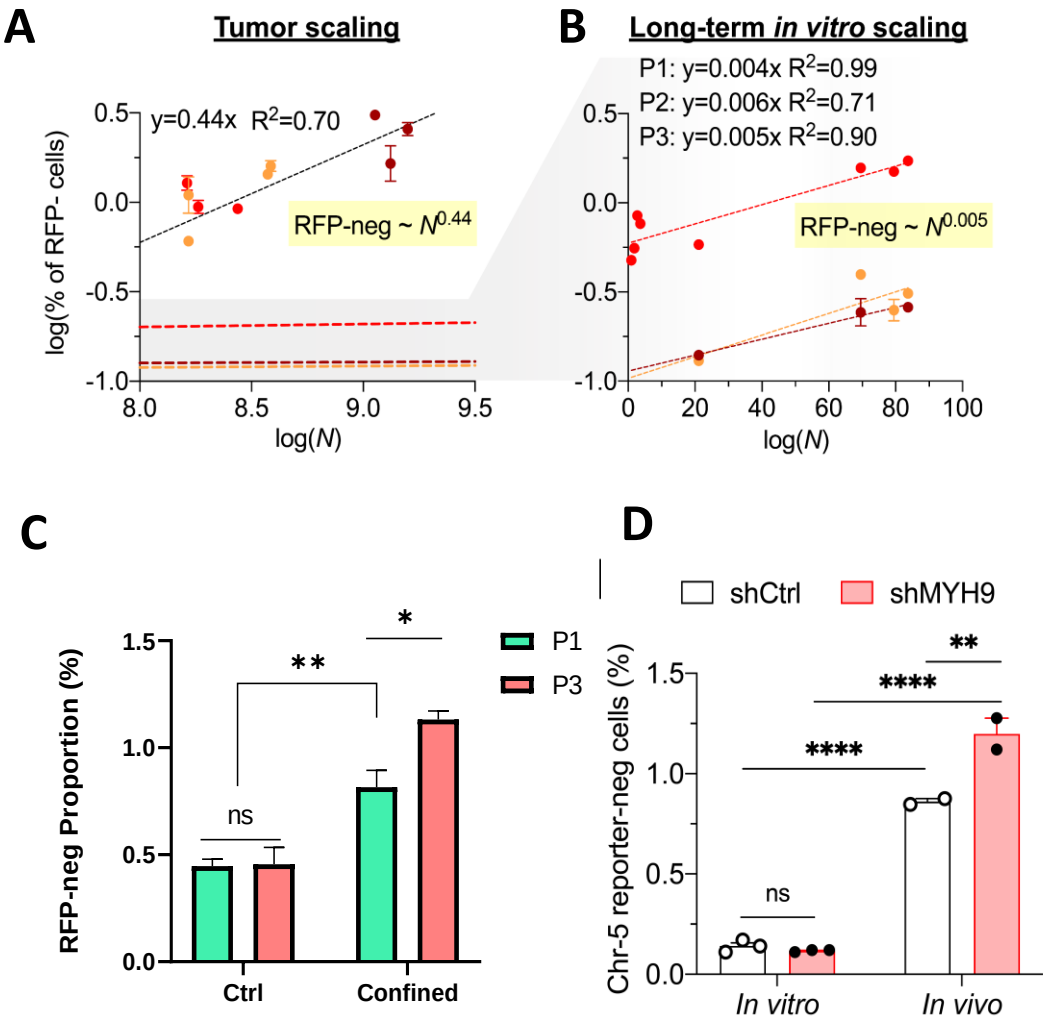

Figure 5.4: Reporter-neg% scales with cell number (*N*) in a power-law relationship, and knockdown of Myosin-IIa leads to more reporter-neg% *in vivo*. (A)-(B) Chreporter-neg% measured from A549 tumors in Fig 5.3 (C) top was plotted vs cell number *N* that is proportional to total division number and is estimated from tumor size and mean cell volume *in vivo*. Total cell number of *in vitro* control was estimated assuming all the cells are kept, with weekly splitting. The scaling slope *in vivo* is much higher than *in vitro*. (C) Flow cytometry analyses of Chr-5 reporter loss in A549 clone P1 or P3 in either confined or standard 2D cultures, conducted simultaneously. P3 shows higher Chr-reporter% than P1 after confinement. n=3. **(D)** Myosin-IIA knockdown iPSCs *in vivo* show the most Chr-5 reporter-negative cells (RFP-LMNB1) upon disaggregation of solid teratomas (of shMYH9) when compared to *in vivo* controls (shCtrl) or time-matched standard 2D-cultures (*in vitro*). n=2-3. (C)-(D): two-way ANOVA with Tukey's correction for multiple comparisons: *$p < 0.05$, **$p < 0.005$, ***$p < 0.0005$, ****$p < 0.0001$; ns, not significant. **D: with Brandon Hayes**

mouse-derived collagen and mouse cells (Swift et al., 2013). Such results are consistent with the lack of an effect of myosin-IIA inhibition in soft and solid microenvironments. The findings reaffirm the effects of myosin-II in maintaining genetic stability in rigid confinement (Fig.4.10), and again offer some insight into how a similar myosin-IIA knockdown directly in mouse embryo dermis can lead to cancer (Schramek et al., 2014).

5.3 Chr CNV can affect motility of isolated sub-populations

To illustrate use of the fluorescence reporters in relating heritable Chr differences to phenotype changes, particularly in growth and motility, we applied scRNA-seq to mixtures of four different A549 clones that are either all positive (P1-P4) or all negative (N1-N4) for the fluorescent Chr-5 reporter (**Fig.5.5 A**). Many cancer cells show spontaneous losses and gains of Chr's (e.g. **Fig. E 2**), and bulk DNA profiling shows clonally distinct CNVs, with the reporter approach providing a unique opportunity for confidence in finding one less allele of Chr-5 only in (N1-N4) cells (**Fig. 5.5A, E2**). However, we expected other CNV-derived phenotype differences in part because P1 tumors grow faster *in vivo* than P2 and P3 tumors (Fig.5.3 C, Fig. 5.4 A & B). Single-cell RNA-sequencing profiles showed that Chr-5 have the greatest number of upregulated genes (>1.28-fold change) when comparing all of the RFP-pos 'P' clones to RFP-neg 'N'

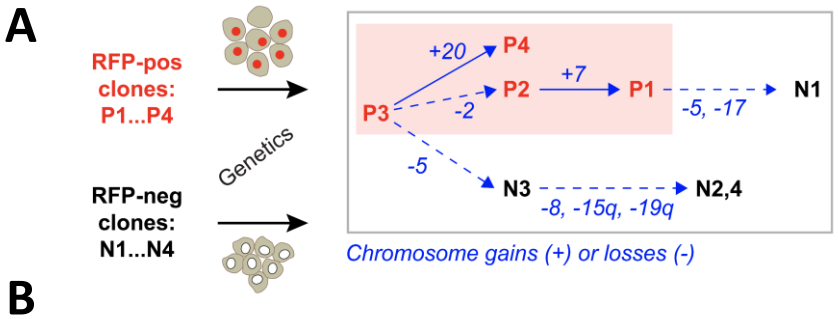
A
RFP-pos clones: P1...P4
Genetics
RFP-neg clones: N1...N4
P3
+20
P4
-2
P2
+7
P1
-5, -17
N1
-5
N3
-8, -15q, -19q
N2,4
Chromosome gains (+) or losses (-)

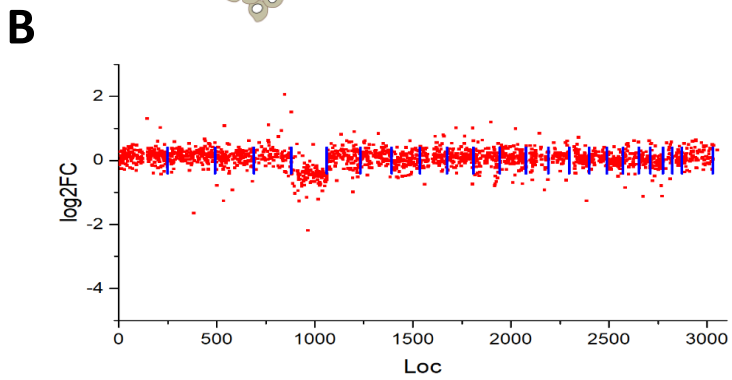
B
log2FC
Loc

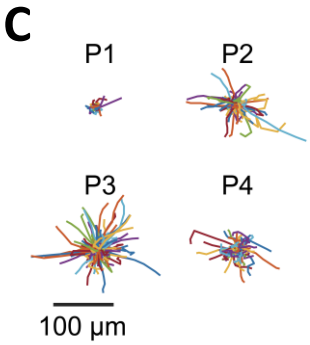
C
P1
P2
P3
P4
100 µm

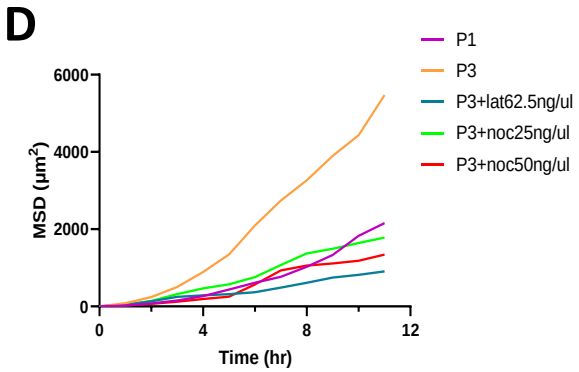
D
MSD (µm²)
Time (hr)
P1
P3
P3+lat62.5ng/ul
P3+noc25ng/ul
P3+noc50ng/ul

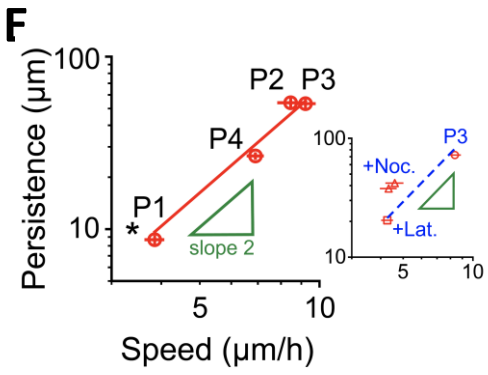
F
Persistence (µm)
Speed (µm/h)
P1
P2 P3
P4
slope 2
+Noc.
+Lat.

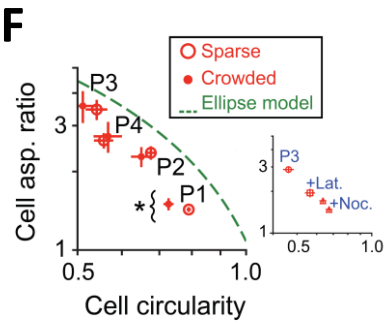
F
Sparse
Crowded
Ellipse model
Cell asp. ratio
Cell circularity
P1
P2
P3
P4
+Lat.
+Noc.

Figure 5.5: (Previous page) **Chr-5 reporter-neg A549 cell clones have genes on Chr-5 down-regulation, and other chromosome variation (Chr-7) leads to phenotypic changes within reporter-positive populations as well. (A)** Sorting of RFP-pos A549s followed by 3-4 days in standard culture leads to spontaneous generation of RFP-neg cells that corresponds to Chr-5. Four RFP-pos and four RFP-neg cells were clonally expanded for genomic characterization, revealing other gains and losses (blue) per the lineage map. **(B)** reporter-neg cells show decreased expression of *LMNB1* and many other genes on Chr-5 **(C)** Live-imaging of sparse cultures for 6h on plastic shows persistence scales with migration speed. (D) Mean square displacement, or random walk movement of P3 is slowed by microtubule or actin disruption, pheno-copying P1. **(E)** P1 slow-migration phenotype phenocopied by P3 cells with disruption of microtubules (with Noc) or F-actin (Lat: latrunculin-A). **(F)** Cell circularity and aspect ratio in both sparse and crowded culture shows the expected relationship for an ellipse. P1 cells are again phenocopied by P3 cells treated with Noc or Lat. n>100 cells per condition; $*p < 0.05$.

B: Sequencing: Yuntao Xia and Jerome Irianto

C: Path graphing:Yuntao Xia

E-F: Fitting: Charlotte Pfeifer

clones (Fig.5.5 B), consistent with a gene dosage effect. Chr-7 segregated P1 from P2-P4, (Fig.E2). P1 cells migrated more slowly and with less persistence (Fig.5.5 C-E). P3 cells with depolymerized F-actin or MT followed a similar trend (Fig.5.5 E,F, E3), pheno-copying the cytoskeletal deficit in P1 cells. P1 cells were also more rounded than P2-P4, with circularity closer to 1 (Fig.5.5F). Once again, P3 cells with depolymerized F-actin or MT followed a similar trend (Fig.5.5F, inset, Fig. E3), pheno-copying the cytoskeletal deficit in P1 cells. These results — despite being for 2D cultured cells — illustrate P1's phenotypic difference from P2's and P3's, as observed *in vivo* (Fig.5.5A).

5.4 Discussion

The hypothesis that mitosis within rigidly-constraining 3D microenvironments causes *heritable mechanogenetic* changes is supported by the mono-allelic chromosome reporter approach that directly reveals generation of rare GFP/RFP-negative cells that are to varying extent viable *in vivo*. Both normal (iPSC) and cancer (A549) reporter cells harvested from mice display significantly fold-change increase in reporter-neg%, confirming that high-stiffness environmental structure *in vivo* yields more genomic variations. Reporter-neg% in harvested A549 reporter cells dropped dramatically after undergoing culture *in vitro*, but this number started to increase before it reached 0. This indicates that not all–or even a great proportion of genomically altered cells–cannot survive, and the small proportion that survive are probably enough to lead to the next generation of mutated cancer cells. Indeed, it is reasonable to judge that Chr-5 reporter neg cells carry CNV other than Chr-5 and carry complicated heterogeneity, as indicated in our single cell genomics and karyotyping data (Fig. C1). Chromosomal loss is random, and many severe lethal CNVs have made cells hard to survive further. iPSCs, on the other hand, show reporter-neg% dropped to 0 for most of the teratoma, given the difficulty for normal cells with a lost chromosome to be viable. However, interestingly, one out of ten teratoma

shows 1% reporter-neg% after long-term culture, providing some possible understanding on the transition from normal somatic cells to abnormal whose viability and heritability constitute origins for cancer cell formation and progression.

Scaling of reporter-neg% with respect to cell number (*N*) gives an estimation on the trend of how fast CNV changes versus division rate. Total number of divisions includes all cell divisions that have happened for a single cell to become the total number of cells in a petri dish or xenograft by the time of measurement (sample calculation A1). The much greater power exponent *in vivo* than *in vitro* confirms the hypothesis that stiff environment leads to more chromosomal copy number variation, and the increase in reporter-neg% versus division proves that division is needed for increase in genome variation. This is also consistent with previous general data showing tissue mutation (reflected by reporter-neg%) is positively correlated with proliferation (reflected by cell number) and tissue stiffness (Yizhak, et al., 2019; Beroukhim, et al., 2010; Pfeifer, et al., 2017, Tomasetti and Vogelstein, 2015, Lawrence et al., 2013). Cells grow much more slowly *in vivo* than *in vitro*, because many initially injected cells couldn't survive, and also because stiff confinement slows down division (Lancaster et al., 2013; Fig. D1). Different A549 reporter-pos clones show different Chr-reporter loss levels *in vitro* and *in vivo*, and have different sizes of tumors by the time of dissection. The change of one chromosome is responsible for the overdose or underdose (insufficiency) of thousands of genes, which, as

expected, contributes to their different behaviors in migration and ability to live *in vivo*. Scrutinizing over those clones show that P1, with an extra copy of q-arm of Chr-7, are rounder in shape and less likely to migrate in 2D substrate. The central dogma that genotype affects phenotype has been reflected thoroughly and strictly, while more research can be executed if Chr-7 is targeted to be a chromosome reporter, in which case the transitioning from P1 to P3 can be understood and more changes in genotypic and phenotypic levels can be unveiled and discussed.

In addition, more substrate conditions at different stiffness in between subcutaneous tumor and liquid tumor (*in vitro*) can be used to discover a series of power exponents along with their continuous, functional relationship with stiffness (Young's Modulus E). If *in vivo* conditions are hard for controlling stiffness, embedding cells in 3D gels with specified compositions to control stiffness can be an alternative approach.

5.5 Materials and methods

Cell lines and tissue culture.

A549 cells were cultured in Ham's F-12 media (Gibco 11765047) supplemented with 10% (v/v) fetal bovine serum (FBS; MilliporeSigma, Catalog no. F2442) and 100 U ml^{-1} penicillin-streptomycin (Gibco, Catalog no. 15140122). All cells were passaged every 2-3 days using 0.05% Trypsin/EDTA (Gibco, Catalog no. 25300054). All A549 cells were incubated at 37^{o}C and maintained at 5% CO_2.The original A549 RFP-LMNB1 cell line was engineered by Sigma-Aldrich. The A549 cell line was obtained from the American Type Culture Collection (ATCC).

The following induced pluripotent stem cell (iPSC) lines were also used, all of which were acquired from the Coriell Institute for Biomedical Research and generated/validated by the Allen Institute for Cell Science: iPSC GFP-LMNB1 (AICS-0013 cl.210), iPSC RFP-LMNB1 GFP-SEC61B (AICS-0059 cl.36), and iPSC FBL-GFP NPM1-RFP (AICS-0084 cl.18). iPSCs were cultured in mTseR Plus medium (STEMCELL Technologies, Catalog no. 05825), with mTser Plus 5X supplement and 100 U ml^{-1} penicillin-streptomycin. For passaging and maintenance of iPSCs, cells were lifted with accutase (Sigma, Catalog no. A6964) at 37^{o}C and re-plated into 10-cm plates (Corning)

coated with Matrigel (Corning, Catalog no. 356231) following the Allen Institute of Cell Science's protocol. 10 mM ROCK inhibitor (Y-27632; STEMCELL Technologies, Catalog no. 72302) was added to replated cultures to help with adherence and to prevent differentiation. Passaging was done once iPSC cultures reached 70% confluency to prevent spontaneous differentiation. All iPSC lines were also cultured at 37^{o}C and maintained at 5% CO_2.

Monoallelic chromosome tagging

For all attempted monoallelic chromosome reporters as described in Fig. 1E, all donor constructs were a gift from Allen Institute of Cell Science: AICSDP-8:TOMM20-mEGFP (Addgene plasmid #87423; http://n2t.net/addgene:87423; RRID:Addgene_87423), AICSDP-13:FBL-mEGFP (Addgene plasmid #87427; http://n2t.net/addgene:87427; RRID:Addgene_87427), AICSDP-35:AAVS1-mEGFP (Addgene plasmid #91565; http://n2t.net/addgene:91565; RRID:Addgene_91565), AICSDP-42:AAVS1-mTagRFPT-CAAX (Addgene plasmid #107580; http://n2t.net/addgene:107580; RRID:Addgene_107580), AICSDP-1:PXN-EGFP (Addgene plasmid #87420; http://n2t.net/addgene:87420; RRID:Addgene_87420), AICSDP-10:LMNB1-mEGFP (Addgene plasmid #87422; http://n2t.net/addgene:87422; RRID:Addgene_87422), AICSDP-52: HIST1H2BJ-mEGFP (Addgene plasmid #109121;

http://n2t.net/addgene:109121 ; RRID:Addgene_109121), AICSDP-7:SEC61B-mEGFP (Addgene plasmid # 87426; http://n2t.net/addgene:87426; RRID:Addgene_87426).

All knock-in reporter lines were generated following the protocol established in (1) using CRISPR/Cas9 technology. Donor plasmids were designed such that unique designs for each target locus contain 5' and 3' homology arms (1 kb each) for the desired insertion site, based on the GRCh38 reference human genome. For editing, we use the ribonucleic protein (RNP) method with recombinant wild type *S. pyogenes* Cas9 protein pre-complexed with a synthetic CRISPR RNA (crRNA) and a trans-activating crRNA (tracrRNA) duplex. Recombinant wild-type Cas9 protein was purchased from the University of California–Berkeley QB3 Macrolab, while crRNA and tracrRNA oligonucleotides were designed by and purchased from Horizon Discovery. For transfection of donor templates into target cells, we used the electroporation using a Gene Pulser Xcell Electroporation System (Bio-Rad). 700,000 targets cells were lifted using 0.05% Trypsin/EDTA, resuspended in 200 ul of fresh media without penicillin-streptomycin, and loaded into a 0.4-cm cuvette. 4 µL of both 10 µM crRNA:tracrRNA duplex and 10 µM recombinant Cas9 protein were added to the cell solution, as well as 8 µg of donor plasmid. Electroporation conditions were as follows: (1) A549 and H23: 200V with 45 ms pulse length using a square-wave protocol; (2) U2OS: 160V with 30 ms pulse length using a square-wave protocol. After electroporation, cells were allowed to expand for ~1 week and then enriched via fluorescence-activated cell sorting (FACS), as described

below. 3-5 FACS enrichment cycles were performed to achieve a pure reporter-positive population.

Single cell RNA-sequencing.

RNA libraries were constructed using the Chromium Single Cell Gene Expression kit (v3.1, single index, Catalog no. PN-1000128; PN-1000127; PN-1000213) from 10X Genomics per the manufacturer's instructions. The libraries were submitted to the University of Pennsylvania's Next Generation Sequencing Core for sequencing using NovaSeq 6000 (100 cycles) from Illumina. Raw base call (BCL) files were analyzed using CellRanger (version 5.0.1) to generate FASTQ files and the "count" command was used to generate raw count matrices aligned to GRCh38 provided by 10x genomics. For teratoma samples, FASTQ files were aligned to both GRCh38 and GRCm38. The cells are labeled to be human/mouse cells if more than 90% of the UMIs are aligned to GRCh38/GRCm38. The data generated was imported as a Seurat object (4.0.0) for future downstream analysis (2). Cells were filtered to make sure that they expressed 500 and 6,000 genes inclusive and had less than 10 percent mitochondrial content. Data was normalized using the "LogNormalize" method or sctransform package (0.3.2) (3). Differential expression analysis was performed using the "FindAllMarkers" command and the output was used for the volcano plot. The very first 30 dimensions were used to generate UMAP. Cell cycle analysis was performed using "CellCycleScoring" command.

Cell type annotations

Raw expression matrices were used as the input for the singleR (1.4.1) package (Aran et al., 2019). The cell types were annotated based on Human Primary Cell Atlas (Mabbott et al., 2013).

Reporter validation via single-nucleotide polymorphism arrays & analysis

Genomic DNA was isolated from a minimum of 3.0×10^5 cells with the Blood & Cell Culture DNA Mini Kit (Qiagen, Catalog no. 13323) per the manufacturer's instructions. In the event that cells were either very rare (such as reporter-negative cells) or had poor viability after FACS enrichment (specifically, iPSCs), genomic DNA was amplified post-extraction using the Illustra Single Cell GenomiPhi DNA Amplification Kit (GE Healthcare Biosciences, Catalog no. 29108107) following the manufacturer's instructions. All DNA samples were sent to The Center for Applied Genomics Core in The Children's Hospital of Philadelphia, PA, for Single Nucleotide Polymorphism (SNP) array HumanOmniExpress-24 BeadChip Kit (Illumina). For this array, >700,000 probes have an average inter-probe distance of ~4kb along the entire genome. For each sample, the Genomics Core provided the data in the form of GenomeStudio files (Illumina). Chromosome copy number and LOH regions were analyzed in GenomeStudio by using cnvPartition plug-in (Illumina). Regions with one chromosome copy number are not

associated with LOH by Illumina's algorithm. Hence, regions with one chromosome copy number as given by the GenomeStudio are added to the LOH region lists. SNP array experiments also provide genotype data, which was used to give Single Nucleotide Variation (SNV) data. In order to increase the confidence of LOH data given by the GenomeStudio, the changes in LOH of each chromosome from each sample were cross referenced to their corresponding SNV data. After extracting data from GenomeStudio, all data analysis was done on Matlab.

Lentiviral packaging and delivery

MYH9 silencing was performed by lentiviral-driven expression of short-hairpin RNAs purchased from Sigma-Aldrich, using the pLKO backbone construct. The following shRNA were used: TRCN0000285480, TRCN0000029468, TRCN0000029466, TRCN0000276055, and TRCN0000276070. For non-targeting shRNA control, the pLKO-sh-HSC plasmid was a gift from Do-Hyung Kim (Addgene plasmid # 46896 ; http://n2t.net/addgene:46896 ; RRID:Addgene_46896). Lentivirus was produced in HEK293T cells using MirusBio TransIT-Lenti Transfection Reagent (Catalog no. MIR 6604) following the manufacturer's protocol. Lentiviral production was allowed to occur for 48h, after which the supernatant was collected. Lentivirus was concentrated and purified from traces of fetal bovine serum using the PEG-it Virus Precipitation Solution (System Biosciences, Catalog no. LV810A-1) following the manufacturer's protocol.

Infected cells were selected by incubation using 1 μg ml^{-1} puromycin (Corning, Catalog no. 61385RA).

Flow cytometry and FACS

All flow cytometry was performed on a BD LSRII (Benton Dickinson) and analyzed with FCS Express 7 software (De Novo Software). All studied cell lines were detached by brief trypsinization (for all cancer lines in 2D culture) or with accutase (for iPSCs and 3D-spheroids), washed, and resuspended in FACS buffer (PBS + 5% FBS) with 1.0 μg ml^{-1} DAPI (MilliporeSigma, Catalog no. 09542). For all dissociated tumor/teratoma xenograft quantification of reporter-negative subpopulations, dissociated cells were washed and resuspended in PBS + 5% (v/v) BSA containing mouse BD Fc Block (Clone 2.4G2; BD Biosciences, Catalog no. 553141) at a 1:500 dilution of the stock. Cell suspensions were incubated at 4°C for 30 min and agitated occasionally to prevent cell settling. Once the 30-min incubation period elapsed, anti-human IgG (Rockland Immunochemicals, Catalog no. 109-4139) was spiked into the FACS buffer for a final 1:500 dilution. Cell suspensions were again incubated at 4°C for 30 min and agitated occasionally to prevent cell settling. Cells were then washed twice with FACS buffer and incubated with a 1:500 dilution of donkey anti-rabbit AlexaFluor 647-conjugated secondary antibody against the anti-human IgG in FACS buffer for 30 min at 4°C. Finally, cells were washed twice and resuspended in FACS buffer containing 1.0 μg ml^{-1} DAPI. For fluorescence-activated cells sorting, or

FACS, cells were prepared in the same way as described above except that freshly prepared sterile FACS buffer was used and no DAPI was included. FACS was performed on either a BD FACS Aria II or a BD FACS Jazz. Prior to any assay that assessed reporter-negative subpopulation generation, cells were FACS-enriched for only reporter-positive cells. Cultures were also routinely FACS-enriched every 2 weeks to remove spontaneous, naturally occurring aneuploid reporter-negative cells.

For gating, forward scatter parameters FSC-A vs. FSC-H and side scatter parameters SSC-A vs. SSC-H were used to remove aggregates from analysis. Live cells were gated on using forward scatter and side scatter (FSC-A vs. SSC-A). DAPI was further used to discriminate between live cells and debris/dead cells. For tumor/teratoma flow cytometry quantification, additional gates were added to remove mouse cells from human xenograft samples. Only anti-human IgG-high cells were gated on. In the case of teratomas, when possible, a secondary GFP-SEC61B marker unique to the human iPSCs was also used to further remove any potential mouse cell contaminants in the analysis.

Immunofluorescence and imaging

Cells were fixed in 4% formaldehyde (Thermo Fisher Scientific, Catalog no. 28908) for 15 min, followed by permeabilization by 0.5% Triton-X (MilliporeSigma, Catalog no. 112298) for 15 min, and blocked with 5% bovine serum albumin (BSA; MilliporeSigma, Catalog no. A7906) for 30 min and overnight incubation in primary antibodies (1:500

dilution). The cells were then incubated in secondary antibodies (1:500 dilution) for 1.5h, and their nuclei were stained with 8μM Hoechst 33342 (Thermo Fisher, Catalog no. 62249) for 15 min. When mounting is involved, Prolong Gold antifade reagent was used (Invitrogen, Catalog no. P36930). Micronucleated cells were classified manually by distinct staining by Hoescht 33342 of structures outside of the main nucleus. Epifluorescence imaging was performed using an Olympus IX71 with a digital camera (Photometrics) and a 40x/0.6 NA objective. For certain samples, confocal imaging was performed on a Leica TCS SP8 system with a 63x/1.4 NA oil-immersion. Live imaging was performed on an EVOS FL Auto Imaging System with 10× or 20x/0.6 NA object in normal culture conditions (37°C and 5% CO2; complete culture medium as specified above).

Mouse models and xenograft dissociation

For *in vivo* studies, non-obese diabetic/severe combined immunodeficient (NOD/SCID) mice with null expression of interleukin-2 receptor gamma chain (referred to in text as NSG mice) were used (Alvey et al., 2017). Mice were procured by the University of Pennsylvania Stem Cell and Xenograft Core. Mouse xenografts were generated in 8- to 12-week old NSG mice by subcutaneous or intraperitoneal injection (as a 100 μL bolus) of approximately 0.5-1.0 $\times$ 10^6 A549 cancer cells (for tumors) or iPSCs (for teratomas). For injection, cells were resuspended in sterile, serum-free media with Matrigel at a 7:3

volumetric ratio. Tumor area was calculated as $A = \pi/4 \times L \times W$, where L and W represent length and width, respectively. For all *in vivo* studies, tumor/teratomas were grown up until they reached ~2-cm in either length or width, after which mice were humanely euthanized. All mouse experiments were planned with and performed in accordance with protocols approved by the University of Pennsylvania's Institutional Animal Care & Use Committee.

For dissociation, tumor/teratomas in humanely euthanized mice were disaggregated using dispase (Corning, Catalog no. 354235) supplemented with 4 mg ml^{-1} collagenase IV (Thermo FIsher Scientific, Catalog no. 17104-019) and DNAse I (Thermo Fisher Scientific, Catalog no. 18068-015) at 1 µL per 1 mL of dispase solution. Tumor/teratomas were allowed to dissociate for 30 min while incubated at 37°C. Dissociated cells were centrifuged at 300×g, washed with Dulbecco's phosphate-buffered saline (PBS; Gibco, Catalog no. 10010-023), and resuspended in ACK lysis buffer to lyse red blood cells. After lysis, cells were washed once more and used for flow cytometry quantification, single-cell sequencing experiments, or plated back following the previously described cell culture methods.

Power-law scaling *in vitro* and *in vivo*.

Scaling calculations as depicted in Fig. 4L were done as follows: For cells dissociated from tumors *in vivo*, cell number was calculated based on the following equation: $N=\rho_c m/\rho_m$. Cell density ρc (expressed in number/cm^3) was estimated from tumor section images using

3D reconstruction (ImageJ) from confocal microscopy. Mass density ρm was assumed to be 1.16 g/cm^3. The volume of each tumor was recorded prior to dissociation. For *in vitro* cell number calculations, all A549 RFP-LMNB1 clones were cultured for 278 days after being FACS-enriched and were left unperturbed for the entire duration. Cells were only passaged at ~70-80% confluency (and at each passaging timepoint, a sample of cells was analyzed via flow cytometry for reporter-negative quantification). The cell number used for analysis is the theoretical total number of cells that would have been generated from the original culture (assuming an infinitely large culture vessel and unlimited nutrients). For scaling calculation associated with MPS1 inhibition and confinement kinetics in Fig.4.6, cell number is calculated in similar way as for the theoretical total number described before. However, doubling time for each conditions are not necessarily the same: for A549 MPS1 inhibition and DMSO control, cells were seeded at low density and didn't reach full confluency before passaging, so the normal doubling time of A549 in this study (~19 hr) is used; For confinement and its control, however, cells were seeded at semi-confluent density to start, cell number was calculated based on logistic growth function described in Fig. S5, passaged every 4 days, and assuming all cells dissociated each time were plated back for the next cycle.

Tumor staining

Sectioning and trichrome staining of A549 tumors were performed by the Molecular Pathology and Imaging Core (University of Pennsylvania). Tumors were excised, fixed in

4% formaldehyde overnight at 4°C, washed in PBS, and dehydrated in 70% ethanol prior to submission. Imaging was done using an Olympus IX inverted microscope with a 40x/0.6 NA or 20x/0.4 NA objective and equipped with a sCMOS camera or a Leica TCS SP8 system with a 63X/1.4 NA oil-immersion (provided and maintained by the University of Pennsylvania Cell & Developmental Biology Microscopy Core).

Live-cell imaging of cell motility

All studied A549 RFP-LMNB1 clones were plated 24h prior to assay at a density of 4,000 cells per well in a 12-well plate (Corning). Live-imaging was done using an EVOS FL Auto Imaging System with a 10x objective with cells under normal culture conditions (37°C and 5% CO_2; complete culture medium). One image was every hour for a total of 6 hours. Migration paths of cells were traced with MATLAB, with the original location of cells labeled as the origin coordinate (0,0). Speed was calculated using the ImageJ Plugin MtrackJ. For each cell, its location was tracked from t = 0 to 6 h at 1h intervals, and their 2D locations (x_i, y_i) were recorded by MtrackJ and exported into excel. The mean speed for each cell at 6 hour span was calculated as the summation of all paths traveled divided by time span. Mathematically, $Speed = \frac{\sum_{i=1}^{6}\sqrt{(x_i - x_{i-1})^2 + (y_i - y_{i-1})^2}}{6\ hr}$, where i denotes the time frame for each cell imaged. Persistence length of each type of clone or condition was calculated as $P = \frac{\bar{D}}{|\overline{\mathbf{v}}|}$.

Data reporting

Statistical methods were not used to predetermine sample size. The experiments were not randomized. Investigators were not blinded to allocation during experiments and outcome assessment.

Statistics and reproducibility

The statistical methods for each experiment are included in the corresponding Figure legends. All statistical analyses were done on GraphPad Prism 9.0. All experiments were biologically repeated and confirmed. Unless otherwise mentioned, all plots show MEAN ± SEM, and statistical comparisons are considered significant if $p<0.05$. n indicates the number of samples, cells, wells, etc. quantified in each experiment. Additionally, at least two separate investigators performed each experiment separately for reproducibility.

Appendix A

Supplementary materials for chapter 1

Kuangzheng Zhu performed calculation in this supplementary chapter.

A.1 Sample Calculations

Sample Calculation A.1: Estimation of bacteria and human genetic mutation rate in mutation per site per cell generation.

Bacteria or unicellular eukaryotes carry out 0.003 mutations per genome per cell generation (Drake et al., 1998). Bacterial genome is estimated to range from 0.6 to 6 megabases (Fournier and Raoult, 2017).

$mutation\ rate = \frac{0.003\ mutations\ per\ genome\ per\ cell\ generation}{0.6\ to\ 6{\times}10^{6} bases}$=$5\times 10^{-9}\ to\ 5\times 10^{-10}$ mutation per base (or site) per cell generation, in the order of magnitude of scale of 10^{-9} to 10^{-10}.

The number of cells in a new born infant is about 1 trillion (Osgood, 1955).

Total number of cell divisions that have occurred to form the infant constitute the total number of cell generations for each biological generation. In order to form 2^n cells, $\sum_{i=1}^{n-1} 2^i$ divisions are needed. Each division, regardless of direct or indirect contribution to the formation of final cells, has mutation chances. Therefore, the total number of divisions is the geometric series $\sum_{i=1}^{n-1} 2^i$, evaluated to be $2^n - 1$. In this study, cell number for each condition is greater than 1 million, so $2^n - 1$ can be treated as 2^n, where cell number can be treated as identical to total division numbers. With one trillion cells in new born infant, there have been 1 trillion divisions occurred. Therefore,

$mutation\ rate = \frac{10^{-8}\ mutations\ per\ site\ per\ generation}{10^{12} cell\ generation\ per\ generation}$=$10^{-20}$ mutation per site per cell generation. This is an underestimation in that daughter cells formed from division but died are not counted, and the mutations occur after infant is born are also part of biological generation but is neglected here. The following schematic diagram shows how division number and cell number correlate:

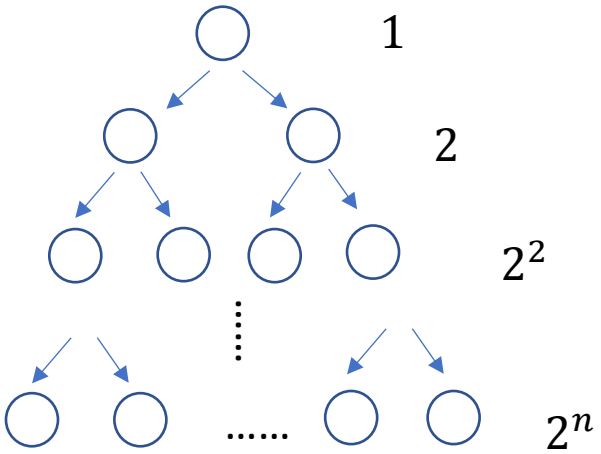

Appendix B

Supplementary materials for chapter 2

Data in Fig. B.1 to B.3 in this chapter have been published in Nuclear rupture at sites of high curvature compromises retention of DNA repair factors. *The Journal of Cell Biology*, 2018, *217*(11), 3796–3808, by Xia, Y., Ivanovska, I.L., Zhu, K., Smith, L., Irianto, J., Pfeifer, C.R., Alvey, C.M., Ji, J., Liu, D., Cho, S., Bennett, R.R., Liu, A.J., Greenberg, R.A., Discher, D.E.; Fig. B.5 images have been recorded in Live cell monitoring for factors affecting genome variation, *Biorxiv*, 2018, by Xia, Y., Zhu, K., Irianto, J., Andrechak, J.C., Dooling, L.J., Pfeifer, C.R., Discher, D.E.. Dr.Yuntao Xia conducted Fig. B.2, B.3 A and C; Kuangzheng Zhu conducted Fig. B.1, B.3 B, B.4, B.5.

B.1 Supplementary Figures

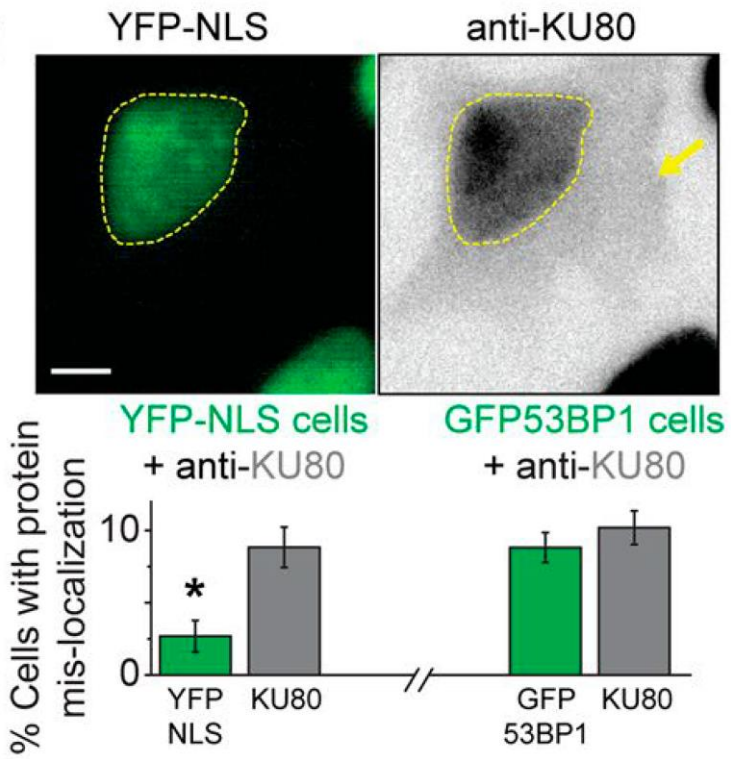

Figure B.1: Repair factor relocates into nucleus more slowly than NLS. KU80 is still in the cytoplasm (arrow) when YFP-NLS is fully within the nucleus, indicating that YFP-NLS may recover faster than KU80 after rupture. In contrast, both GFP-53BP1 and KU80 are seen in cytoplasm together (bar graph), indicating these two may recover at similar rates.

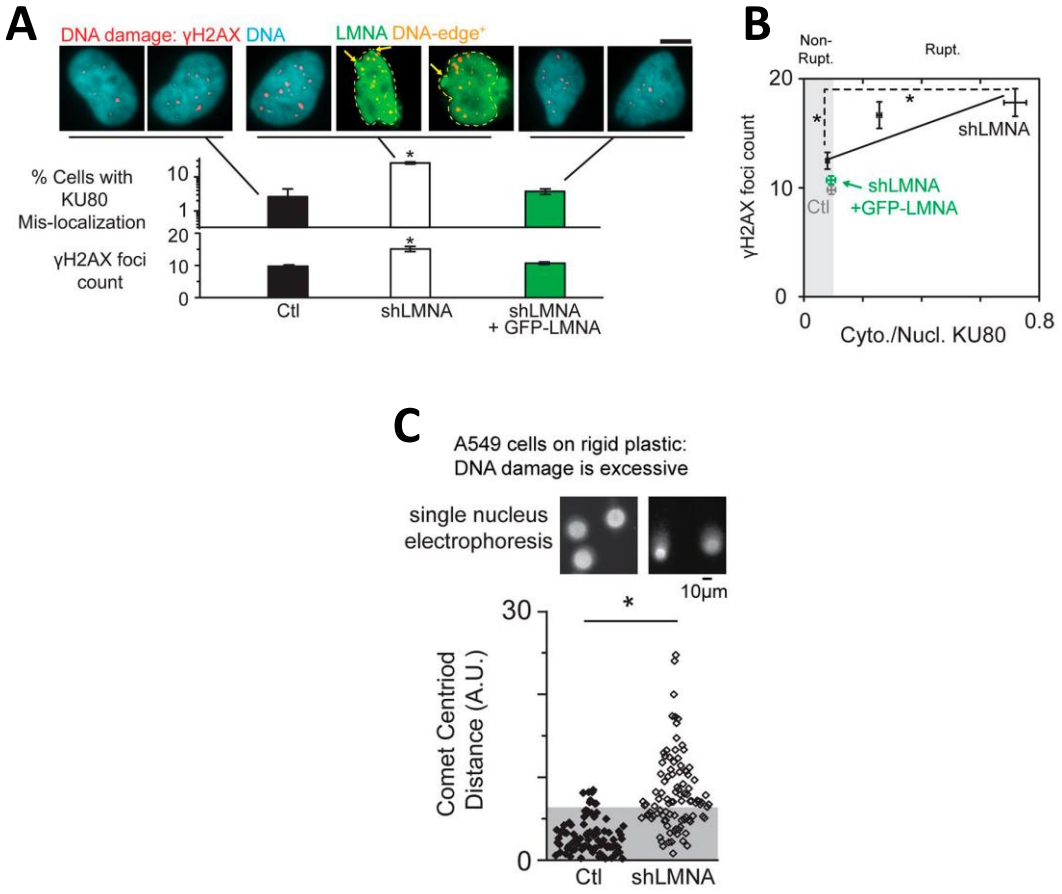

Figure B.2: Ruptured nuclei exhibit an excess in DNA damage marker. (A) Lamin A knockdown increases the fraction of cells with mislocalized cytoplasmic KU80 and excess DNA damage as indicated by γH2AX foci. GFP-LMNA rescues both effects. γH2AX foci in nuclei of shLMNA cells are not enriched near lamina rupture sites (arrows). n > 150 cells in three experiments. scale bar = 10 μm. **(B)** For shLMNA cells, ruptured nuclei with higher cytoplasmic/nuclear KU80 have higher γH2AX foci counts compared with nonruptured ones with low cytoplasmic/nuclear KU80. Ctl and GFP-LMNA–rescued cells rarely rupture and show low cytoplasmic/nuclear KU80 and low γH2AX foci counts. n > 150 cells in three experiments. **(C)** Comet assay shows higher DNA damage level in A549 shLMNA cells. n > 100 nuclei in three experiments. (A)-(C): *$p < 0.05$.

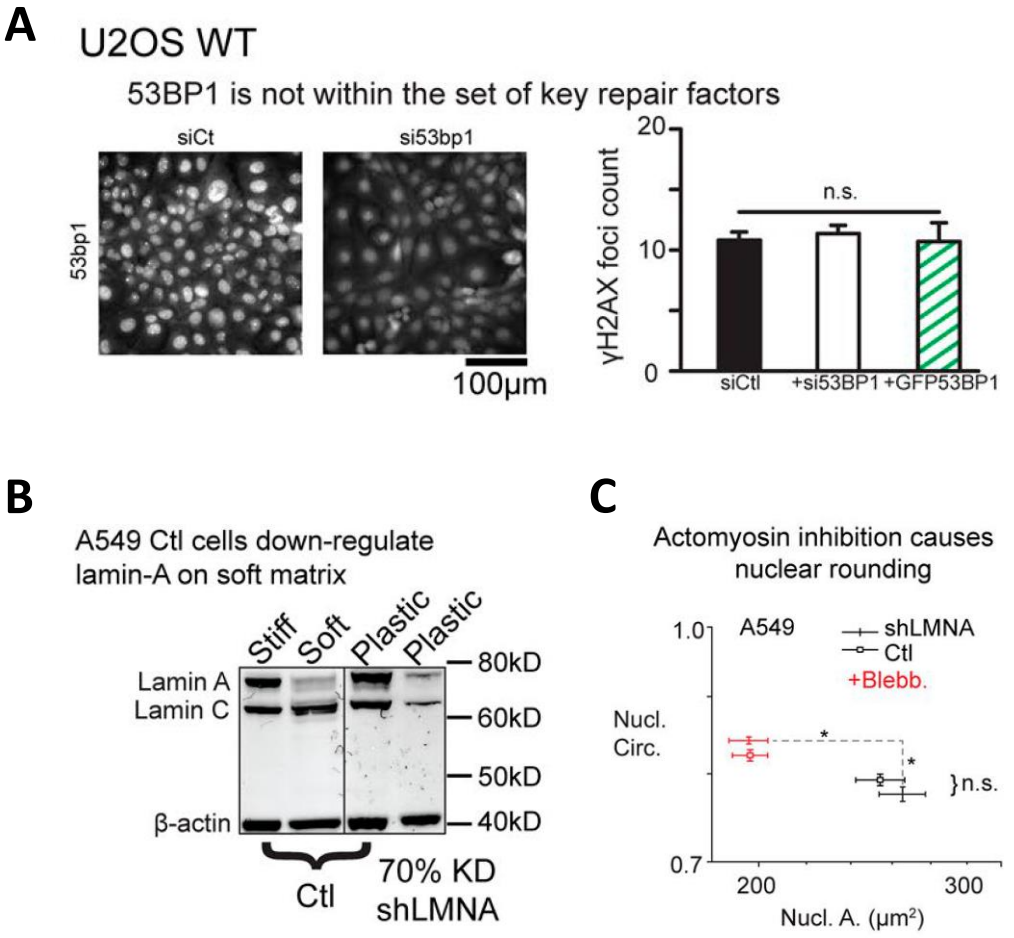

Figure B.3: Not all repair factors are essential; change in stiffness in substrate or contractility can alter cell shape with lamina amount change. (A) Either knockdown or overexpression of 53BP1 does not change γH2AX foci count. n > 100 cells in three experiments. (B) Lamin A level of A549 Ctl cells is mechanosensitive, but A549 shLMNA cells have low lamin A even on stiff substrate. (C) Nuclear circularity versus nuclear area of A549 Ctl and shLMNA cells on plastic with/without Blebbistatin treatment. Nuclear circularity decreases after siLMNA in U2OS cells. n > 50 cells per group in three experiments. * $p < 0.05$, n.s., not significant.

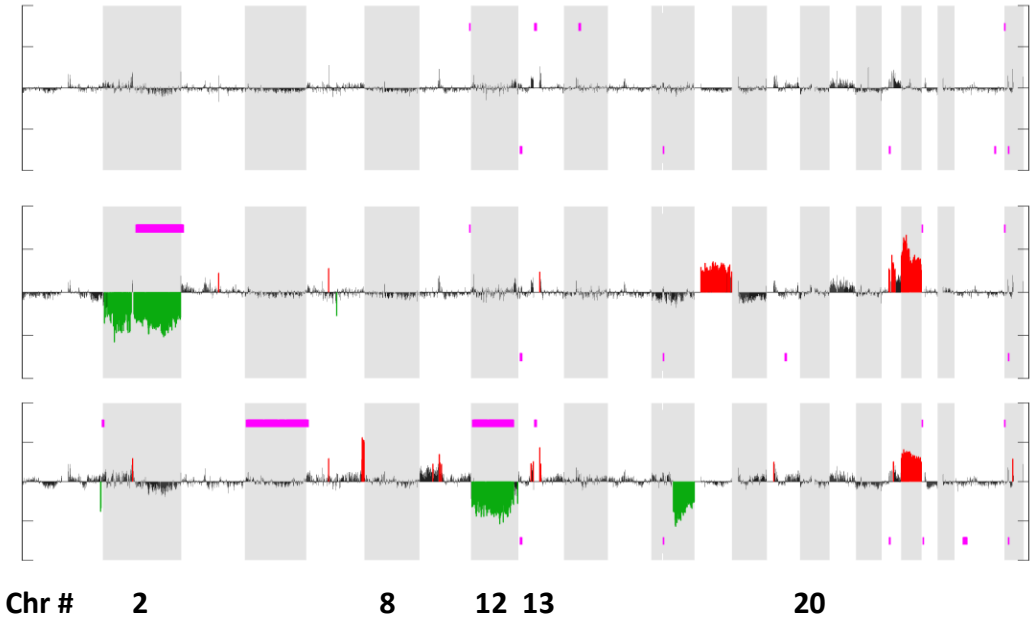

Figure B.4: SNPa of the 3 clones from repair-factor knockdown A549 cell bulk culture. CN values were subtracted from a control clone. All 3 clones show unidentical genomes.

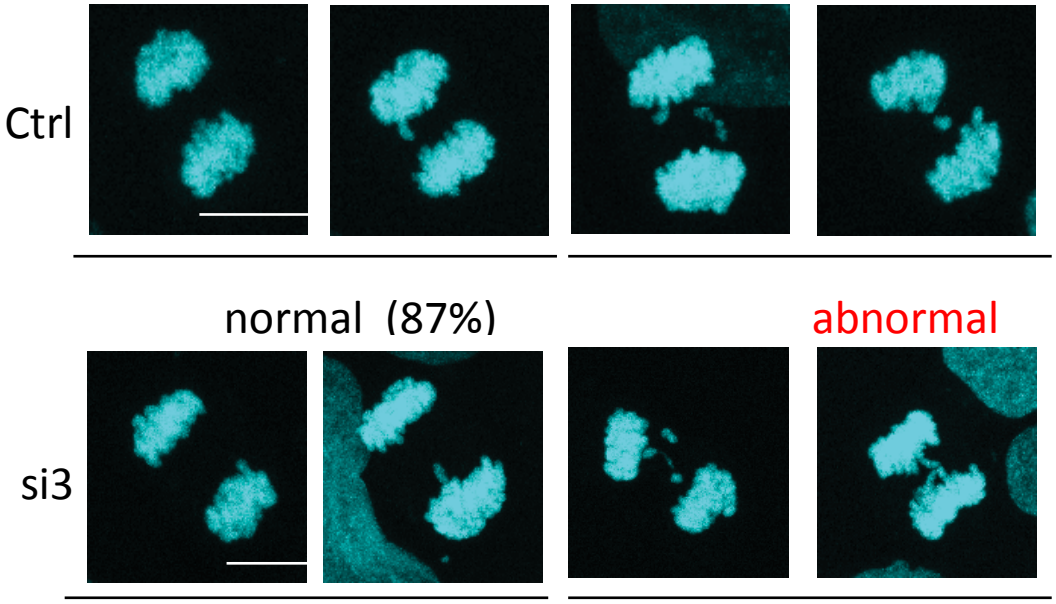

Figure B.5: Repair-factor knockdown leads to chromosome mis-segregation during mitosis. A549 cells were treated with combinatory siRNA of KU80, BRCA1, and BRCA2, or siCtrl, respectively. They were synchronized with nocodazole, and then released, fixed, and imaged under confocal microscopy. Anaphase cells with lagging chromosome (abnormal division) is identified to be more in repair-factor knockdown than Ctrl. All Scale bars = 10 μm.

Appendix C

Supplementary materials for chapter 3

Fig. C.1 A-C have been recorded in Live cell monitoring for factors affecting genome variation, *Biorxiv*, 2018, by Xia, Y., Zhu, K., Irianto, J., Andrechak, J.C., Dooling, L.J., Pfeifer, C.R., Discher, D.E.. Dr. Yuntao Xia, conducted Fig. C.1 B; Dr. Jerome Irianto developed code for SNPa sequencing. Mai Wang did sequencing for Fig. C.1 D; Kuangzheng Zhu prepared cells for Fig. C.1 D and conducted the rest.

C.1 Supplementary Figures

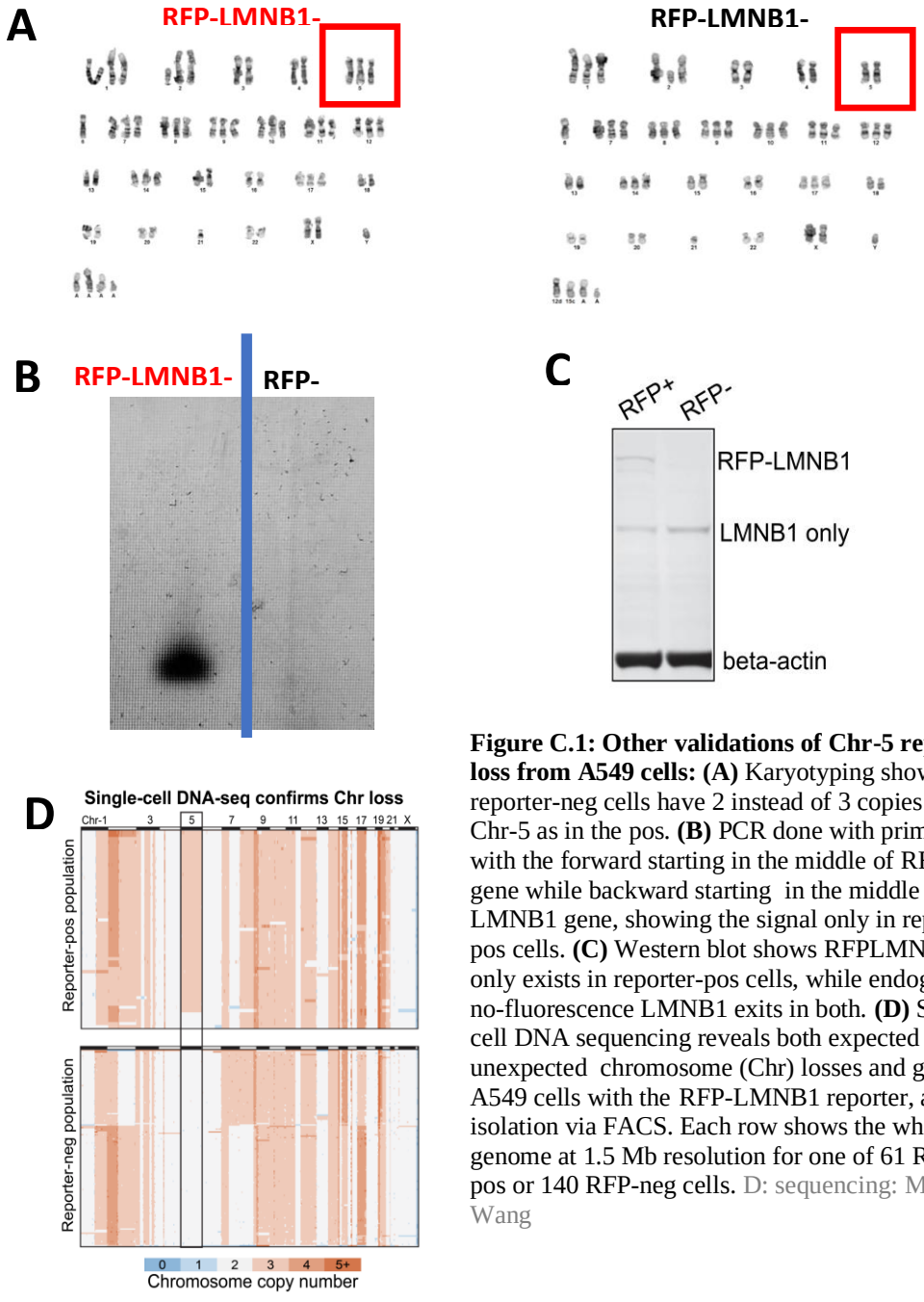

Figure C.1: Other validations of Chr-5 reporter loss from A549 cells: (A) Karyotyping shows reporter-neg cells have 2 instead of 3 copies of Chr-5 as in the pos. **(B)** PCR done with primers with the forward starting in the middle of RFP- gene while backward starting in the middle of LMNB1 gene, showing the signal only in reporter-pos cells. **(C)** Western blot shows RFPLMNB1 only exists in reporter-pos cells, while endogenous no-fluorescence LMNB1 exits in both. **(D)** Single-cell DNA sequencing reveals both expected and unexpected chromosome (Chr) losses and gains in A549 cells with the RFP-LMNB1 reporter, after isolation via FACS. Each row shows the whole genome at 1.5 Mb resolution for one of 61 RFP-pos or 140 RFP-neg cells. D: sequencing: Mai Wang

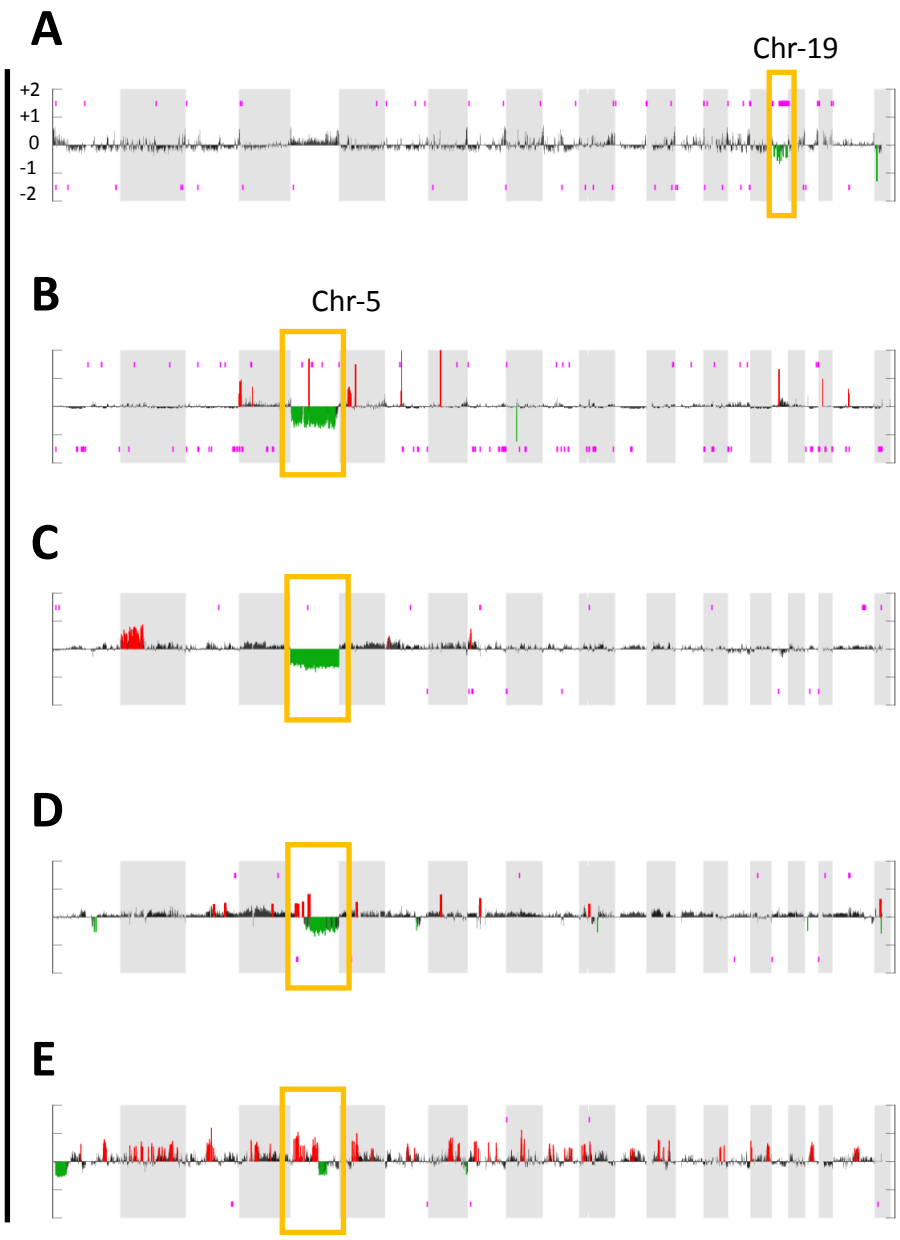

Figure C.2: SNPa validation of other cell lines and Chr-reporters. (A) iPSGFPFBL-reporter-neg. **(B)** Confinement-generated A549-Chr-5 reporter-negs. **(C)** tumor-generated A549 reporter-negs; **(D)** GFPLMNB1 reporter-negs from H23 treated with reversine. It loses q-arm of Chr-5. **(E)** GFPLMNB1 reporter-negs from U2OS cells treated with reversine. It loses part of q-arm of Chr-5, which contains the gene of LMNB1.

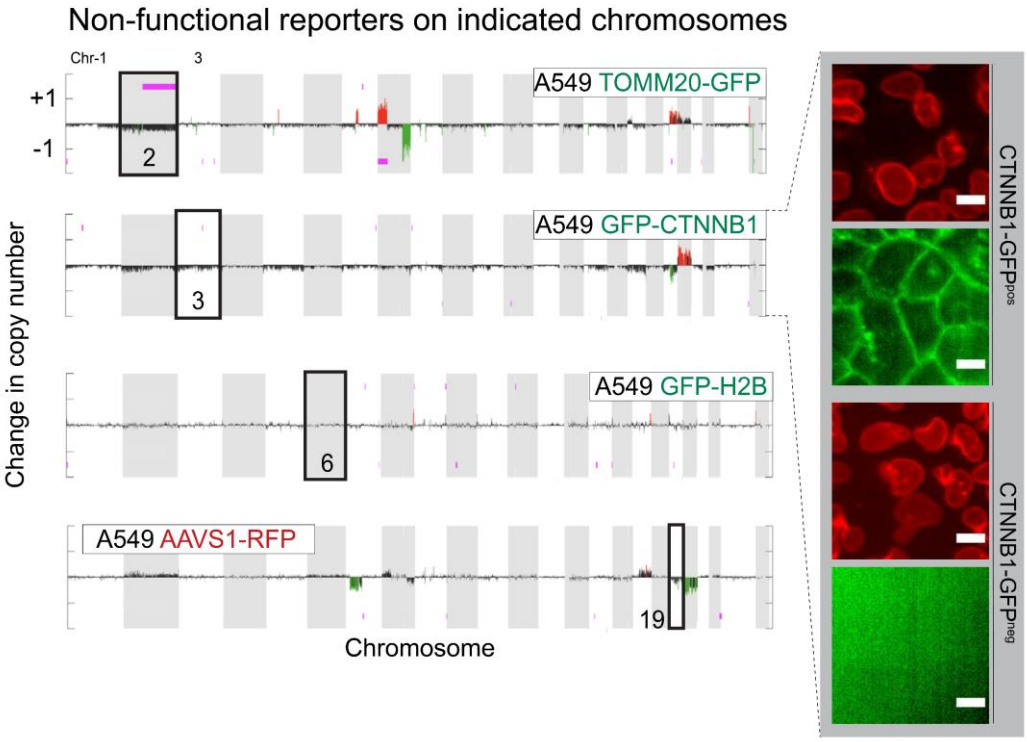

Figure C.3: SNPa examples of genes that failed Chr-reporter validation. Images show CTNNB1-GFP as an example, in which fluorescence was lost but genomic validation showed no copy number variation in the tagged chromosome between the reporter-positive and reporter-negative samples. Scalebar = 10 µm.

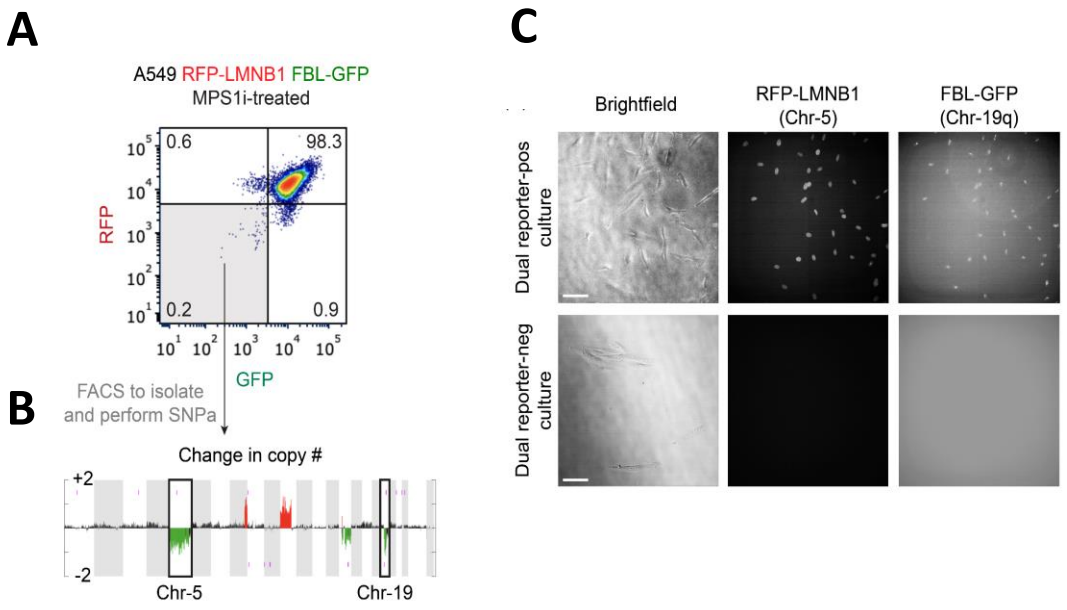

Figure C.4: Rare multi-chromosomal loss can be accurately detected using Chr-reporters.(A) A549 cells with dual-reporters on single alleles of Chr-5 (RFP-LMNB1) and Chr-19 (GFP-FBL), respectively, grown on plastic, show spontaneous loss of one or both reporters. **(B)** Double negative cells from quadrant III were sorted, expanded, and CNV was measured by subtracting from double positive SNPa. **(C)** Images of cells sorted and expanded from quadrant III (double negative) versus

Appendix D

Supplementary materials for chapter 4

Kuangzheng Zhu executed all the experiments and analyses in this supplementary chapter.

D.1 Supplementary Figures

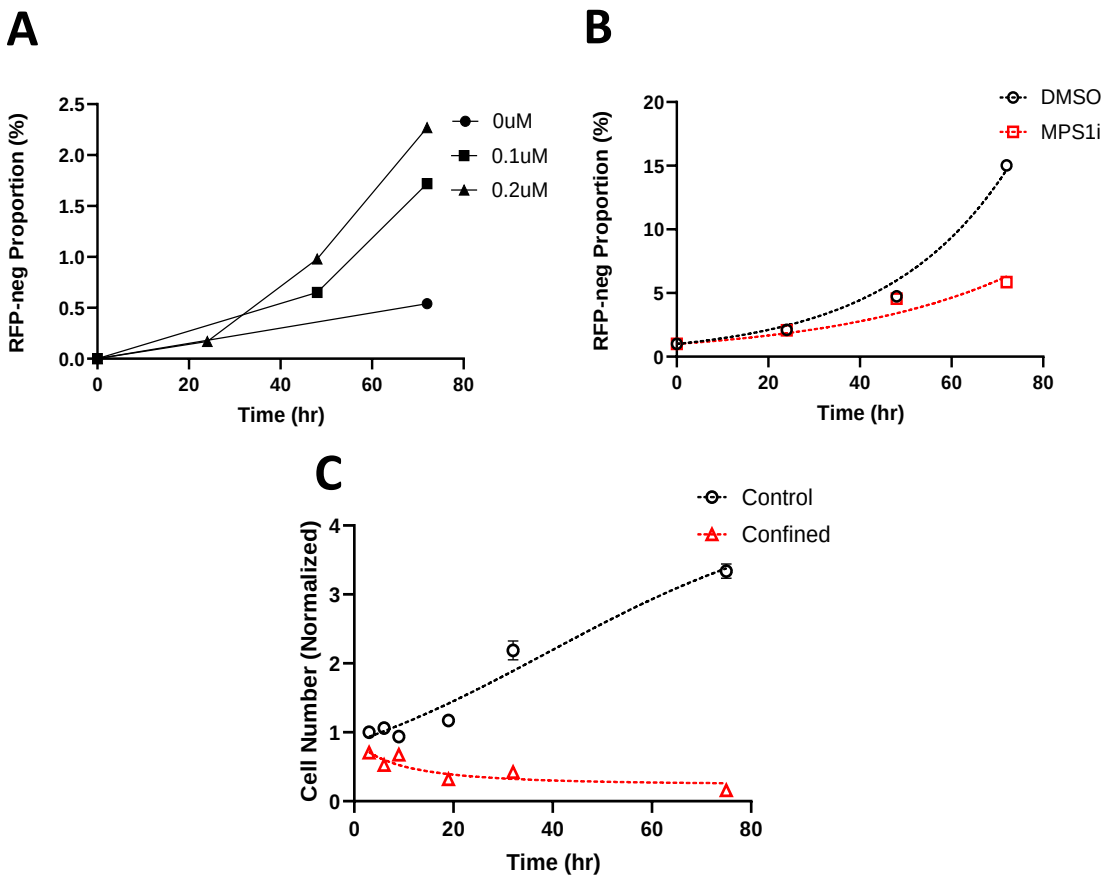

Figure D.1: High dose MPS1i (reversine) leads to more reporter-neg%; high dose MPS1i and confinement both lead to slower cell growth. (A) A549 Chr-5 reporter neg% measured at different times and different MPS1i concentrations, measured with flow cytometry. **(B)** Sustained MPS1 inhibition (0.1uM Reversine treatment without release) impedes net cell growth beyond 2 days (~2 divisions) in sparse culture. Fits are simple exponential. **(C)** Sustained confinement for 3 days suppresses proliferation and kills cells. Cells were seeded at typical semi-confluent density used for confinement, and were synchronized with nocodazole beforehand, and the measurement started after nocodazole release of the dense cultures. Mathematical fits are logistic (for control) or exponential decay (for confined), with initial time delays. Doubling Time indicated in control (19 hr) is based on the assumption of low density, or, in other words, directly calculated from the coefficient k from logistic model $y = \frac{L}{(A\,Exp\,(-k\,t+1)}$ (t is expressed in hour)

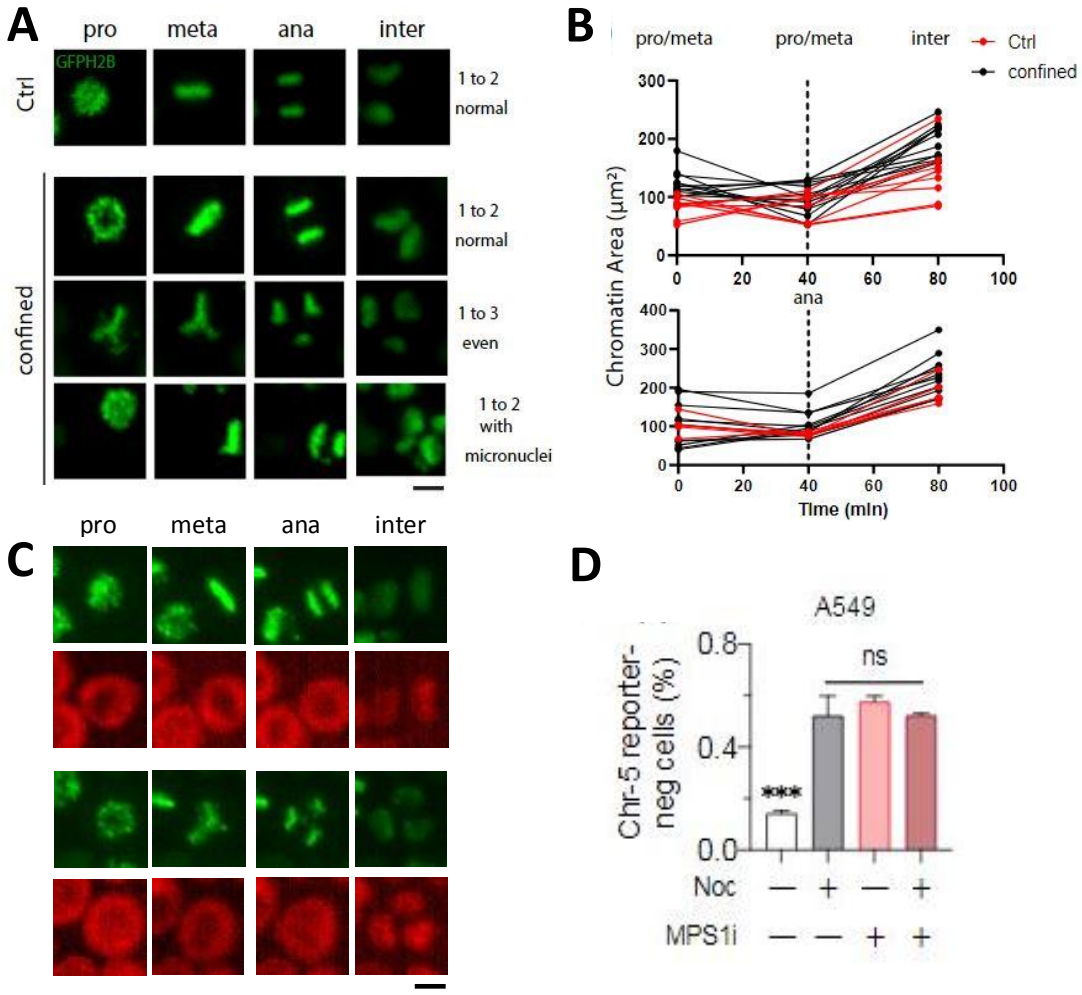
A
pro
meta
ana
inter
Ctrl
GFPH2B
1 to 2
normal
confined
1 to 2
normal
1 to 3
even
1 to 2
with
micronuclei
B
pro/meta
pro/meta
inter
Ctrl
confined
Chromatin Area (µm²)
ana
Time (min)
C
pro
meta
ana
inter
D
A549
Chr-5 reporter-
neg cells (%)
ns
***
Noc
MPS1i

Figure D.2: (Previous page) **Confinement increases chromatin area, allows cells to proceed mitosis, and doesn't provide additive effect with nocodazole when superimposed. (A)** Representative Images of GFPH2B-tagged A549 cells dividing in both unconfined and confined cases. Images in horizontal row represents the mitotic procedure of a single cell. GFP channel with H2B is displayed as DNA tracker. **(B)** Nuclear area increases after cells dividing to enter interphase, whether confinement is applied or not. Confinement enlarges nuclear areas in mitotic phases by 20%, but doesn't make a difference once cells enter interphase. **(C)** Representative images of GFP-H2B A549 cells dividing under confinement (with 6.58 μm beads). The horizontal row represents the mitotic process of a single cell. The GFP channel with H2B is used as a DNA tracker. The shape of the RFP-LMNB1 signal from the Chr-5 reporters confirms that the displayed cells enter interphase, as LMNB1 re-assembles in the end. **(D)** Sub-saturating dose of nocodazole and confinement are added, without synchronization, displaying no additive reporter-neg% as tested by flow cytometry. n=3 replicates; two-way ANOVA for multiple comparisons. ***$p < 0.0005$; ns, not significant. All Scale bars=10 μm.

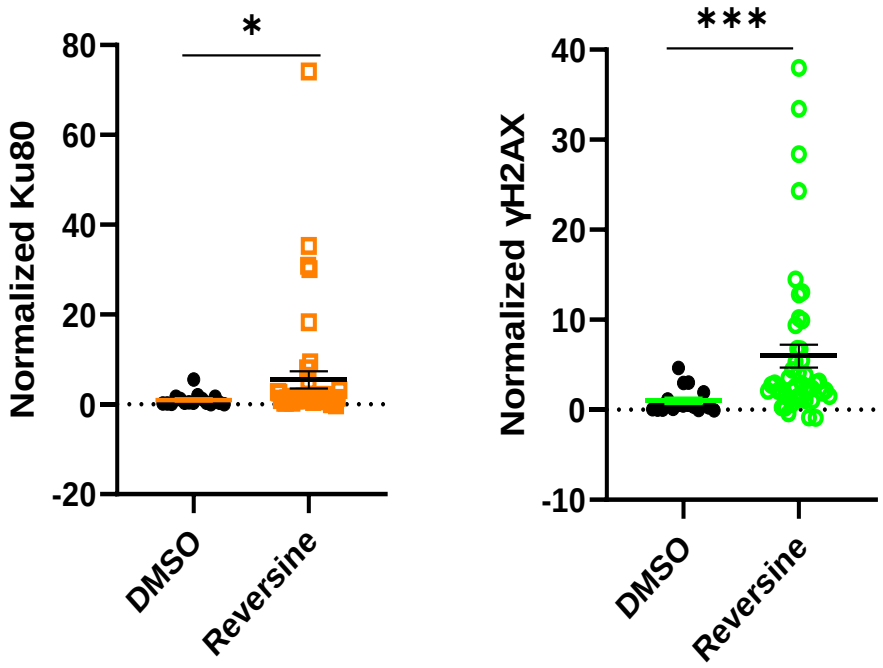

Figure D.3: MPS1 inhibitor reversine leads to more DNA damage in micronuclei. Ku80 and gH2AX intensity are both higher in reversine-treated micronuclei than DMSO, indicating higher DNA damage after MPS1 inhibition. n >20 cells per condition; unpaired two-tailed t-test with Welch's correction. *$p < 0.05$, ***$p < 0.0005$.

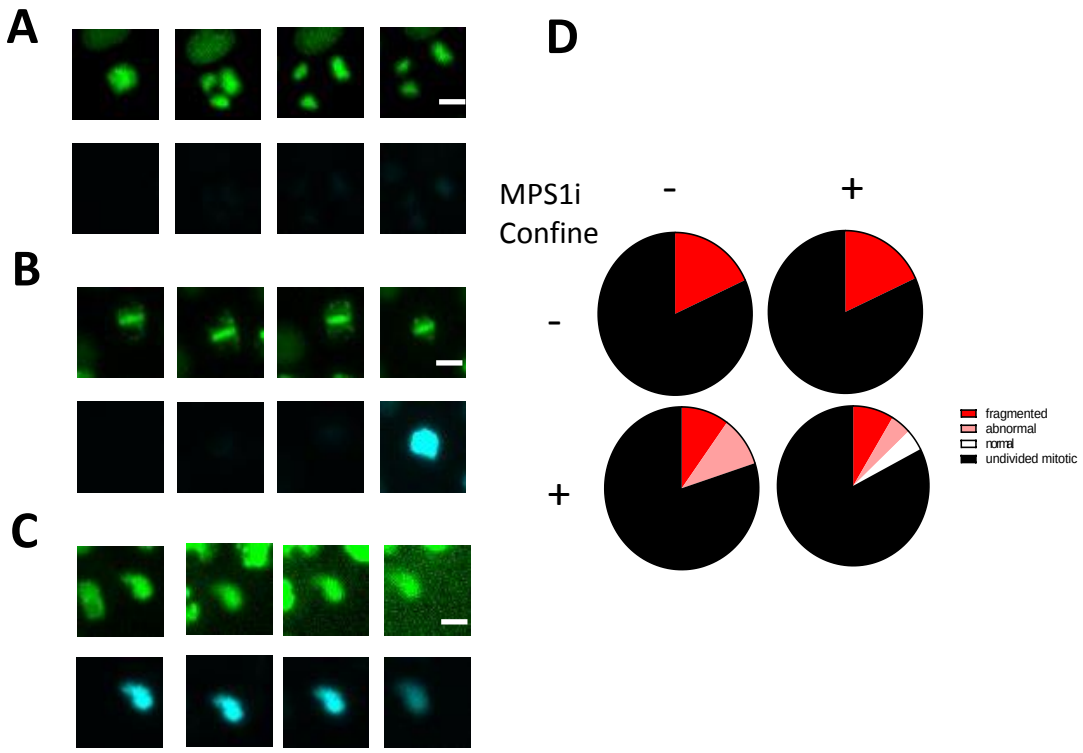

Figure D.4: Mitotic confinement causes some death in mitosis. (A-C) Representative images of GFP-H2B A549 cells dividing under confinement (with 6.58-µm beads), where tripolar division, undivided, and dead from start are presented respectively. The horizontal row represents the mitotic process of a single cell. The GFP channel with H2B is used as a DNA tracker, while DAPI was added to the culture media to stain for dead cells (or cells entering apoptosis). Images show an abnormally dividing tripolar cell that survived, an undivided cell that finally died, and a dead cell at the start of confinement (at t = 0). **(D)** Most dead cells during mitosis in confinement (with 6.58-µm beads) are undivided mitotic cells. Cells dead at the beginning of the process are excluded. All Scalebars = 10 µm.

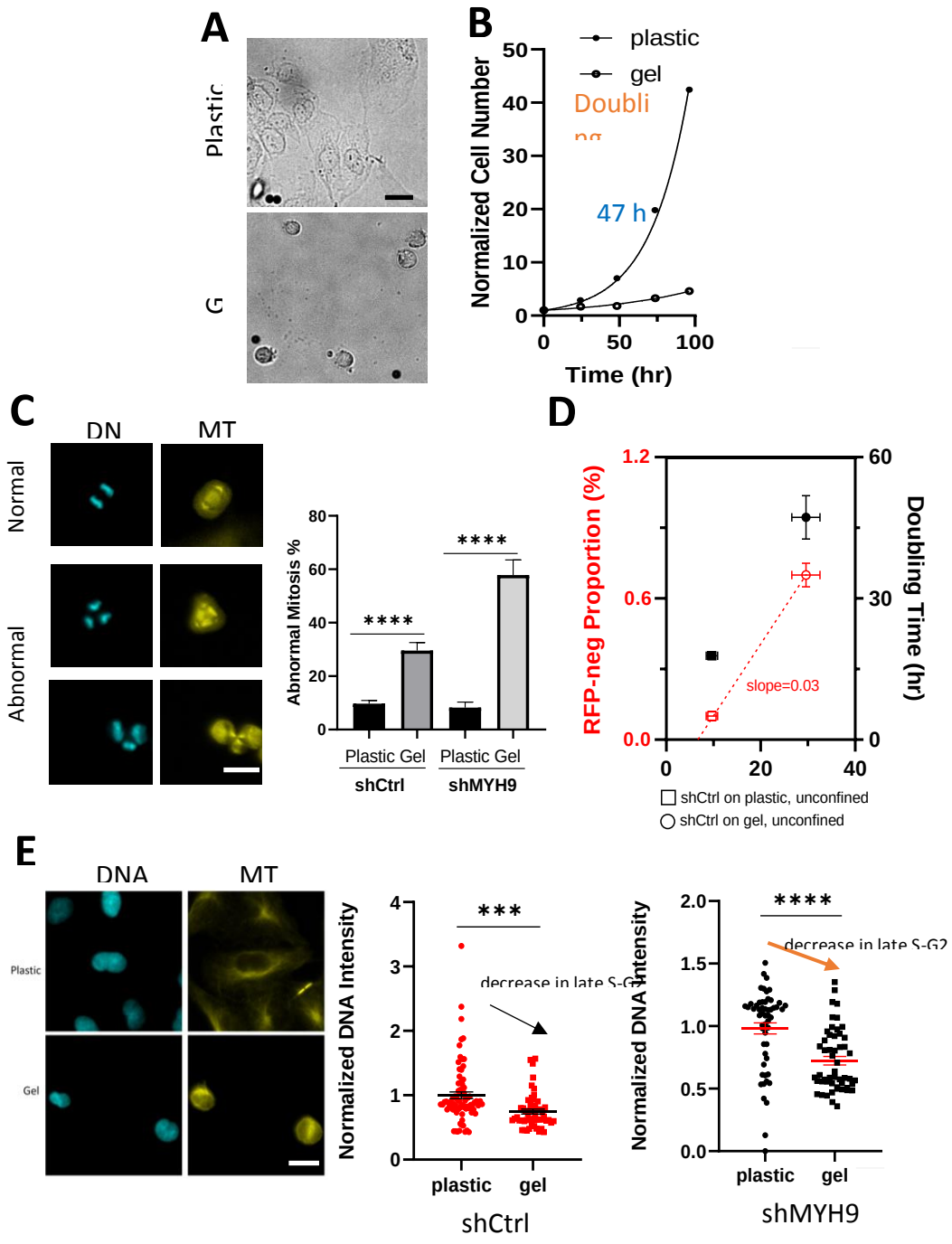
A
Plastic
G
B
plastic
gel
Doubli
ng
47 h
Normalized Cell Number
Time (hr)
C
DN
MT
Normal
Abnormal
Abnormal Mitosis %
****
****
Plastic Gel
Plastic Gel
shCtrl
shMYH9
D
RFP-neg Proportion (%)
Doubling Time (hr)
slope=0.03
shCtrl on plastic, unconfined
shCtrl on gel, unconfined
E
DNA
MT
Plastic
Gel
Normalized DNA Intensity
***
decrease in late S-G2
plastic
gel
shCtrl
****
decrease in late S-G2
plastic
gel
shMYH9

Figure D.5: (Previous page) **Myosin-IIa knockdown with collagen-coated substrate increases loss of chromosome reporter. (A)** A549 cells spread on plastic but remain round while firmly attaching on collagen-coated gel. Scale bar = 50 μm. **(B)** A549 cells plated on gel have 2.5-fold longer doubling time than on plastic. **(C)** Abnormal mitosis is more frequent on collagen-coated gel versus plastic, in both Myosin-IIa depleted cells and shCtrl cells. $n \geq 10$ cells per condition. Scale bar = 20 μm. **(D)** RFP-neg proportion and doubling times correlate with detectably abnormal mitosis. The apparent slope is consistent with 33-fold more losses.(E) DNA is low on collagen-coated gel (with a decrease in late-S/G2 cells), in both shCtrl and Myosin-IIa depleted cells. Interphase microtubule organization is altered by collagen-coated gel. $n \geq 40$ cells per condition Scale bar = 20 μm. (C) & (E): unpaired two-tailed t-test with Welch's correction: ***$p < 0.0005$; **** $p < 0.0001$.

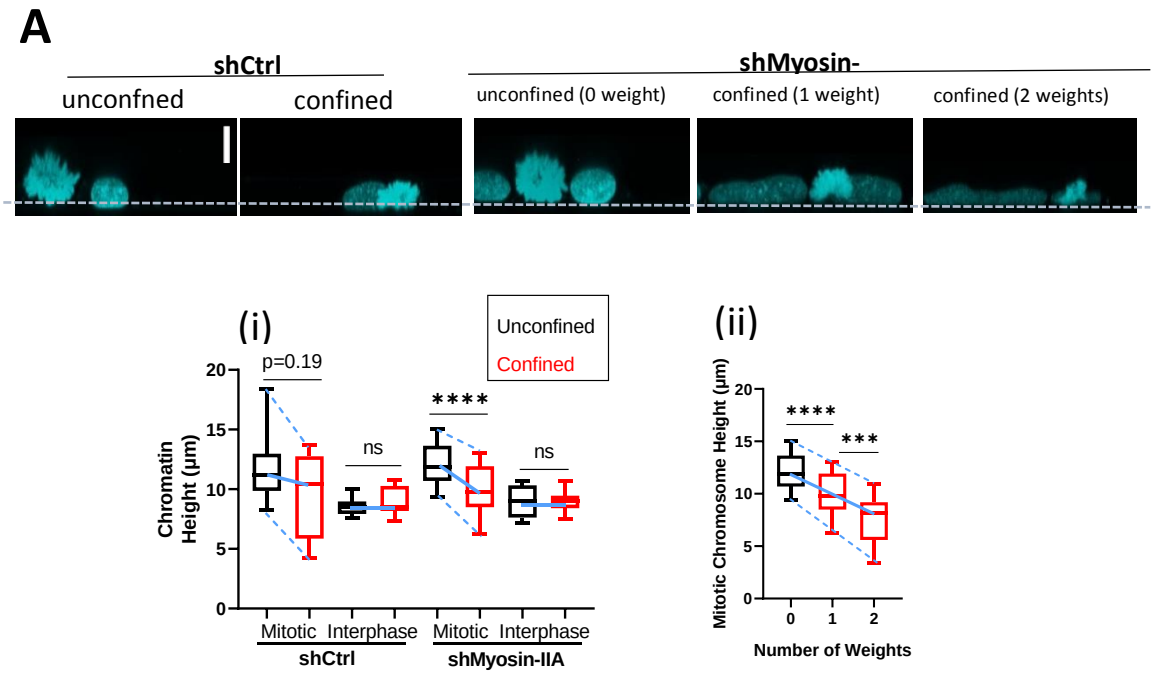
A
shCtrl
unconfned
confined
shMyosin-
unconfined (0 weight)
confined (1 weight)
confined (2 weights)
(i)
Unconfined
Confined
p=0.19
ns
****
ns
Chromatin Height (µm)
Mitotic
Interphase
Mitotic
Interphase
shCtrl
shMyosin-IIA
(ii)
****
***
Mitotic Chromosome Height (µm)
Number of Weights
B
shCtrl
shMyosin-
Unconfined
Confined
Mitotic Cell Area (µm²)
Unconfined
Confined
****
****
shCtrl
shMyosin-IIA

Figure D.6: (Previous page) **Increased weight leads to increased compression under confinement, and confinement enlarges cell area: (A)** Confinement causes mitotic height to decrease, while not affecting interphase height, whether Myosin IIa is knocked down or not. Variation is larger in mitosis than interphase, and chromatin height in both the tallest and shortest mitotic cells are compressed by confinement. Increased force causes decreased height after Myosin Iia knockdown. $n \geq 13$ cells per condition. **(B)** Decreased height corresponds to increased area, confinement causes cell area to increase. $n \geq 29$ cells per condition. (A) & (B): unpaired two-tailed t-test with Welch's correction: ***$p<0.05$, **** $p<0.0001$. scale bars = 10 μm.

D.2 Sample Calculations

Sample Calculation D.1: Derivation of reporter-neg% under perturbation or release.

Defining the density of reporter positive cells and negative cells are C_p and C_n , expressed as cell numbers/unit area of vessel surface. Both positive and negative cells undergo net proliferation with rate constants K_p and K_n , respectively. Positive cells can become negative by losing chromosome with fluorescence loss through "reaction rate constant" k_l , while negatives cannot turn back to positive, so the reaction is irreversible. Therefore, cell number balance gives differential equations:

$$\frac{dC_p}{dt} = K_p C_p - k_l C_p \quad C_p(0) = C_{p0} \quad (1)$$

$$\frac{dC_n}{dt} = K_n C_n + k_l C_p \quad C_n(0) = C_{n0} \quad (2)$$

Solving for (1), there is

$$C_p = C_{p0} e^{(K_p - k_l)t}$$

Plug in the expression of (1) for (2),

$$\frac{dC_n}{dt} - K_n C_n = k_l C_p = k_l C_{p0} e^{(K_p - k_l)t}$$

Multiply both sides with $e^{-K_n t}$, there is

$$e^{-K_n t}\frac{dC_n}{dt} - K_n e^{-K_n t} C_n = k_l C_{p0} e^{(K_p - K_n - k_l)t}$$

$$\frac{d\,(C_n e^{-K_n t})}{dt} = k_l C_{p0} e^{(K_p - K_n - k_l)t}$$

Integrate on both sides, specifying initial condition $C_n(0) = C_{n0}$

$$C_n e^{-K_n t} = \frac{k_l C_{p0} e^{(K_p - K_n - k_l)t}}{K_p - K_n - k_l} + C$$

$$C_n = \frac{k_l C_{p0} e^{(K_p - k_l)t}}{K_p - K_n - k_l} + \left(C_{n0} - \frac{k_l C_{p0}}{K_p - K_n - k_l}\right) e^{K_n t}$$

Reporter-neg cell proportion in the culture is expressed as:

$$r(t) = \frac{C_n}{C_p + C_n} = 1 - \frac{C_p}{C_p + C_n}$$

$$= 1 - \frac{C_{p0} e^{(K_p - k_l)t}}{(C_{p0} e^{(K_p - k_l)t} + \frac{k_l C_{p0} e^{(K_p - k_l)t}}{K_p - K_n - k_l} + \left(C_{n0} - \frac{k_l C_{p0}}{K_p - K_n - k_l}\right) e^{K_n t}}$$

$$= 1$$

$$- \frac{1}{1 + \frac{k_l}{K_p - K_n - k_l} + \left(\frac{C_{n0}}{C_{p0}} - \frac{k_l}{K_p - K_n - k_l}\right) Exp[-(K_p - K_n - k_l)t]}$$

Because $\frac{C_{n0}}{C_{p0}} = \frac{C_{p0}+C_{n0}}{C_{p0}} - 1 = \frac{1}{r(0)} - 1 = \frac{r(0)}{1-r(0)}$, where $r(0) = r_0$, as measured from flow cytometry , and define $\Delta K = K_p - K_n$,

$$r\,(t) = 1 - \frac{1}{1 + \frac{k_l}{\Delta K - k_l} + \left(\frac{r_0}{1-r_0} - \frac{k_l}{\Delta K - k_l}\right) Exp[-(\Delta K - k_l)t]}$$

Parameters are fitted with the expression

$$\frac{r(t)}{1-r(t)} = \frac{k_l}{\Delta K - k_l} + \left(\frac{r_0}{1-r_0} - \frac{k_l}{\Delta K - k_l}\right) Exp[-(\Delta K - k_l)t]$$

to determine parameters ΔK and k_l.

Reporter-neg% raw data were determined with flow cytometry, and were converted to absolute ratio (percentage divided by 100) before function fitting. Plotted model is displayed with 100 multiplied back.

For iPS sample, the generation phase is treated as pulse, instead of a time-dependent model as presented above.

Appendix E

Supplementary materials for chapter 5

Fig. E.1 & E.3 A have been recorded in Live cell monitoring for factors affecting genome variation, *Biorxiv*, 2018, by Xia, Y., Zhu, K., Irianto, J., Andrechak, J.C., Dooling, L.J., Pfeifer, C.R., Discher, D.E.. Kuangzheng Zhu executed all the experiments and analyses in this supplementary chapter.

E.1 Supplementary Figures

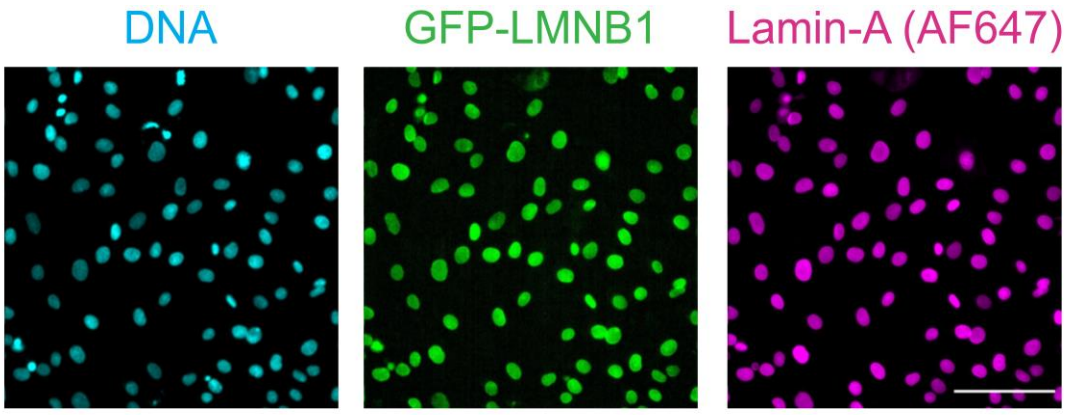

Figure E.1: iPSCs differentiate after growing *in vivo*. iPSCs dissociated from teratoma show high lamin A signal with immunofluorescence, a marker of differentiated cell. scale bar = 100 µm.

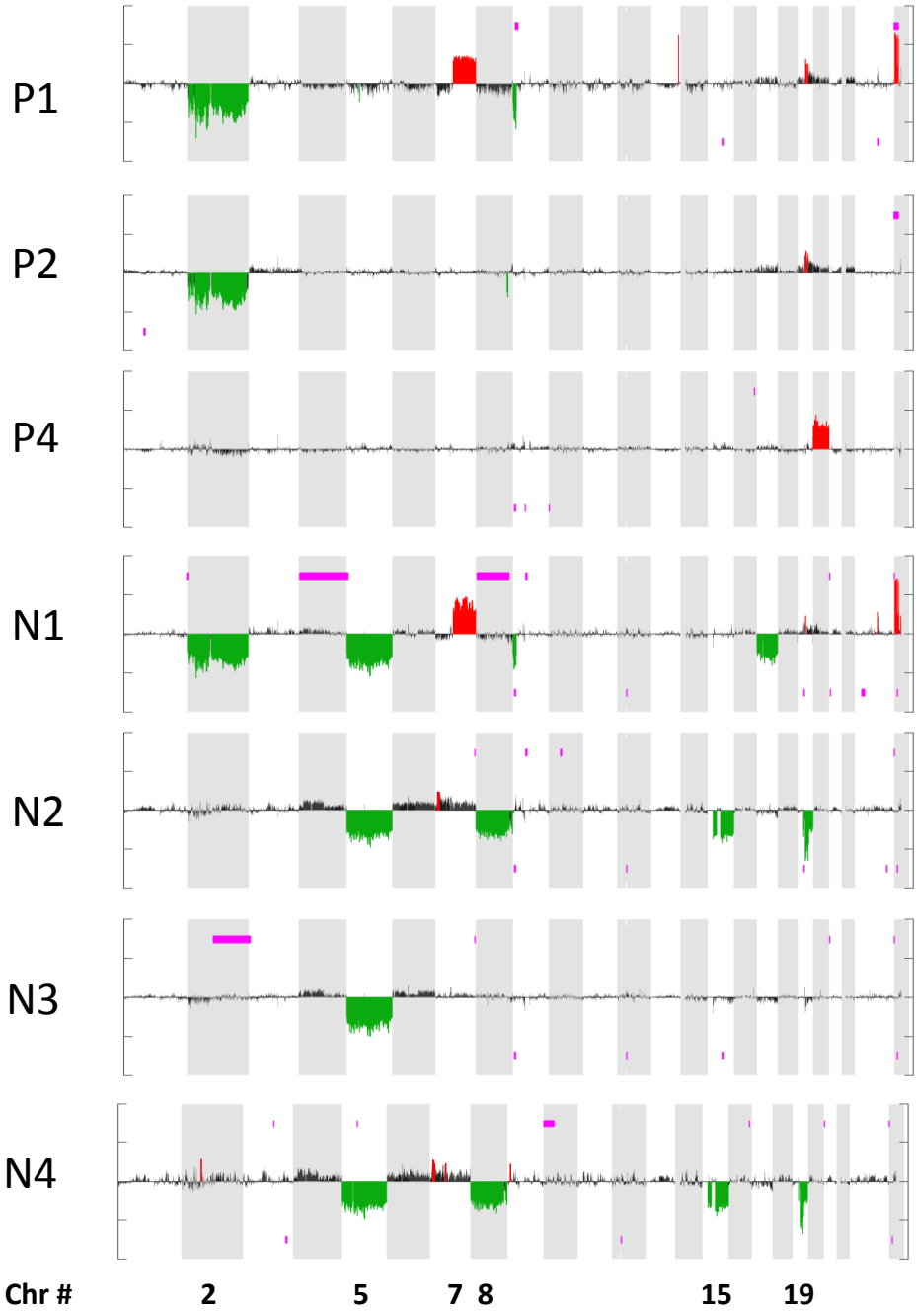

Figure E.2: SNPa of A549 clones involved in *in vivo* and phenotype studies. P1,P2,P4 and N1,N2,N3,N4 subtracted from P3, leading to a phylogeny map in Fig.5.5A.

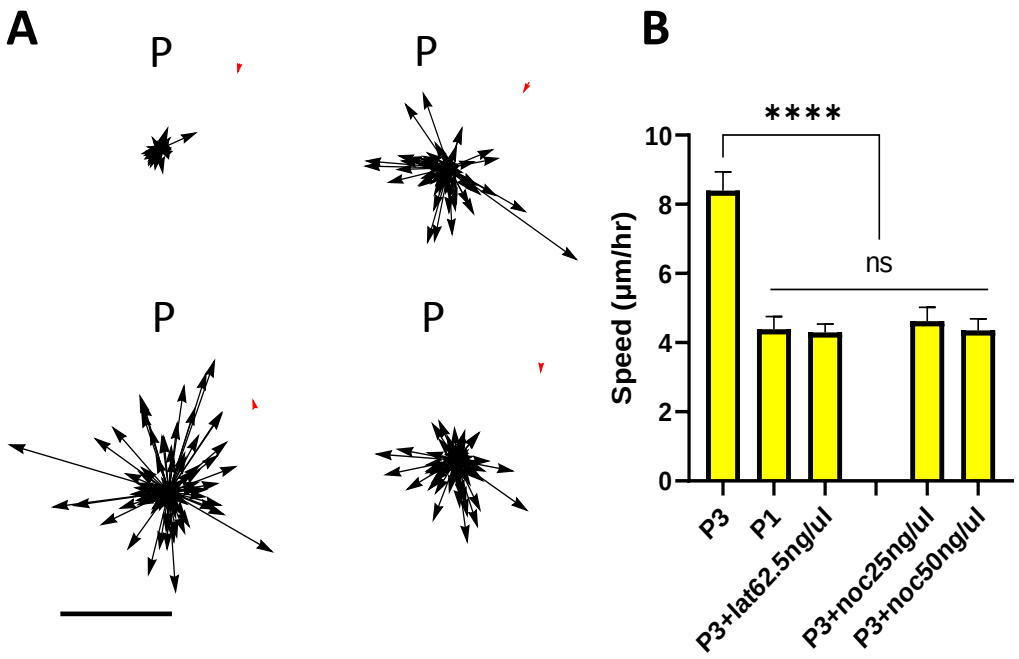

Figure E.3: Motility of genomically different clones of cells can be altered phenotypically. (A) A549 clones P1-P4 movement tracks in 6 hrs, presented by vectors. **(B)** speed of P3 movement slows down when microtubule or actin is disrupted (with nocodazole or latrunculin, respectively), and pheno-copies the behavior of P1. one-way ANOVA with Tukey's correction for multiple comparisons. ****$p < 0.0001$. scale bar = 100 µm.

References

Agol, V.I., Gmyl, A.P., 2018. Emergency Services of Viral RNAs: Repair and Remodeling. Microbiol Mol Biol Rev 82, e00067-17. https://doi.org/10.1128/MMBR.00067-17

Alberts, B., 2015. Molecular biology of the cell, Sixth edition. ed. Garland Science, Taylor and Francis Group, New York, NY.

Alshareeda, A.T., Negm, O.H., Aleskandarany, M.A., Green, A.R., Nolan, C., TigHhe, P.J., Madhusudan, S., Ellis, I.O., Rakha, E.A., 2016. Clinical and biological significance of RAD51 expression in breast cancer: a key DNA damage response protein. Breast Cancer Res Treat 159, 41–53. https://doi.org/10.1007/s10549-016-3915-8

Alvey, C., Discher, D.E., 2017. Engineering macrophages to eat cancer: from "marker of self" CD47 and phagocytosis to differentiation. J Leukoc Biol 102, 31–40. https://doi.org/10.1189/jlb.4RI1216-516R

Aragona, M., Sifrim, A., Malfait, M., Song, Y., Van Herck, J., Dekoninck, S., Gargouri, S., Lapouge, G., Swedlund, B., Dubois, C., Baatsen, P., Vints, K., Han, S., Tissir, F., Voet, T., Simons, B.D., Blanpain, C., 2020. Mechanisms of stretch-mediated skin expansion at single-cell resolution. Nature 584, 268–273. https://doi.org/10.1038/s41586-020-2555-7

Aran, D., Looney, A.P., Liu, L., Wu, E., Fong, V., Hsu, A., Chak, S., Naikawadi, R.P., Wolters, P.J., Abate, A.R., Butte, A.J., Bhattacharya, M., 2019. Reference-based analysis of lung single-cell sequencing reveals a transitional profibrotic macrophage. Nat Immunol 20, 163–172. https://doi.org/10.1038/s41590-018-0276-y

Astwood, E.B., 2014. Recent Progress in Hormone Research: Proceedings of the 1967 Laurentian Hormone Conference. Elsevier Science, Saint Louis.

Bannister, A.J., Kouzarides, T., 2011. Regulation of chromatin by histone modifications. Cell Res 21, 381–395. https://doi.org/10.1038/cr.2011.22

Benner, S.E., Wahl, G.M., Von Hoff, D.D., 1991. Double minute chromosomes and homogeneously staining regions in tumors taken directly from patients versus in human tumor cell lines. Anticancer Drugs 2, 11–25. https://doi.org/10.1097/00001813-199102000-00002

Beroukhim, R., Mermel, C.H., Porter, D., Wei, G., Raychaudhuri, S., Donovan, J., Barretina, J., Boehm, J.S., Dobson, J., Urashima, M., Mc Henry, K.T., Pinchback, R.M., Ligon, A.H., Cho, Y.-J., Haery, L., Greulich, H., Reich, M., Winckler, W., Lawrence, M.S., Weir, B.A., Tanaka, K.E., Chiang, D.Y., Bass, A.J., Loo, A., Hoffman, C., Prensner, J., Liefeld, T., Gao, Q., Yecies, D., Signoretti, S., Maher, E., Kaye, F.J., Sasaki, H., Tepper, J.E., Fletcher, J.A., Tabernero, J., Baselga, J., Tsao, M.-S., Demichelis, F., Rubin, M.A., Janne, P.A., Daly, M.J., Nucera, C., Levine,

R.L., Ebert, B.L., Gabriel, S., Rustgi, A.K., Antonescu, C.R., Ladanyi, M., Letai, A., Garraway, L.A., Loda, M., Beer, D.G., True, L.D., Okamoto, A., Pomeroy, S.L., Singer, S., Golub, T.R., Lander, E.S., Getz, G., Sellers, W.R., Meyerson, M., 2010. The landscape of somatic copy-number alteration across human cancers. Nature 463, 899–905. https://doi.org/10.1038/nature08822

Bittel, D.C., Butler, M.G., 2005. Prader-Willi syndrome: clinical genetics, cytogenetics and molecular biology. Expert Rev Mol Med 7, 1–20. https://doi.org/10.1017/S1462399405009531

Bonnans, C., Chou, J., Werb, Z., 2014. Remodelling the extracellular matrix in development and disease. Nat Rev Mol Cell Biol 15, 786–801. https://doi.org/10.1038/nrm3904

Boulton, S.J., 2006. Cellular functions of the BRCA tumour-suppressor proteins. Biochem Soc Trans 34, 633–645. https://doi.org/10.1042/BST0340633

Boulton, S.J., Jackson, S.P., 1998. Components of the Ku-dependent non-homologous end-joining pathway are involved in telomeric length maintenance and telomeric silencing. EMBO J 17, 1819–1828. https://doi.org/10.1093/emboj/17.6.1819

Boyd, R.S., Ray, K.P., Wallis, M., 1988. Actions of pertussis toxin on the inhibitory effects of dopamine and somatostatin on prolactin and growth hormone release from ovine anterior pituitary cells. J Mol Endocrinol 1, 179–186. https://doi.org/10.1677/jme.0.0010179

Cadart, C., Zlotek-Zlotkiewicz, E., Le Berre, M., Piel, M., Matthews, H.K., 2014. Exploring the function of cell shape and size during mitosis. Dev Cell 29, 159–169. https://doi.org/10.1016/j.devcel.2014.04.009

Capo-chichi, C.D., Cai, K.Q., Smedberg, J., Ganjei-Azar, P., Godwin, A.K., Xu, X.-X., 2011. Loss of A-type lamin expression compromises nuclear envelope integrity in breast cancer. Chin J Cancer 30, 415–425. https://doi.org/10.5732/cjc.010.10566

Castedo, M., Perfettini, J.-L., Roumier, T., Andreau, K., Medema, R., Kroemer, G., 2004. Cell death by mitotic catastrophe: a molecular definition. Oncogene 23, 2825–2837. https://doi.org/10.1038/sj.onc.1207528

Castera, L., Friedrich-Rust, M., Loomba, R., 2019. Noninvasive Assessment of Liver Disease in Patients With Nonalcoholic Fatty Liver Disease. Gastroenterology 156, 1264-1281.e4. https://doi.org/10.1053/j.gastro.2018.12.036

Chen, B., Deng, S., Ge, T., Ye, M., Yu, J., Lin, S., Ma, W., Songyang, Z., 2020. Live cell imaging and proteomic profiling of endogenous NEAT1 lncRNA by CRISPR/Cas9-mediated knock-in. Protein Cell 11, 641–660. https://doi.org/10.1007/s13238-020-00706-w

Chen, R., Wold, M.S., 2014. Replication protein A: single-stranded DNA's first responder: dynamic DNA-interactions allow replication protein A to direct single-strand DNA intermediates into different pathways for synthesis or repair. Bioessays 36, 1156–1161. https://doi.org/10.1002/bies.201400107

Christmann, M., Kaina, B., 2000. Nuclear translocation of mismatch repair proteins MSH2 and MSH6 as a response of cells to alkylating agents. J Biol Chem 275, 36256–36262. https://doi.org/10.1074/jbc.M005377200

Chung, W., Jo, C., Chung, W.J., Kim, D.J., 2018. Liver cirrhosis and cancer: comparison of mortality. Hepatol Int 12, 269–276. https://doi.org/10.1007/s12072-018-9850-5

Coaxum, S.D., Tiedeken, J., Garrett-Mayer, E., Myers, J., Rosenzweig, S.A., Neskey, D.M., 2017. The tumor suppressor capability of p53 is dependent on non-muscle myosin IIA function in head and neck cancer. Oncotarget 8, 22991–23007. https://doi.org/10.18632/oncotarget.14967

Compression regulates mitotic spindle length by a mechanochemical switch at the poles, n.d.

Conti, M.A., Saleh, A.D., Brinster, L.R., Cheng, H., Chen, Z., Cornelius, S., Liu, C., Ma, X., Van Waes, C., Adelstein, R.S., 2015. Conditional deletion of nonmuscle myosin II-A in mouse tongue epithelium results in squamous cell carcinoma. Sci Rep 5, 14068. https://doi.org/10.1038/srep14068

Cossarizza, A., Chang, H.-D., Radbruch, A., Akdis, M., Andrä, I., Annunziato, F., Bacher, P., Barnaba, V., Battistini, L., Bauer, W.M., Baumgart, S., Becher, B., Beisker, W., Berek, C., Blanco, A., Borsellino, G., Boulais, P.E., Brinkman, R.R., Büscher, M., Busch, D.H., Bushnell, T.P., Cao, X., Cavani, A., Chattopadhyay, P.K., Cheng, Q., Chow, S., Clerici, M., Cooke, A., Cosma, A., Cosmi, L., Cumano, A., Dang, V.D., Davies, D., De Biasi, S., Del Zotto, G., Della Bella, S., Dellabona, P., Deniz, G., Dessing, M., Diefenbach, A., Di Santo, J., Dieli, F., Dolf, A., Donnenberg, V.S., Dörner, T., Ehrhardt, G.R.A., Endl, E., Engel, P., Engelhardt, B., Esser, C., Everts, B., Dreher, A., Falk, C.S., Fehniger, T.A., Filby, A., Fillatreau, S., Follo, M., Förster, I., Foster, J., Foulds, G.A., Frenette, P.S., Galbraith, D., Garbi, N., García-Godoy, M.D., Geginat, J., Ghoreschi, K., Gibellini, L., Goettlinger, C., Goodyear, C.S., Gori, A., Grogan, J., Gross, M., Grützkau, A., Grummitt, D., Hahn, J., Hammer, Q., Hauser, A.E., Haviland, D.L., Hedley, D., Herrera, G., Herrmann, M., Hiepe, F., Holland, T., Hombrink, P., Houston, J.P., Hoyer, B.F., Huang, B., Hunter, C.A., Iannone, A., Jäck, H.-M., Jávega, B., Jonjic, S., Juelke, K., Jung, S., Kaiser, T., Kalina, T., Keller, B., Khan, S., Kienhöfer, D., Kroneis, T., Kunkel, D., Kurts, C., Kvistborg, P., Lannigan, J., Lantz, O., Larbi, A., LeibundGut-Landmann, S., Leipold, M.D., Levings, M.K., Litwin, V., Liu, Y., Lohoff, M., Lombardi, G., Lopez, L., Lovett-Racke, A., Lubberts, E., Ludewig, B., Lugli, E., Maecker, H.T., Martrus, G., Matarese, G., Maueröder, C., McGrath, M., McInnes, I., Mei, H.E., Melchers, F., Melzer, S., Mielenz, D., Mills, K., Mirrer, D., Mjösberg, J., Moore, J., Moran, B., Moretta, A., Moretta, L., Mosmann, T.R., Müller, S., Müller, W., Münz, C., Multhoff, G., Munoz, L.E., Murphy, K.M., Nakayama, T., Nasi, M., Neudörfl, C., Nolan, J., Nourshargh, S., O'Connor, J.-E., Ouyang, W., Oxenius, A., Palankar, R., Panse, I., Peterson, P., Peth, C., Petriz, J., Philips, D., Pickl, W., Piconese, S., Pinti, M., Pockley, A.G., Podolska, M.J., Pucillo, C., Quataert, S.A., Radstake,

T.R.D.J., Rajwa, B., Rebhahn, J.A., Recktenwald, D., Remmerswaal, E.B.M., Rezvani, K., Rico, L.G., Robinson, J.P., Romagnani, C., Rubartelli, A., Ruckert, B., Ruland, J., Sakaguchi, S., Sala-de-Oyanguren, F., Samstag, Y., Sanderson, S., Sawitzki, B., Scheffold, A., Schiemann, M., Schildberg, F., Schimisky, E., Schmid, S.A., Schmitt, S., Schober, K., Schüler, T., Schulz, A.R., Schumacher, T., Scotta, C., Shankey, T.V., Shemer, A., Simon, A.-K., Spidlen, J., Stall, A.M., Stark, R., Stehle, C., Stein, M., Steinmetz, T., Stockinger, H., Takahama, Y., Tarnok, A., Tian, Z., Toldi, G., Tornack, J., Traggiai, E., Trotter, J., Ulrich, H., van der Braber, M., van Lier, R.A.W., Veldhoen, M., Vento-Asturias, S., Vieira, P., Voehringer, D., Volk, H.-D., von Volkmann, K., Waisman, A., Walker, R., Ward, M.D., Warnatz, K., Warth, S., Watson, J.V., Watzl, C., Wegener, L., Wiedemann, A., Wienands, J., Willimsky, G., Wing, J., Wurst, P., Yu, L., Yue, A., Zhang, Q., Zhao, Y., Ziegler, S., Zimmermann, J., 2017. Guidelines for the use of flow cytometry and cell sorting in immunological studies. Eur J Immunol 47, 1584–1797. https://doi.org/10.1002/eji.201646632

Cunningham, J.J., Ulbright, T.M., Pera, M.F., Looijenga, L.H.J., 2012. Lessons from human teratomas to guide development of safe stem cell therapies. Nat Biotechnol 30, 849–857. https://doi.org/10.1038/nbt.2329

Darzynkiewicz, Z., Halicka, H.D., Zhao, H., Podhorecka, M., 2011. Cell synchronization by inhibitors of DNA replication induces replication stress and DNA damage response: analysis by flow cytometry. Methods Mol Biol 761, 85–96. https://doi.org/10.1007/978-1-61779-182-6_6

Davoli, T., Xu, A.W., Mengwasser, K.E., Sack, L.M., Yoon, J.C., Park, P.J., Elledge, S.J., 2013. Cumulative haploinsufficiency and triplosensitivity drive aneuploidy patterns and shape the cancer genome. Cell 155, 948–962. https://doi.org/10.1016/j.cell.2013.10.011

de la Rosa, J., Freije, J.M.P., Cabanillas, R., Osorio, F.G., Fraga, M.F., Fernández-García, M.S., Rad, R., Fanjul, V., Ugalde, A.P., Liang, Q., Prosser, H.M., Bradley, A., Cadiñanos, J., López-Otín, C., 2013. Prelamin A causes progeria through cell-extrinsic mechanisms and prevents cancer invasion. Nat Commun 4, 2268. https://doi.org/10.1038/ncomms3268

de Wind, N., Dekker, M., Berns, A., Radman, M., te Riele, H., 1995. Inactivation of the mouse Msh2 gene results in mismatch repair deficiency, methylation tolerance, hyperrecombination, and predisposition to cancer. Cell 82, 321–330. https://doi.org/10.1016/0092-8674(95)90319-4

Denais, C.M., Gilbert, R.M., Isermann, P., McGregor, A.L., te Lindert, M., Weigelin, B., Davidson, P.M., Friedl, P., Wolf, K., Lammerding, J., 2016. Nuclear envelope rupture and repair during cancer cell migration. Science 352, 353–358. https://doi.org/10.1126/science.aad7297

Deville, S.S., Cordes, N., 2019. The Extracellular, Cellular, and Nuclear Stiffness, a Trinity in the Cancer Resistome-A Review. Front Oncol 9, 1376. https://doi.org/10.3389/fonc.2019.01376

Difilippantonio, M.J., Zhu, J., Chen, H.T., Meffre, E., Nussenzweig, M.C., Max, E.E., Ried, T., Nussenzweig, A., 2000. DNA repair protein Ku80 suppresses chromosomal aberrations and malignant transformation. Nature 404, 510–514. https://doi.org/10.1038/35006670

Doller, A., Badawi, A., Schmid, T., Brauss, T., Pleli, T., zu Heringdorf, D.M., Piiper, A., Pfeilschifter, J., Eberhardt, W., 2015. The cytoskeletal inhibitors latrunculin A and blebbistatin exert antitumorigenic properties in human hepatocellular carcinoma cells by interfering with intracellular HuR trafficking. Exp Cell Res 330, 66–80. https://doi.org/10.1016/j.yexcr.2014.09.010

Dooley, J., Lok, A.S.F., Garcia-Tsao, G., Pinzani, M. (Eds.), 2018. Sherlock's diseases of the liver and biliary system, 13th edition. ed. Wiley, Hoboken, NJ.

Drake, J.W., Charlesworth, B., Charlesworth, D., Crow, J.F., 1998. Rates of spontaneous mutation. Genetics 148, 1667–1686. https://doi.org/10.1093/genetics/148.4.1667

Driscoll, D.A., Gross, S., 2009. Clinical practice. Prenatal screening for aneuploidy. N Engl J Med 360, 2556–2562. https://doi.org/10.1056/NEJMcp0900134

Duijf, P.H.G., Schultz, N., Benezra, R., 2013. Cancer cells preferentially lose small chromosomes. Int J Cancer 132, 2316–2326. https://doi.org/10.1002/ijc.27924

Dumont, S., Mitchison, T.J., 2009. Compression regulates mitotic spindle length by a mechanochemical switch at the poles. Curr Biol 19, 1086–1095. https://doi.org/10.1016/j.cub.2009.05.056

Duncan, J.A., Reeves, J.R., Cooke, T.G., 1998. BRCA1 and BRCA2 proteins: roles in health and disease. Mol Pathol 51, 237–247. https://doi.org/10.1136/mp.51.5.237

Eble, J.A., Niland, S., 2019. The extracellular matrix in tumor progression and metastasis. Clin Exp Metastasis 36, 171–198. https://doi.org/10.1007/s10585-019-09966-1

Engler, A., Bacakova, L., Newman, C., Hategan, A., Griffin, M., Discher, D., 2004. Substrate compliance versus ligand density in cell on gel responses. Biophys J 86, 617–628. https://doi.org/10.1016/S0006-3495(04)74140-5

Engler, A.J., Sen, S., Sweeney, H.L., Discher, D.E., 2006. Matrix elasticity directs stem cell lineage specification. Cell 126, 677–689. https://doi.org/10.1016/j.cell.2006.06.044

Farr, C.J., Antoniou-Kourounioti, M., Mimmack, M.L., Volkov, A., Porter, A.C.G., 2014. The α isoform of topoisomerase II is required for hypercompaction of mitotic chromosomes in human cells. Nucleic Acids Res 42, 4414–4426. https://doi.org/10.1093/nar/gku076

Farrell, G.C., Larter, C.Z., 2006. Nonalcoholic fatty liver disease: from steatosis to cirrhosis. Hepatology 43, S99–S112. https://doi.org/10.1002/hep.20973

Fattet, L., Jung, H.-Y., Matsumoto, M.W., Aubol, B.E., Kumar, A., Adams, J.A., Chen, A.C., Sah, R.L., Engler, A.J., Pasquale, E.B., Yang, J., 2020. Matrix Rigidity Controls Epithelial-Mesenchymal Plasticity and Tumor Metastasis via a Mechanoresponsive EPHA2/LYN Complex. Dev Cell 54, 302-316.e7. https://doi.org/10.1016/j.devcel.2020.05.031

Favier, R., Akshoomoff, N., Mattson, S., Grossfeld, P., 2015. Jacobsen syndrome: Advances in our knowledge of phenotype and genotype. Am J Med Genet C Semin Med Genet 169, 239–250. https://doi.org/10.1002/ajmg.c.31448

Fournier, P.-E., Raoult, D., 2017. Bacterial Genomes, in: Infectious Diseases. Elsevier, pp. 62-67.e1. https://doi.org/10.1016/B978-0-7020-6285-8.00007-1

Friedenson, B., 2007. The BRCA1/2 pathway prevents hematologic cancers in addition to breast and ovarian cancers. BMC Cancer 7, 152. https://doi.org/10.1186/1471-2407-7-152

GBD 2013 Mortality and Causes of Death Collaborators, 2015. Global, regional, and national age-sex specific all-cause and cause-specific mortality for 240 causes of death, 1990-2013: a systematic analysis for the Global Burden of Disease Study 2013. Lancet 385, 117–171. https://doi.org/10.1016/S0140-6736(14)61682-2

Gemble, S., Buhagiar-Labarchède, G., Onclercq-Delic, R., Fontaine, G., Lambert, S., Amor-Guéret, M., 2020. Topoisomerase IIα prevents ultrafine anaphase bridges by two mechanisms. Open Biol 10, 190259. https://doi.org/10.1098/rsob.190259

Girstun, A., Ishikawa, T., Kowalska-Loth, B., Czubaty, A., Staron, K., 2017. Subnuclear Localization of Human Topoisomerase I. J Cell Biochem 118, 407–419. https://doi.org/10.1002/jcb.25654

Greaves, M., Maley, C.C., 2012. Clonal evolution in cancer. Nature 481, 306–313. https://doi.org/10.1038/nature10762

Griffiths, A.J.F., 2005. Introduction to genetic analysis. W.H. Freeman and Co., New York.

Gunther, D.F., Eugster, E., Zagar, A.J., Bryant, C.G., Davenport, M.L., Quigley, C.A., 2004. Ascertainment bias in Turner syndrome: new insights from girls who were diagnosed incidentally in prenatal life. Pediatrics 114, 640–644. https://doi.org/10.1542/peds.2003-1122-L

Guntur, V.P., Waldrep, J.C., Guo, J.J., Selting, K., Dhand, R., 2010. Increasing p53 protein sensitizes non-small cell lung cancer to paclitaxel and cisplatin in vitro. Anticancer Res 30, 3557–3564.

Guo, X.E., Ngo, B., Modrek, A.S., Lee, W.-H., 2014. Targeting tumor suppressor networks for cancer therapeutics. Curr Drug Targets 15, 2–16. https://doi.org/10.2174/1389450114666140106095151

Gutierrez-Aranda, I., Ramos-Mejia, V., Bueno, C., Munoz-Lopez, M., Real, P.J., Mácia, A., Sanchez, L., Ligero, G., Garcia-Parez, J.L., Menendez, P., 2010. Human induced pluripotent stem cells develop teratoma more efficiently and faster than human

embryonic stem cells regardless the site of injection. Stem Cells 28, 1568–1570. https://doi.org/10.1002/stem.471

Han, K., Pierce, S.E., Li, A., Spees, K., Anderson, G.R., Seoane, J.A., Lo, Y.-H., Dubreuil, M., Olivas, M., Kamber, R.A., Wainberg, M., Kostyrko, K., Kelly, M.R., Yousefi, M., Simpkins, S.W., Yao, D., Lee, K., Kuo, C.J., Jackson, P.K., Sweet-Cordero, A., Kundaje, A., Gentles, A.J., Curtis, C., Winslow, M.M., Bassik, M.C., 2020. CRISPR screens in cancer spheroids identify 3D growth-specific vulnerabilities. Nature 580, 136–141. https://doi.org/10.1038/s41586-020-2099-x

Harada, T., Swift, J., Irianto, J., Shin, J.-W., Spinler, K.R., Athirasala, A., Diegmiller, R., Dingal, P.C.D.P., Ivanovska, I.L., Discher, D.E., 2014. Nuclear lamin stiffness is a barrier to 3D migration, but softness can limit survival. J Cell Biol 204, 669–682. https://doi.org/10.1083/jcb.201308029

Hassold, T., Hunt, P., 2001. To err (meiotically) is human: the genesis of human aneuploidy. Nat Rev Genet 2, 280–291. https://doi.org/10.1038/35066065

Hatch, E.M., Fischer, A.H., Deerinck, T.J., Hetzer, M.W., 2013. Catastrophic nuclear envelope collapse in cancer cell micronuclei. Cell 154, 47–60. https://doi.org/10.1016/j.cell.2013.06.007

Hayashida, M., Maita, T., Matsuda, G., 1991. The primary structure of skeletal muscle myosin heavy chain: I. Sequence of the amino-terminal 23 kDa fragment. J Biochem 110, 54–59. https://doi.org/10.1093/oxfordjournals.jbchem.a123543

Holt, J.A., 1979. The cause of cancer: biochemical defects in the cancer cell demonstrated by the effects of electromagnetic radiation, glucose and oxygen. Med Hypotheses 5, 109–143. https://doi.org/10.1016/0306-9877(79)90065-3

Hu, X., Weston, T.A., He, C., Jung, R.S., Heizer, P.J., Young, B.D., Tu, Y., Tontonoz, P., Wohlschlegel, J.A., Jiang, H., Young, S.G., Fong, L.G., 2019. Release of cholesterol-rich particles from the macrophage plasma membrane during movement of filopodia and lamellipodia. Elife 8, e50231. https://doi.org/10.7554/eLife.50231

Iourov, I.Y., Vorsanova, S.G., Yurov, Y.B., Kutsev, S.I., 2019. Ontogenetic and Pathogenetic Views on Somatic Chromosomal Mosaicism. Genes (Basel) 10, E379. https://doi.org/10.3390/genes10050379

Iredale, J.P., 2003. Cirrhosis: new research provides a basis for rational and targeted treatments. BMJ 327, 143–147. https://doi.org/10.1136/bmj.327.7407.143

Irianto, J., Xia, Y., Pfeifer, C.R., Athirasala, A., Ji, J., Alvey, C., Tewari, M., Bennett, R.R., Harding, S.M., Liu, A.J., Greenberg, R.A., Discher, D.E., 2017. DNA Damage Follows Repair Factor Depletion and Portends Genome Variation in Cancer Cells after Pore Migration. Curr Biol 27, 210–223. https://doi.org/10.1016/j.cub.2016.11.049

Iwabuchi, K., Bartel, P.L., Li, B., Marraccino, R., Fields, S., 1994. Two cellular proteins that bind to wild-type but not mutant p53. Proc Natl Acad Sci U S A 91, 6098–6102. https://doi.org/10.1073/pnas.91.13.6098

Iwabuchi, K., Li, B., Massa, H.F., Trask, B.J., Date, T., Fields, S., 1998. Stimulation of p53-mediated transcriptional activation by the p53-binding proteins, 53BP1 and 53BP2. J Biol Chem 273, 26061–26068. https://doi.org/10.1074/jbc.273.40.26061

Jackson, H.W., Defamie, V., Waterhouse, P., Khokha, R., 2017. TIMPs: versatile extracellular regulators in cancer. Nat Rev Cancer 17, 38–53. https://doi.org/10.1038/nrc.2016.115

Jiang, H., Gelhaus, S.L., Mangal, D., Harvey, R.G., Blair, I.A., Penning, T.M., 2007. Metabolism of benzo[a]pyrene in human bronchoalveolar H358 cells using liquid chromatography-mass spectrometry. Chem Res Toxicol 20, 1331–1341. https://doi.org/10.1021/tx700107z

Jin, Y., Sun, A., Noriki, S., Imamura, Y., Fukuda, M., 2007. Detection of cancer clones in human colorectal adenoma as revealed by increased DNA instability and other biomarkers. Eur J Histochem 51, 1–10.

Joo, E.E., Yamada, K.M., 2014. MYPT1 regulates contractility and microtubule acetylation to modulate integrin adhesions and matrix assembly. Nat Commun 5, 3510. https://doi.org/10.1038/ncomms4510

Kakarougkas, A., Jeggo, P.A., 2014. DNA DSB repair pathway choice: an orchestrated handover mechanism. Br J Radiol 87, 20130685. https://doi.org/10.1259/bjr.20130685

Kapoor, T.M., 2017. Metaphase Spindle Assembly. Biology (Basel) 6, E8. https://doi.org/10.3390/biology6010008

Klinefelter, H.F., 1986. Klinefelter's syndrome: historical background and development. South Med J 79, 1089–1093.

Knouse, K.A., Lopez, K.E., Bachofner, M., Amon, A., 2018. Chromosome Segregation Fidelity in Epithelia Requires Tissue Architecture. Cell 175, 200-211.e13. https://doi.org/10.1016/j.cell.2018.07.042

Lamalice, L., Le Boeuf, F., Huot, J., 2007. Endothelial cell migration during angiogenesis. Circ Res 100, 782–794. https://doi.org/10.1161/01.RES.0000259593.07661.1e

Lancaster, O.M., Le Berre, M., Dimitracopoulos, A., Bonazzi, D., Zlotek-Zlotkiewicz, E., Picone, R., Duke, T., Piel, M., Baum, B., 2013. Mitotic rounding alters cell geometry to ensure efficient bipolar spindle formation. Dev Cell 25, 270–283. https://doi.org/10.1016/j.devcel.2013.03.014

Langer-Safer, P.R., Levine, M., Ward, D.C., 1982. Immunological method for mapping genes on Drosophila polytene chromosomes. Proc Natl Acad Sci U S A 79, 4381–4385. https://doi.org/10.1073/pnas.79.14.4381

Lawrence, M.S., Stojanov, P., Polak, P., Kryukov, G.V., Cibulskis, K., Sivachenko, A., Carter, S.L., Stewart, C., Mermel, C.H., Roberts, S.A., Kiezun, A., Hammerman, P.S., McKenna, A., Drier, Y., Zou, L., Ramos, A.H., Pugh, T.J., Stransky, N., Helman, E., Kim, J., Sougnez, C., Ambrogio, L., Nickerson, E., Shefler, E., Cortés, M.L., Auclair, D., Saksena, G., Voet, D., Noble, M., DiCara, D., Lin, P.,

Lichtenstein, L., Heiman, D.I., Fennell, T., Imielinski, M., Hernandez, B., Hodis, E., Baca, S., Dulak, A.M., Lohr, J., Landau, D.-A., Wu, C.J., Melendez-Zajgla, J., Hidalgo-Miranda, A., Koren, A., McCarroll, S.A., Mora, J., Crompton, B., Onofrio, R., Parkin, M., Winckler, W., Ardlie, K., Gabriel, S.B., Roberts, C.W.M., Biegel, J.A., Stegmaier, K., Bass, A.J., Garraway, L.A., Meyerson, M., Golub, T.R., Gordenin, D.A., Sunyaev, S., Lander, E.S., Getz, G., 2013. Mutational heterogeneity in cancer and the search for new cancer-associated genes. Nature 499, 214–218. https://doi.org/10.1038/nature12213

Lee, J.H., Berger, J.M., 2019. Cell Cycle-Dependent Control and Roles of DNA Topoisomerase II. Genes (Basel) 10, E859. https://doi.org/10.3390/genes10110859

Li, F., Aljahdali, I., Ling, X., 2019. Cancer therapeutics using survivin BIRC5 as a target: what can we do after over two decades of study? J Exp Clin Cancer Res 38, 368. https://doi.org/10.1186/s13046-019-1362-1

Li, Y.-R., Yang, W.-X., 2016. Myosins as fundamental components during tumorigenesis: diverse and indispensable. Oncotarget 7, 46785–46812. https://doi.org/10.18632/oncotarget.8800

Lichtenstein, A.V., 2018. Genetic Mosaicism and Cancer: Cause and Effect. Cancer Res 78, 1375–1378. https://doi.org/10.1158/0008-5472.CAN-17-2769

Lin, J.-R., Fallahi-Sichani, M., Sorger, P.K., 2015. Highly multiplexed imaging of single cells using a high-throughput cyclic immunofluorescence method. Nat Commun 6, 8390. https://doi.org/10.1038/ncomms9390

Liu, S., Kwon, M., Mannino, M., Yang, N., Renda, F., Khodjakov, A., Pellman, D., 2018. Nuclear envelope assembly defects link mitotic errors to chromothripsis. Nature 561, 551–555. https://doi.org/10.1038/s41586-018-0534-z

Liu, Y., Hu, X., Han, C., Wang, L., Zhang, X., He, X., Lu, X., 2015. Targeting tumor suppressor genes for cancer therapy. Bioessays 37, 1277–1286. https://doi.org/10.1002/bies.201500093

López-Carrasco, A., Martín-Vañó, S., Burgos-Panadero, R., Monferrer, E., Berbegall, A.P., Fernández-Blanco, B., Navarro, S., Noguera, R., 2020. Impact of extracellular matrix stiffness on genomic heterogeneity in MYCN-amplified neuroblastoma cell line. J Exp Clin Cancer Res 39, 226. https://doi.org/10.1186/s13046-020-01729-1

Ma, H., Naseri, A., Reyes-Gutierrez, P., Wolfe, S.A., Zhang, S., Pederson, T., 2015. Multicolor CRISPR labeling of chromosomal loci in human cells. Proc Natl Acad Sci U S A 112, 3002–3007. https://doi.org/10.1073/pnas.1420024112

Ma, X., Jana, S.S., Conti, M.A., Kawamoto, S., Claycomb, W.C., Adelstein, R.S., 2010. Ablation of nonmuscle myosin II-B and II-C reveals a role for nonmuscle myosin II in cardiac myocyte karyokinesis. Mol Biol Cell 21, 3952–3962. https://doi.org/10.1091/mbc.E10-04-0293

Mabbott, N.A., Baillie, J.K., Brown, H., Freeman, T.C., Hume, D.A., 2013. An expression atlas of human primary cells: inference of gene function from

coexpression networks. BMC Genomics 14, 632. https://doi.org/10.1186/1471-2164-14-632

Mahmood, T., Yang, P.-C., 2012. Western blot: technique, theory, and trouble shooting. N Am J Med Sci 4, 429–434. https://doi.org/10.4103/1947-2714.100998

Mandai, M., Watanabe, A., Kurimoto, Y., Hirami, Y., Morinaga, C., Daimon, T., Fujihara, M., Akimaru, H., Sakai, N., Shibata, Y., Terada, M., Nomiya, Y., Tanishima, S., Nakamura, M., Kamao, H., Sugita, S., Onishi, A., Ito, T., Fujita, K., Kawamata, S., Go, M.J., Shinohara, C., Hata, K.-I., Sawada, M., Yamamoto, M., Ohta, S., Ohara, Y., Yoshida, K., Kuwahara, J., Kitano, Y., Amano, N., Umekage, M., Kitaoka, F., Tanaka, A., Okada, C., Takasu, N., Ogawa, S., Yamanaka, S., Takahashi, M., 2017. Autologous Induced Stem-Cell-Derived Retinal Cells for Macular Degeneration. N Engl J Med 376, 1038–1046. https://doi.org/10.1056/NEJMoa1608368

Mandrell, R.E., Griffiss, J.M., Macher, B.A., 1988. Lipooligosaccharides (LOS) of Neisseria gonorrhoeae and Neisseria meningitidis have components that are immunochemically similar to precursors of human blood group antigens. Carbohydrate sequence specificity of the mouse monoclonal antibodies that recognize crossreacting antigens on LOS and human erythrocytes. J Exp Med 168, 107–126. https://doi.org/10.1084/jem.168.1.107

Mansoori, B., Mohammadi, A., Davudian, S., Shirjang, S., Baradaran, B., 2017. The Different Mechanisms of Cancer Drug Resistance: A Brief Review. Adv Pharm Bull 7, 339–348. https://doi.org/10.15171/apb.2017.041

Martincorena, I., Roshan, A., Gerstung, M., Ellis, P., Van Loo, P., McLaren, S., Wedge, D.C., Fullam, A., Alexandrov, L.B., Tubio, J.M., Stebbings, L., Menzies, A., Widaa, S., Stratton, M.R., Jones, P.H., Campbell, P.J., 2015. Tumor evolution. High burden and pervasive positive selection of somatic mutations in normal human skin. Science 348, 880–886. https://doi.org/10.1126/science.aaa6806

Matthews, H.K., Ganguli, S., Plak, K., Taubenberger, A.V., Win, Z., Williamson, M., Piel, M., Guck, J., Baum, B., 2020. Oncogenic Signaling Alters Cell Shape and Mechanics to Facilitate Cell Division under Confinement. Dev Cell 52, 563-573.e3. https://doi.org/10.1016/j.devcel.2020.01.004

Mazzolini, R., Dopeso, H., Mateo-Lozano, S., Chang, W., Rodrigues, P., Bazzocco, S., Alazzouzi, H., Landolfi, S., Hernández-Losa, J., Andretta, E., Alhopuro, P., Espín, E., Armengol, M., Tabernero, J., Ramón y Cajal, S., Kloor, M., Gebert, J., Mariadason, J.M., Schwartz, S., Aaltonen, L.A., Mooseker, M.S., Arango, D., 2012. Brush border myosin Ia has tumor suppressor activity in the intestine. Proc Natl Acad Sci U S A 109, 1530–1535. https://doi.org/10.1073/pnas.1108411109

Meng, Z., Qiu, Y., Lin, K.C., Kumar, A., Placone, J.K., Fang, C., Wang, K.-C., Lu, S., Pan, M., Hong, A.W., Moroishi, T., Luo, M., Plouffe, S.W., Diao, Y., Ye, Z., Park, H.W., Wang, X., Yu, F.-X., Chien, S., Wang, C.-Y., Ren, B., Engler, A.J., Guan, K.-

L., 2018. RAP2 mediates mechanoresponses of the Hippo pathway. Nature 560, 655–660. https://doi.org/10.1038/s41586-018-0444-0

Mo, H.Y., An, C.H., Choi, E.J., Yoo, N.J., Lee, S.H., 2020. Somatic mutation and loss of expression of a candidate tumor suppressor gene TET3 in gastric and colorectal cancers. Pathol Res Pract 216, 152759. https://doi.org/10.1016/j.prp.2019.152759

Morris, J.K., Wald, N.J., Watt, H.C., 1999. Fetal loss in Down syndrome pregnancies. Prenat Diagn 19, 142–145.

Najafi, M., Farhood, B., Mortezaee, K., 2019. Extracellular matrix (ECM) stiffness and degradation as cancer drivers. J Cell Biochem 120, 2782–2790. https://doi.org/10.1002/jcb.27681

Nathanson, D.A., Gini, B., Mottahedeh, J., Visnyei, K., Koga, T., Gomez, G., Eskin, A., Hwang, K., Wang, J., Masui, K., Paucar, A., Yang, H., Ohashi, M., Zhu, S., Wykosky, J., Reed, R., Nelson, S.F., Cloughesy, T.F., James, C.D., Rao, P.N., Kornblum, H.I., Heath, J.R., Cavenee, W.K., Furnari, F.B., Mischel, P.S., 2014. Targeted therapy resistance mediated by dynamic regulation of extrachromosomal mutant EGFR DNA. Science 343, 72–76. https://doi.org/10.1126/science.1241328

Nava, M.M., Miroshnikova, Y.A., Biggs, L.C., Whitefield, D.B., Metge, F., Boucas, J., Vihinen, H., Jokitalo, E., Li, X., García Arcos, J.M., Hoffmann, B., Merkel, R., Niessen, C.M., Dahl, K.N., Wickström, S.A., 2020. Heterochromatin-Driven Nuclear Softening Protects the Genome against Mechanical Stress-Induced Damage. Cell 181, 800-817.e22. https://doi.org/10.1016/j.cell.2020.03.052

Nelakanti, R.V., Kooreman, N.G., Wu, J.C., 2015. Teratoma formation: a tool for monitoring pluripotency in stem cell research. Curr Protoc Stem Cell Biol 32, 4A.8.1-4A.8.17. https://doi.org/10.1002/9780470151808.sc04a08s32

Nicholson, J.M., Macedo, J.C., Mattingly, A.J., Wangsa, D., Camps, J., Lima, V., Gomes, A.M., Dória, S., Ried, T., Logarinho, E., Cimini, D., 2015. Chromosome mis-segregation and cytokinesis failure in trisomic human cells. Elife 4. https://doi.org/10.7554/eLife.05068

Nielsen, C.F., Zhang, T., Barisic, M., Kalitsis, P., Hudson, D.F., 2020. Topoisomerase IIα is essential for maintenance of mitotic chromosome structure. Proc Natl Acad Sci U S A 117, 12131–12142. https://doi.org/10.1073/pnas.2001760117

Northcott, P.A., Buchhalter, I., Morrissy, A.S., Hovestadt, V., Weischenfeldt, J., Ehrenberger, T., Gröbner, S., Segura-Wang, M., Zichner, T., Rudneva, V.A., Warnatz, H.-J., Sidiropoulos, N., Phillips, A.H., Schumacher, S., Kleinheinz, K., Waszak, S.M., Erkek, S., Jones, D.T.W., Worst, B.C., Kool, M., Zapatka, M., Jäger, N., Chavez, L., Hutter, B., Bieg, M., Paramasivam, N., Heinold, M., Gu, Z., Ishaque, N., Jäger-Schmidt, C., Imbusch, C.D., Jugold, A., Hübschmann, D., Risch, T., Amstislavskiy, V., Gonzalez, F.G.R., Weber, U.D., Wolf, S., Robinson, G.W., Zhou, X., Wu, G., Finkelstein, D., Liu, Y., Cavalli, F.M.G., Luu, B., Ramaswamy, V., Wu, X., Koster, J., Ryzhova, M., Cho, Y.-J., Pomeroy, S.L., Herold-Mende, C., Schuhmann, M., Ebinger, M., Liau, L.M., Mora, J., McLendon, R.E., Jabado, N.,

Kumabe, T., Chuah, E., Ma, Y., Moore, R.A., Mungall, A.J., Mungall, K.L., Thiessen, N., Tse, K., Wong, T., Jones, S.J.M., Witt, O., Milde, T., Von Deimling, A., Capper, D., Korshunov, A., Yaspo, M.-L., Kriwacki, R., Gajjar, A., Zhang, J., Beroukhim, R., Fraenkel, E., Korbel, J.O., Brors, B., Schlesner, M., Eils, R., Marra, M.A., Pfister, S.M., Taylor, M.D., Lichter, P., 2017. The whole-genome landscape of medulloblastoma subtypes. Nature 547, 311–317. https://doi.org/10.1038/nature22973

O'Donovan, P.J., Livingston, D.M., 2010. BRCA1 and BRCA2: breast/ovarian cancer susceptibility gene products and participants in DNA double-strand break repair. Carcinogenesis 31, 961–967. https://doi.org/10.1093/carcin/bgq069

Osgood, E.E., 1955. Development and growth of hematopoietic tissues; with a clinically practical method of growth analysis. Pediatrics 15, 733–751.

Ouderkirk, J.L., Krendel, M., 2014. Non-muscle myosins in tumor progression, cancer cell invasion, and metastasis. Cytoskeleton (Hoboken) 71, 447–463. https://doi.org/10.1002/cm.21187

Parajón, E., Surcel, A., Robinson, D.N., 2021. The mechanobiome: a goldmine for cancer therapeutics. Am J Physiol Cell Physiol 320, C306–C323. https://doi.org/10.1152/ajpcell.00409.2020

Parola, M., Pinzani, M., 2019. Liver fibrosis: Pathophysiology, pathogenetic targets and clinical issues. Mol Aspects Med 65, 37–55. https://doi.org/10.1016/j.mam.2018.09.002

Paszek, M.J., DuFort, C.C., Rossier, O., Bainer, R., Mouw, J.K., Godula, K., Hudak, J.E., Lakins, J.N., Wijekoon, A.C., Cassereau, L., Rubashkin, M.G., Magbanua, M.J., Thorn, K.S., Davidson, M.W., Rugo, H.S., Park, J.W., Hammer, D.A., Giannone, G., Bertozzi, C.R., Weaver, V.M., 2014. The cancer glycocalyx mechanically primes integrin-mediated growth and survival. Nature 511, 319–325. https://doi.org/10.1038/nature13535

Patterson, D., 2009. Molecular genetic analysis of Down syndrome. Hum Genet 126, 195–214. https://doi.org/10.1007/s00439-009-0696-8

Payne, S.R., Kemp, C.J., 2005. Tumor suppressor genetics. Carcinogenesis 26, 2031–2045. https://doi.org/10.1093/carcin/bgi223

Peck, K.M., Lauring, A.S., 2018. Complexities of Viral Mutation Rates. J Virol 92, e01031-17. https://doi.org/10.1128/JVI.01031-17

Perrier, X., De Langhe, E., Donohue, M., Lentfer, C., Vrydaghs, L., Bakry, F., Carreel, F., Hippolyte, I., Horry, J.-P., Jenny, C., Lebot, V., Risterucci, A.-M., Tomekpe, K., Doutrelepont, H., Ball, T., Manwaring, J., de Maret, P., Denham, T., 2011. Multidisciplinary perspectives on banana (Musa spp.) domestication. Proc Natl Acad Sci U S A 108, 11311–11318. https://doi.org/10.1073/pnas.1102001108

Petridou, N.I., Corominas-Murtra, B., Heisenberg, C.-P., Hannezo, E., 2021. Rigidity percolation uncovers a structural basis for embryonic tissue phase transitions. Cell 184, 1914-1928.e19. https://doi.org/10.1016/j.cell.2021.02.017

Pfeifer, C.R., Alvey, C.M., Irianto, J., Discher, D.E., 2017. Genome variation across cancers scales with tissue stiffness - an invasion-mutation mechanism and implications for immune cell infiltration. Curr Opin Syst Biol 2, 103–114. https://doi.org/10.1016/j.coisb.2017.04.005

Pfeifer, G.P., Denissenko, M.F., Olivier, M., Tretyakova, N., Hecht, S.S., Hainaut, P., 2002. Tobacco smoke carcinogens, DNA damage and p53 mutations in smoking-associated cancers. Oncogene 21, 7435–7451. https://doi.org/10.1038/sj.onc.1205803

Picariello, H.S., Kenchappa, R.S., Rai, V., Crish, J.F., Dovas, A., Pogoda, K., McMahon, M., Bell, E.S., Chandrasekharan, U., Luu, A., West, R., Lammerding, J., Canoll, P., Odde, D.J., Janmey, P.A., Egelhoff, T., Rosenfeld, S.S., 2019. Myosin IIA suppresses glioblastoma development in a mechanically sensitive manner. Proc Natl Acad Sci U S A 116, 15550–15559. https://doi.org/10.1073/pnas.1902847116

Pollard, T.D., Ostap, E.M., 1996. The chemical mechanism of myosin-I: implications for actin-based motility and the evolution of the myosin family of motor proteins. Cell Struct Funct 21, 351–356. https://doi.org/10.1247/csf.21.351

Przybyla, L., Muncie, J.M., Weaver, V.M., 2016. Mechanical Control of Epithelial-to-Mesenchymal Transitions in Development and Cancer. Annu Rev Cell Dev Biol 32, 527–554. https://doi.org/10.1146/annurev-cellbio-111315-125150

Raab, M., Swift, J., Dingal, P.C.D.P., Shah, P., Shin, J.-W., Discher, D.E., 2012. Crawling from soft to stiff matrix polarizes the cytoskeleton and phosphoregulates myosin-II heavy chain. J Cell Biol 199, 669–683. https://doi.org/10.1083/jcb.201205056

Rajagopalan, H., Lengauer, C., 2004. Aneuploidy and cancer. Nature 432, 338–341. https://doi.org/10.1038/nature03099

Ramanathan, S.P., Helenius, J., Stewart, M.P., Cattin, C.J., Hyman, A.A., Muller, D.J., 2015. Cdk1-dependent mitotic enrichment of cortical myosin II promotes cell rounding against confinement. Nat Cell Biol 17, 148–159. https://doi.org/10.1038/ncb3098

Ramos-Mejia, V., Melen, G.J., Sanchez, L., Gutierrez-Aranda, I., Ligero, G., Cortes, J.L., Real, P.J., Bueno, C., Menendez, P., 2010. Nodal/Activin signaling predicts human pluripotent stem cell lines prone to differentiate toward the hematopoietic lineage. Mol Ther 18, 2173–2181. https://doi.org/10.1038/mt.2010.179

Rancati, G., Pavelka, N., Fleharty, B., Noll, A., Trimble, R., Walton, K., Perera, A., Staehling-Hampton, K., Seidel, C.W., Li, R., 2008. Aneuploidy underlies rapid adaptive evolution of yeast cells deprived of a conserved cytokinesis motor. Cell 135, 879–893. https://doi.org/10.1016/j.cell.2008.09.039

Ratna, A., Mandrekar, P., 2017. Alcohol and Cancer: Mechanisms and Therapies. Biomolecules 7, E61. https://doi.org/10.3390/biom7030061

Ring, K.L., Garcia, C., Thomas, M.H., Modesitt, S.C., 2017. Current and future role of genetic screening in gynecologic malignancies. Am J Obstet Gynecol 217, 512–521. https://doi.org/10.1016/j.ajog.2017.04.011

Saez, A., Buguin, A., Silberzan, P., Ladoux, B., 2005. Is the mechanical activity of epithelial cells controlled by deformations or forces? Biophys J 89, L52-54. https://doi.org/10.1529/biophysj.105.071217

Samejima, K., Samejima, I., Vagnarelli, P., Ogawa, H., Vargiu, G., Kelly, D.A., de Lima Alves, F., Kerr, A., Green, L.C., Hudson, D.F., Ohta, S., Cooke, C.A., Farr, C.J., Rappsilber, J., Earnshaw, W.C., 2012. Mitotic chromosomes are compacted laterally by KIF4 and condensin and axially by topoisomerase IIα. J Cell Biol 199, 755–770. https://doi.org/10.1083/jcb.201202155

Santaguida, S., Richardson, A., Iyer, D.R., M'Saad, O., Zasadil, L., Knouse, K.A., Wong, Y.L., Rhind, N., Desai, A., Amon, A., 2017. Chromosome Mis-segregation Generates Cell-Cycle-Arrested Cells with Complex Karyotypes that Are Eliminated by the Immune System. Dev Cell 41, 638-651.e5. https://doi.org/10.1016/j.devcel.2017.05.022

Schmitt, M.W., Prindle, M.J., Loeb, L.A., 2012. Implications of genetic heterogeneity in cancer. Ann N Y Acad Sci 1267, 110–116. https://doi.org/10.1111/j.1749-6632.2012.06590.x

Schramek, D., Sendoel, A., Segal, J.P., Beronja, S., Heller, E., Oristian, D., Reva, B., Fuchs, E., 2014. Direct in vivo RNAi screen unveils myosin IIa as a tumor suppressor of squamous cell carcinomas. Science 343, 309–313. https://doi.org/10.1126/science.1248627

Schwabe, R.F., Tabas, I., Pajvani, U.B., 2020. Mechanisms of Fibrosis Development in Nonalcoholic Steatohepatitis. Gastroenterology 158, 1913–1928. https://doi.org/10.1053/j.gastro.2019.11.311

Sedzinski, J., Biro, M., Oswald, A., Tinevez, J.-Y., Salbreux, G., Paluch, E., 2011. Polar actomyosin contractility destabilizes the position of the cytokinetic furrow. Nature 476, 462–466. https://doi.org/10.1038/nature10286

Segel, M., Neumann, B., Hill, M.F.E., Weber, I.P., Viscomi, C., Zhao, C., Young, A., Agley, C.C., Thompson, A.J., Gonzalez, G.A., Sharma, A., Holmqvist, S., Rowitch, D.H., Franze, K., Franklin, R.J.M., Chalut, K.J., 2019. Niche stiffness underlies the ageing of central nervous system progenitor cells. Nature 573, 130–134. https://doi.org/10.1038/s41586-019-1484-9

Seitz, H.K., Stickel, F., 2007. Molecular mechanisms of alcohol-mediated carcinogenesis. Nat Rev Cancer 7, 599–612. https://doi.org/10.1038/nrc2191

Shaffer, S.M., Dunagin, M.C., Torborg, S.R., Torre, E.A., Emert, B., Krepler, C., Beqiri, M., Sproesser, K., Brafford, P.A., Xiao, M., Eggan, E., Anastopoulos, I.N., Vargas-Garcia, C.A., Singh, A., Nathanson, K.L., Herlyn, M., Raj, A., 2017. Rare cell variability and drug-induced reprogramming as a mode of cancer drug resistance. Nature 546, 431–435. https://doi.org/10.1038/nature22794

Shlien, A., Malkin, D., 2009. Copy number variations and cancer. Genome Med 1, 62. https://doi.org/10.1186/gm62

Skamagki, M., Correia, C., Yeung, P., Baslan, T., Beck, S., Zhang, C., Ross, C.A., Dang, L., Liu, Z., Giunta, S., Chang, T.-P., Wang, J., Ananthanarayanan, A., Bohndorf, M., Bosbach, B., Adjaye, J., Funabiki, H., Kim, J., Lowe, S., Collins, J.J., Lu, C.-W., Li, H., Zhao, R., Kim, K., 2017. ZSCAN10 expression corrects the genomic instability of iPSCs from aged donors. Nat Cell Biol 19, 1037–1048. https://doi.org/10.1038/ncb3598

Song, G., Xu, S., Zhang, H., Wang, Y., Xiao, C., Jiang, T., Wu, L., Zhang, T., Sun, X., Zhong, L., Zhou, C., Wang, Z., Peng, Z., Chen, J., Wang, X., 2016. TIMP1 is a prognostic marker for the progression and metastasis of colon cancer through FAK-PI3K/AKT and MAPK pathway. J Exp Clin Cancer Res 35, 148. https://doi.org/10.1186/s13046-016-0427-7

Stewart, M.P., Helenius, J., Toyoda, Y., Ramanathan, S.P., Muller, D.J., Hyman, A.A., 2011. Hydrostatic pressure and the actomyosin cortex drive mitotic cell rounding. Nature 469, 226–230. https://doi.org/10.1038/nature09642

Straight, A.F., Cheung, A., Limouze, J., Chen, I., Westwood, N.J., Sellers, J.R., Mitchison, T.J., 2003. Dissecting temporal and spatial control of cytokinesis with a myosin II Inhibitor. Science 299, 1743–1747. https://doi.org/10.1126/science.1081412

Sudo, H., 2018. Microtubule Hyperacetylation Enhances KL1-Dependent Micronucleation under a Tau Deficiency in Mammary Epithelial Cells. Int J Mol Sci 19. https://doi.org/10.3390/ijms19092488

Sun, A., Noriki, S., Imamura, Y., Fukuda, M., 2003. Detection of cancer clones in human gastric adenoma by increased DNA-instability and other biomarkers. Eur J Histochem 47, 111–122. https://doi.org/10.4081/815

Swift, J., Ivanovska, I.L., Buxboim, A., Harada, T., Dingal, P.C.D.P., Pinter, J., Pajerowski, J.D., Spinler, K.R., Shin, J.-W., Tewari, M., Rehfeldt, F., Speicher, D.W., Discher, D.E., 2013. Nuclear lamin-A scales with tissue stiffness and enhances matrix-directed differentiation. Science 341, 1240104. https://doi.org/10.1126/science.1240104

Tomasetti, C., Li, L., Vogelstein, B., 2017. Stem cell divisions, somatic mutations, cancer etiology, and cancer prevention. Science 355, 1330–1334. https://doi.org/10.1126/science.aaf9011

Tomasetti, C., Vogelstein, B., 2015. Cancer etiology. Variation in cancer risk among tissues can be explained by the number of stem cell divisions. Science 347, 78–81. https://doi.org/10.1126/science.1260825

Uhler, C., Shivashankar, G.V., 2017. Regulation of genome organization and gene expression by nuclear mechanotransduction. Nat Rev Mol Cell Biol 18, 717–727. https://doi.org/10.1038/nrm.2017.101

Umbreit, N.T., Zhang, C.-Z., Lynch, L.D., Blaine, L.J., Cheng, A.M., Tourdot, R., Sun, L., Almubarak, H.F., Judge, K., Mitchell, T.J., Spektor, A., Pellman, D., 2020. Mechanisms generating cancer genome complexity from a single cell division error. Science 368. https://doi.org/10.1126/science.aba0712

Vignesh Kumar, B., Backiyarani, S., Chandrasekar, A., Saranya, S., Ramajayam, D., Saraswathi, M.S., Durai, P., Kalpana, S., Uma, S., 2020. Strengthening of banana breeding through data digitalization. Database (Oxford) 2020, baz145. https://doi.org/10.1093/database/baz145

von Morgen, P., Lidak, T., Horejsi, Z., Macurek, L., 2018. Nuclear localisation of 53BP1 is regulated by phosphorylation of the nuclear localisation signal. Biol Cell 110, 137–146. https://doi.org/10.1111/boc.201700067

Wang, C.X., Jimenez-Sainz, J., Jensen, R.B., Mazin, A.V., 2019. The Post-Synaptic Function of Brca2. Sci Rep 9, 4554. https://doi.org/10.1038/s41598-019-41054-y

Wang, H., Nakamura, M., Abbott, T.R., Zhao, D., Luo, K., Yu, C., Nguyen, C.M., Lo, A., Daley, T.P., La Russa, M., Liu, Y., Qi, L.S., 2019. CRISPR-mediated live imaging of genome editing and transcription. Science 365, 1301–1305. https://doi.org/10.1126/science.aax7852

Wang, H., Zhao, Q., Deng, K., Guo, X., Xia, J., 2016. Lin28: an emerging important oncogene connecting several aspects of cancer. Tumour Biol 37, 2841–2848. https://doi.org/10.1007/s13277-015-4759-2

Wang, L., Zhang, M.-X., Zhang, M.-F., Tu, Z.-W., 2020. ZBTB7A functioned as an oncogene in colorectal cancer. BMC Gastroenterol 20, 370. https://doi.org/10.1186/s12876-020-01456-z

Wang, Q., Zhang, H., Guerrette, S., Chen, J., Mazurek, A., Wilson, T., Slupianek, A., Skorski, T., Fishel, R., Greene, M.I., 2001. Adenosine nucleotide modulates the physical interaction between hMSH2 and BRCA1. Oncogene 20, 4640–4649. https://doi.org/10.1038/sj.onc.1204625

Wang, Y., Liu, S., Zhang, Y., Yang, J., 2019. Myosin Heavy Chain 9: Oncogene or Tumor Suppressor Gene? Med Sci Monit 25, 888–892. https://doi.org/10.12659/MSM.912320

Wang, Y., Putnam, C.D., Kane, M.F., Zhang, W., Edelmann, L., Russell, R., Carrión, D.V., Chin, L., Kucherlapati, R., Kolodner, R.D., Edelmann, W., 2005. Mutation in Rpa1 results in defective DNA double-strand break repair, chromosomal instability and cancer in mice. Nat Genet 37, 750–755. https://doi.org/10.1038/ng1587

Warmoes, M., Jaspers, J.E., Pham, T.V., Piersma, S.R., Oudgenoeg, G., Massink, M.P.G., Waisfisz, Q., Rottenberg, S., Boven, E., Jonkers, J., Jimenez, C.R., 2012. Proteomics of mouse BRCA1-deficient mammary tumors identifies DNA repair proteins with potential diagnostic and prognostic value in human breast cancer. Mol Cell Proteomics 11, M111.013334. https://doi.org/10.1074/mcp.M111.013334

Weinberg, R.A., 2014. The biology of cancer, Second edition. ed. Garland Science, Taylor & Francis Group, New York.

Woo, X.Y., Giordano, J., Srivastava, A., Zhao, Z.-M., Lloyd, M.W., de Bruijn, R., Suh, Y.-S., Patidar, R., Chen, L., Scherer, S., Bailey, M.H., Yang, C.-H., Cortes-Sanchez, E., Xi, Y., Wang, J., Wickramasinghe, J., Kossenkov, A.V., Rebecca, V.W., Sun, H., Mashl, R.J., Davies, S.R., Jeon, R., Frech, C., Randjelovic, J., Rosains, J., Galimi, F., Bertotti, A., Lafferty, A., O'Farrell, A.C., Modave, E., Lambrechts, D., Ter Brugge, P., Serra, V., Marangoni, E., El Botty, R., Kim, H., Kim, J.-I., Yang, H.-K., Lee, C., Dean, D.A., Davis-Dusenbery, B., Evrard, Y.A., Doroshow, J.H., Welm, A.L., Welm, B.E., Lewis, M.T., Fang, B., Roth, J.A., Meric-Bernstam, F., Herlyn, M., Davies, M.A., Ding, L., Li, S., Govindan, R., Isella, C., Moscow, J.A., Trusolino, L., Byrne, A.T., Jonkers, J., Bult, C.J., Medico, E., Chuang, J.H., PDXNET Consortium, EurOPDX Consortium, 2021. Conservation of copy number profiles during engraftment and passaging of patient-derived cancer xenografts. Nat Genet 53, 86–99. https://doi.org/10.1038/s41588-020-00750-6

Xia, Y., Ivanovska, I.L., Zhu, K., Smith, L., Irianto, J., Pfeifer, C.R., Alvey, C.M., Ji, J., Liu, D., Cho, S., Bennett, R.R., Liu, A.J., Greenberg, R.A., Discher, D.E., 2018. Nuclear rupture at sites of high curvature compromises retention of DNA repair factors. J Cell Biol 217, 3796–3808. https://doi.org/10.1083/jcb.201711161

Yang, C., Tibbitt, M.W., Basta, L., Anseth, K.S., 2014. Mechanical memory and dosing influence stem cell fate. Nat Mater 13, 645–652. https://doi.org/10.1038/nmat3889

Yao, Y., Dai, W., 2014. Genomic Instability and Cancer. J Carcinog Mutagen 5, 1000165. https://doi.org/10.4172/2157-2518.1000165

Yizhak, K., Aguet, F., Kim, J., Hess, J.M., Kübler, K., Grimsby, J., Frazer, R., Zhang, H., Haradhvala, N.J., Rosebrock, D., Livitz, D., Li, X., Arich-Landkof, E., Shoresh, N., Stewart, C., Segrè, A.V., Branton, P.A., Polak, P., Ardlie, K.G., Getz, G., 2019. RNA sequence analysis reveals macroscopic somatic clonal expansion across normal tissues. Science 364. https://doi.org/10.1126/science.aaw0726

Yoshida, K., Miki, Y., 2004. Role of BRCA1 and BRCA2 as regulators of DNA repair, transcription, and cell cycle in response to DNA damage. Cancer Sci 95, 866–871. https://doi.org/10.1111/j.1349-7006.2004.tb02195.x

Zhang, C.-Z., Spektor, A., Cornils, H., Francis, J.M., Jackson, E.K., Liu, S., Meyerson, M., Pellman, D., 2015. Chromothripsis from DNA damage in micronuclei. Nature 522, 179–184. https://doi.org/10.1038/nature14493

Zhang, N., Bao, Y., Xie, Z., Huang, X., Sun, Y., Feng, G., Zeng, H., Ren, J., Li, Y., Xiong, J., Chen, W., Yan, C., Tang, M., 2019. Efficient Characterization of Tetraploid Watermelon. Plants (Basel) 8, E419. https://doi.org/10.3390/plants8100419

Zheng, X., Amos, C.I., Frost, H.R., 2020. Cancer prognosis prediction using somatic point mutation and copy number variation data: a comparison of gene-level and pathway-based models. BMC Bioinformatics 21, 467. https://doi.org/10.1186/s12859-020-03791-0

Znojek, P., Willmore, E., Curtin, N.J., 2014. Preferential potentiation of topoisomerase I poison cytotoxicity by PARP inhibition in S phase. Br J Cancer 111, 1319–1326. https://doi.org/10.1038/bjc.2014.378